X-ray Observation of X-ray Binary Pulsar Centaurus X-3 with RXTE

Takayoshi Kohmura

Department of Earth & Space Science, Graduated School of Science,

Osaka University,

1-1 Machikaneyama-cho, Toyonaka, Osaka, 560-0043, Japan

A Dissertation

Submitted in Partial Fulfillment of the Requirements

for the Degree of Doctor of Philosophy

Osaka University

Abstract

We present the study of the aperiodic time variation of the binary X-ray pulsar Centaurus X-3 (Cen X-3) observed with the *Rossi X-Ray Timing Explorer* (RXTE).

We analyzed four data of Cen X-3 observed with *RXTE*. We extracted light curves both in the energy band which included the iron K lines ("iron-band") and in the continuum X-ray bands which did not include the iron K lines. Then, we calculated cross spectrum functions between the iron-band and the remaining continuum bands. We discovered, for the first time, the significant time delay of temporal variation of iron-band emission as compared with that of the other energy X-rays by (0.39±0.10) ms, (0.32±0.30) ms and (0.66±0.26) ms (1-σ error). We also discovered the time difference showed a general trend such that the higher energy X-rays advanced in comparison with the lower energy X-rays with the exception of the iron-band.

Assuming that the iron emission lines are fluorescent lines in origin and are emitted by circumstellar matter, we derive (6.0±2.4) ms, (4.0±3.8) ms and (10.1±4.9) ms for the time delay of the temporal variation of the iron lines from the average temporal variation in the energy band above the iron absorption edge, taking into account the energy spectral shape and the photo-electric absorption cross section. These results lead to a determination of $(1.8\pm0.7)\times10^8$ cm, $(1.2\pm1.1)\times10^8$ cm, and $(3.0\pm1.7)\times 10^8$ cm for the distance between the original X-ray source, neutron star, and the reprocessor, which emits the iron lines. These values are smaller than the size of the Alfv́en radius which is derived from Kepler frequency at the magnetospheric radius applying the Beat Frequency Model. These discrepancies of the size can be reconciled by considering that the reprocessor is distributed from the neutron star to the magnetosphere along the magnetic field. In addition, our discovery of the general trend of the hard X-ray advance is considered to be related to the X-ray emission mechanism on the neutron star.

Contents

List of Figures

List of Tables

Chapter 1

Introduction

The accretion powered pulsar, Centaurus X-3, is one of the brightest accretion powered pulsars (Giacconi et al. 1971; Schreier et al. 1972), and the mass accretion in Cen X-3 is thought to proceed not via a capture of the stellar wind (so-called "wind-fed" accretion), but via an accretion disk (so-called "disk-fed" accretion) based on many observational results: the optical observation (Tjemkes, van Paradijs, & Zuiderwijk. 1986), the systematic spin-up trend of the X-ray pulsar (e,g., White et al. 1983; Nagase et al. 1989), and the discovery of QPO in the X-ray light curve (Tennant 1988; Takeshima et al. 1991). All these results strongly suggest the presence of the accretion disk in Cen X-3.

By studying the X-ray spectrum of Cen X-3, many authors have reported complex line structure, including 6.4 keV, 6.7 keV, and 6.9 keV line emissions. The dominant component is 6.4 keV lines (iron K-lines) with relatively large equivalent width of 100–200 eV, except for during eclipses (Nagase et al. 1992; Day et al. 1993b; Ebisawa et al. 1996; Audley et al. 1998). The emission region of the iron line of 6.4 keV has been studied by many authors (White et al. 1983; Nagase et al. 1989; Ebisawa et al. 1996). The Alfv́en shell or the accretion disk, have been thought to be the plausible candidate of the reprocessed region of the iron K-lines of 6.4 keV.

If the iron K-lines originate from the magnetosphere (i.e., Alfv́en shell) and if the Alfv́en shell covers a large fraction of the solid angle from a neutron star, the line photons must be delayed in comparison with the direct X-rays from the neutron star. As we will review in chapter 2, the size of Alfv́en radius, r_A, is $\sim 10^8$ cm. Thus, the expected time delay is estimated to be an order of 10 ms.

Short term, aperiodic or quasi-periodic variations in X-ray pulsars, including Cen X-3, ranging up to kHz region (other than coherent pulsations), have been reported by several authors (e.g., Takeshima et al. 1991; Jernigan et al. 2000). We expect to be able to estimate

the radius of the magnetosphere by studying the time delay of these short-term aperiodic variations.

We have analyzed archival *Rossi X-Ray Timing Explorer* (RXTE) data of Cen X-3, which provided high time resolution data with excellent statistics and a reasonable energy resolution. Our primary goal is the determination of the time difference of the aperiodic variations using a cross spectral analysis. We derive time delays in the arrival of X-rays in different energy bands as compared with that in an energy band containing the iron K lines to determine the distance between the neutron star and the reprocessor of iron K lines.

This thesis consists of the following chapters and an appendix. In chapter 2, we will briefly review well known characteristics of pulsar, and introduce previous trials to approach their nature, especially focusing on Cen X-3. After introducing the instruments of *RXTE* in chapter 3, and the determination of the orbital parameters of Cen X-3 with *RXTE* in chapter 4, we will describe the results of the cross spectral analysis of four observations of Cen X-3 as well as the spectral and timing analyses to search for the QPO features of Cen X-3 in chapter 5. In chapter 6, we will discuss the results of the cross spectral analysis of Cen X-3. Final part of this thesis, in appendix A, we will briefly introduce the cross spectrum function.

Chapter 2

Review

2.1 Pulsars

Accretion powered pulsars among the first sources observed in X-ray astronomy, owing to their characteristic timing signatures, were quite soon correctly interpreted as rotating magnetized neutron stars (Pringle & Rees 1972; Davidson & Ostriker 1973). Since the discovery of the first binary X-ray pulsar Centaurus X-3 (Giacconi et al. 1971), the observation and the study of X-ray pulsars have provided a plenty of important information on the physics of neutron stars and on the evolution of stars in binary systems.

The designation of "*X-ray*" *pulsars* has traditionally been used to indicate the objects powered by accretion of matter from a companion star in close, interacting binary systems (e.g., Centaurus X-3 (hereafter Cen X-3), and Hercules X-1 (hereafter Her X-1)), in contract to the "*radio*" *pulsars*. The "*radio*" *pulsars* are generally isolated neutron stars, the energy source of which is a loss of their rotating energy. So far, only $\sim$ 10 of the youngest and more powerful radio pulsars have been observed with X-rays (e.g., Crab pulsar, Vela pulsar, and etc). The current X-ray satellites with the better sensitivity and the better spatial resolution has allowed the detection of X-rays pulsations from $\sim$80 sources (Liu et al. 2000, 2001).

In this chapter, we will first introduce the rotating powered pulsars for the shake of comparison to the accretion powered pulsars, second we will review the accretion powered pulsars with its observational characteristics. Finally we will review the previous observational results of Cen X-3 to make our motivation of this work clear as well as to know what is known and what is still unknown.

2.2 Rotation Powered Pulsars

There are over 1000 known pulsars so far, and they are divided into two groups. One is so called "rotation powered pulsars", and the other is "accretion powered pulsars", based on their electromagnetic radiation process. The former is powered by rotational energy of the neutron star, while the latter by gravitational energy release of accreting matter onto the neutron star.

Rotation powered pulsars are powered by the loss of the rotation energy into electromagnetic radiation through Magnetic Dipole Radiation, and also referred to as "radio pulsars" because it is mainly observed in radio band and only ~10 sources have been observed in X-ray band. These pulsars are thought to be formed in the Type II supernovae explosions (e.g., Janka & Müller 1995; Burrows et al. 1995; Janka & Müller 1996). They are usually distributed within the Galactic bulge and along the Galactic plane, and most are isolated rather than in a binary system and usually associate with a supernova remnant.

The combination of a rapid rotation and a strong magnetic field of the neutron star induces a strong electric field near the surface of the neutron star. This accelerates charged particles, primarily from the magnetic poles to away from the neutron star along the magnetic field lines. As the neutron star rotates, magnetic field accelerates these charged particles, creating non-thermal beamed radiation.

Since rotation powered pulsars convert their rotational energy into electromagnetic radiation, they exhibit spin-down. Here, the luminosity of the magnetic dipole radiation L_{mdr} scales as $L_{mdr} = (8\pi^4/3c^3)\ R_{N.S}^6 B^2 P^{-4}$ erg s^{-1}, where $R_{N.S}$ is the radius of the neutron star, B is the surface magnetic field, and P is the pulse period, as the pulsar ages the spin-down causes the rotation period to increase, and therefore the luminosity to decrease. The observed spin-down rate can be converted into a rotational energy loss rate $L_{rot} = -\ (2\pi)^2\ I\dot{P}P^{-3}$, where $I \sim 10^{45}$ gcm^3 is the neutron star moment of inertia. Then the equation of L_{mdr} with L_{rot} enable to calculate the magnetic field B of the neutron star, as

$$B = (\frac{3Ic^3\dot{P}P}{2\pi^2 R_{N.S}^6})^{1/2} \approx 3.2 \times 10^{19}\sqrt{\dot{P}P}\ \text{G}. \tag{2.1}$$

Using above equation, the magnetic field of rotation powered pulsars is estimated to be 10^{11}–10^{13} G.

2.3 Accretion Powered Pulsars

In general, all accretion powered pulsars belong to binary systems (X-Ray Binaries (XRBs)), without some unknown objects such as Anomalous X-ray Pulsars (AXPs) (e.g., van Paradijs J. et al. 1995; White et al. 1996; Ghosh et al. 1997; Mereghetti et al. 1997), although some accretion powered pulsars remain to have an unidentified companion star. XRBs contain a compact object (either a neutron star, a white dwarf, or a black hole) along with a normal companion star, and they rotate around their center of gravity. XRBs are divided into two groups based on the mass of their companion star; High Mass X-ray Binaries (HMXBs) and Low Mass X-ray Binaries (LMXBs). These sources exhibit many interesting phenomena, such as quasi-periodic oscillations, X-ray outbursts, flares, and so on.

In many XRBs, the transferred material from the companion star to the compact star cannot land onto the companion star until it has rid itself of most of its angular momentum. This may lead to the formation of an accretion disk, which is an efficient machine for extracting gravitational potential energy and converting it into radiation. This mass transfer proceeds either via a Roche-lobe overflow or via a strong stellar wind (Figure 2.1). We refer the mass accretion system via the accretion disk as a disk-fed accretion and via the stellar wind as a wind-fed accretion.

The Roche-lobe overflow occurs when the companion star extends beyond the inner Lagrange point of the system or the binary separation shrinks, and so material falls from the companion star to the compact object. As the material spirals inward angular momentum is conserved, preventing the material from being directly accreted. Instead, the material goes into quasi-Keplerian orbits around the compact object and an accretion disk is formed. In the accretion disk, viscous forces transfer angular momentum outward in the accretion disk as material moves inward and eventually onto the compact object (Shakura & Sunyaev 1973). This is common case if the companion star is a low mass star, where the envelope of the companion expandes as it evolves away from the main sequence.

The wind-fed accretion occurrs when the companion star is a high mass star, such as an OB or an OBe star. In this case, the mass loss rate of the high mass star is much high, 10^{-10} – 10^{-6} $M_{\odot}yr^{-1}$, and the terminal velocity goes up to ~1,000 km s^{-1}. A compact object in this binary system can capture a significant fraction of the wind (Figure 2.1).

In the common case, X-ray binary pulsars have an elliptical orbit. When the Roche-lobe filling condition or the stellar wind density changes with the orbital phase, the X-ray intensity from these system can be modulated with the orbital phase. Thus, persistent pulsating objects are quite rare, and the majority of the X-ray pulsars are the transient X-ray sources. Therefore, it is difficult to estimate the real number of the accretion powered

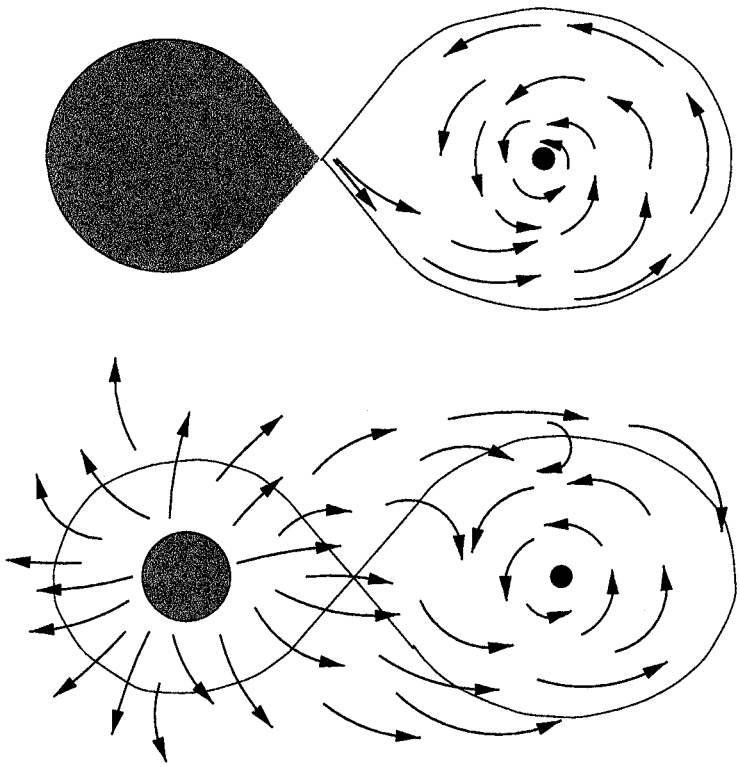

Figure 2.1: Two scenarios for mass accretion from the companion star to the compact object. (i) Upper figure shows the Roche lobe overflow. The companion star in a XRB system may increase in radius, or the binary separation shrinks. Finaly the radius exceedes the point where the gravitational pull of the companion can remove the outer layers of its envelope, and the outflow proceeds mainly through the first Lagrange point. (ii)Bottom figure shows the stellar wind accretion. The companion star ejects much of its mass in the form of a stellar wind; some of this material will be captured gravitationally by the companion.

pulsars. But in these days, owing to the development of both X-ray detectors, such as Charge Coupled Devices (CCDs), and X-ray telescopes with high sensitivity and the good spatial resolution, many new pulsars have been discovered.

Table 2.1 shows the presently known accretion powered pulsars, which are generally classified according to the mass of the companion star as either low mass ($M_c \leq 2.5 M_\odot$) or high-mass ($M_c \geq 6 M_\odot$) systems. There are only five known LMXBs as accretion powered pulsars: Her X-1, 4U 1626-67, GX 1+4, GRO J1744-28, and SAX J 1808.4-3656. The majority of LMXBs are not pulsars and thus evidently have too weak magnetic field to strongly affect the accretion flow ($B \leq 10^9$G).

2.3.1 High Mass X-ray Binary Pulsars

So far, $\sim$ 130 X-ray sources are identified as HMXBs (Liu et al. 2000), and more than half of them, $\sim$70, are high mass X-ray binary pulsars. The high mass X-ray binaries may be divided into those with main-sequence Oe/Be star companions and those with evolved OB supergiant companions. In general, the Oe/Be systems, which account for more than half of the known accretion powered pulsars, are observed during transient outbursts. The companion star in these systems is still on the main sequence and lying well inside its Roche surface. The episodic outbursts are often correlated with periastron passage of the neutron star. The systems are thought to undergo a "propeller" phase during X-ray quiescence (Stella, White, & Rosner 1986).

The supergiant binaries may be further divided into two groups based on the dominant mode of mass transfer: the Roche lobe overflow or the capture of the stellar wind. In some systems, both types of mass transfer may be taking place (Blondin, Stevens, & Kallman 1991). Most of OB supergiants have stellar winds driven by the radiation pressure via the resonance lines of highly ionized atoms, with mass loss rates of $\dot{M} \sim 10^{-6}\ M_\odot\ \mathrm{yr}^{-1}$. Although the capture of a high velocity stellar wind is inefficient, the large mass loss rate in the stellar wind can result in an appreciable mass accretion rate onto the neutron star. Vela X-1 is the best known example of a wind-fed supergiant pulsar.

When the companion star fills its Roche lobe, the accreting matter from companion star flows with high specific angular momentum through the first Lagrange points and forms an accretion disk around the neutron star. This is a very efficient form of high accretion rates in SMC X-1, Cen X-3, and LMC X-4 make them prime candidate for the disk-fed (via Roche Robe over flow) supergiant pulsar binaries. Optical photometric observations of these systems show both an ellipsoidal variation by a tidally distorted companion and an excess light owing to the presence of an accretion disk (van Paradijs & McClintock 1995 and

Table 2.1: Known Accretion powered pulsars from (Bildsten et al. (1997); Lui et al. (2001)

System	l_{II}	b_{II}	P_{spin}(s)	P_{orb}	Companion (MK Type)
Low-Mass Binaries					
GRO J1744–28	0.0	+0.3	0.467	11.8	
Her X-1	58.2	+37.5	1.24	1.70	Hz Her (A9-b)
4U 1626–67	321.8	-13.1	7.66	0.0289	KZ Tra (low-mass dwarf)
4U 1728–247 (GX 1+4) ...	1.9	+4.8	120		V2116 Oph (M6 III)
SAX J 1808.4-3656 ...	355.4	-8.14	0.00249	2.014167	
High-Mass Supergiant and Giant Systems					
SMC X-1	300.4	-43.6	0.717	3.89	Sk 160 (B0 I)
Cen X-3	292.1	+0.3	4.82	2.09	V779 Cen (O6–8f)
RX J0648.1–4419	253.7	-19.1	13.2	1.54	HD 49798 (O6p)
LMC X-4	276.3	-32.5	13.5	1.41	Sk-Ph (O7 III–V)
OAO 1657–415	344.4	+0.3	37.7	10.4	(B0–6 Iab)
Vela X-1	263.1	+3.9	283	8.96	HD 77581 (B0.5 Ib)
1E 1145.1–6141	295.5	-0.0	297		V830 Cen (B2 Iae)
4U 1907+09	43.7	+0.5	438	8.38	(B I)
4U 1538–52	327.4	+2.1	530	3.73	QV Nor (B0 Iab)
GX 301–2	300.1	-0.0	681	41.5	Wray 977 (B1.5 Ia)
Transient Be-Binary Systems					
A0538–67	276.9	-32.2	0.069	16.7	(B2 III–IVe)
4U 0115+63	125.9	+1.0	3.61	24.3	V635 Cas (Be)
V0332+53	146.1	-2.2	4.37	34.2	BQ Cam (Be)
2S 1417–624	313.0	-1.6	17.6	42.1	(OBe)
EXO 2030+375	77.2	-1.3	41.7	46.0	(Be)
GRO J1008–57	283.0	-1.8	93.5	$\approx$ 248	(Be)
A0535+26	181.4	-2.6	105	110	HDE 245770 (O9.7 IIe)
GX 304–1	302.1	+1.2	272	133.(?)	V850 Cen (B2 Vne)
4U 1145–619	295.6	-0.2	292	187	Hen 715 (B1 Vne)
A1118–616	292.5	-0.9	405		He 3-640 (O9.5 III-Ve)
4U 0352+309	163.1	-17.1	835		X Per (O9 III-Ve)
RX J0146.9+6121	129.9	-0.5	1413		LS I+61° 235 (B5 IIIe)
Persistent Systems with an Undetermined Companion					
RX J1838.4–0301	28.8	+1.5	5.45		
1E 1048–593	288.2	-0.5	6.44		
1E 2259+586	109.1	-1.0	6.98		
RX J0720.4–3125	244.2	-8.2	8.38		
4U 0142+614	129.4	-0.4	8.69		
Transient Systems with an Undetermined Companion					
RX J0059.2–7138[c]	302.1	-45.5	2.76		
RX J0502.9–6626	277.0	-35.5	4.06		
GRO J1750–27	2.4	+0.5	4.45	29.8	
2E 0050.1–7247	302.9	-44.6	8.9		
2S 1553–54	327.9	-0.9	9.26	30.6	
GS 0834–430	262.0	-1.5	12.3	106	
GRO J1948+32	64.9	1.8	18.7		
GS 1843+00	33.1	+1.7	29.5		
GS 2138+56(Cep X-4?) ...	99.0	+3.3	66.2		
GS 1843–024	30.2	-0.0	94.8		
Sct X-1	24.5	-0.2	111		
GRO J2058+42	83.6	-2.7	198	$\approx$ 110	
GPS 1722–363	351.5	-0.6	414		

references therein).

2.3.2 Low Mass X-ray Binary Pulsars

Low mass X-ray binaries (LMXBs) consist of either a neutron star or a black hole with a low-mass ($\leq 2.5 M_{\odot}$) normal star (late-type). Since the low mass star lacks a strong stellar wind, the mass accretion is thought to take place via the Roche lobe overflow. The lower luminosity systems of LMXBs (10^{36}–10^{37} ergs^{-1}) typically have an orbital period of $\leq$15 hr and exhibit type I X-ray bursts. The orbital period of higher luminosity systems of LMXBs ($\sim 10^{38}$ ergs^{-1}) is still unknown, since many of them are located in the optically obscured Galactic bulge region.

Most of the low mass X-ray binaries have not been observed any X-ray pulsations, and only 5 sources among $\sim$150 low mass X-ray binaries are cataloged as the low mass X-ray binary pulsars (Liu et al. 2001). This implies the neutron star of LMXBs have weak magnetic field ($\leq 10^{9}$G) so that the accretion flow of them are not affected by the magnetic pressure. Despite of the lack of coherent pulsations, many low mass X-ray binaries show irregular intensity variations on time scales from fractions of a second to hours, such as "Quasi Periodic Oscillations (QPOs)" and X-ray Bursts.

The time variations of QPOs are almost, but not quite, periodic in nature. This QPO feature is also seen in the high mass X-ray binary systems, such as Cen X-3. The study of these timing signatures, especially kHz QPOs since they arise from very near the compact object and are therefore sensitive to general relativistic effects, has been an active field of research since its discovery (see section 4 in this chapter).

The study of X-ray burst has also been an active field of research since its discovery in EXO0748-676 in 1975. X-ray burst is thought to be an unstable thermonuclear burning on the surface of the neutron star.

2.3.3 Mass Accretion onto the Neutron Star

Accretion powered pulsars are thought to be magnetized neutron stars with a normal star companion, the majority of which are high mass, early type stars (see Rappaport & Joss 1983; White et al. 1983; Nagase 1989; Buildsten et al. 1997 for reviews). After the discovery of the periodic pulsations from Cen X-3 (Giacconi et al. 1971a; Schreier et al. 1972) and Her X-1 (Tananbaum et al. 1972) with *Uhuru* satellite, soon these objects were interpreted as X-ray pulsars which were rotating, highly magnetized (B$\sim 10^{12}$ G) neutron stars on which the matter accreted from a binary companion (Pringle & Rees 1972; Davidson & Ostriker

1973; Lamb, Pethick, & Pines 1973; Ghosh & Lamb 1979a, b). In this section, we will review the mass accretion mechanism onto the neutron star.

In a simplified picture, a magnetosphere exists around the neutron star. Far from the magnetosphere, the accreting matter is transferred from the companion star via an accretion disk or via a stellar wind. Once the material has reached the point near the pulsar where the magnetic field is strong enough to constrain its flow, it falls onto the neutron star along the lines of the magnetic field. Then, the accreting matter gains approximately 200 MeV/nucleon while falling down the gravitational well of the neutron star with a radius of 10 km and a mass of $1.4M_{\odot}$. As observational evidence in support of this picture, we cite: (1) the ~40 mHz QPO from Cen X-3, detected by Takeshima et al. (1991), which was successfully explained by the beat frequency model (Alpar & Shaham 1985; Lamb et al. 1985; Shibazaki & Lamb 1987), and (2) the explanation of the average spin-up period as resulting from the interaction between the accreting matter and the magnetic field (Ghosh & Lamb 1979a). However, as yet no direct observational evidence on the magnetosphere has been discovered.

Since the neutron star (unlike the black hole) has a solid surface, the energy is radiated away and the resulting accretion luminosity is

$$L_{acc} = \frac{GM_{N.S}\dot{M}}{R_{N.S}}. \tag{2.2}$$

Here $M_{N.S}$ and $R_{N.S}$ is the neutron star mass and its radius, respectively, $\dot{M}$ is the instantaneous mass accretion rate, L_{acc} is the luminosity, and G is the gravitational constant. Based on the observational result of high mass accretion powered pulsar in the X-ray band, the luminosity of them varies over many orders of magnitude with the $L_{acc} \approx L_x \sim 10^{34} - 10^{39}$ ergs^{-1} range.

In general, the magnetic dipole moment of the neutron star of the accretion powered pulsar is thought to be $\sim 10^{30}$ G cm^3. As mentioned above, the accretion matter onto the neutron star becomes entrained on the strong magnetic field as it approaches the neutron star. The radius which is called Alfv́en radius, r_A, is found by equating the fluid stresses of the matter in the disk with the magnetic stress, and it is described as follows:

$$r_A = 1.6 \times 10^8 \, L_{38}^{-2/7} \varepsilon_{0.1}^{2/7} \mu_{30}^{4/7} \left(\frac{M}{M_{\odot}}\right)^{-1/7} \text{cm}. \tag{2.3}$$

Here L_{38} is the X-ray luminosity in unit of 10^{38} ergs s^{-1}, $\varepsilon_{0.1}$ is the energy conversion efficiency normalized by 0.1, μ_{30} is the magnetic dipole moment of neutron star in units of 10^{30} G cm^3, and M and $M_{\odot}$ are the mass of the neutron star and the solar mass, respectively.

Inside the magnetospheric radius, the magnetic stress dominates, and the ionized plasma

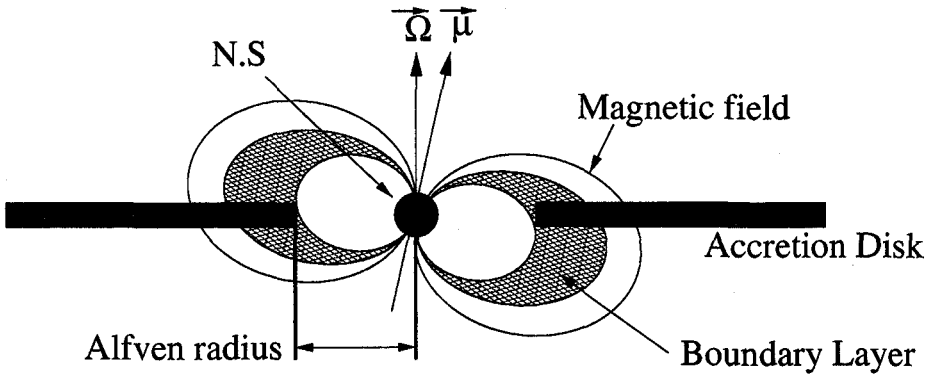

Figure 2.2: Side view of the accretion flow around the neutron star with an accretion disk. The magnetic field of the pulsar disrupts the disk at the magnetospheric radius, channeling plasma through the boundary layer to the neutron star magnetic poles (Ghosh & Lamb 1979a,b). Although not shown, the magnetic field is expected to be deformed away from a purely dipolar configuration by plasma in the disk at radii larger than the magnetospheric radius.

entrained on the magnetic field of lines is channeled onto the magnetic poles. This infalling matter onto the neutron star creates two hot spots on the neutron star surface which are the primary source of X-ray emission. If the magnetic and the spin axes are offset, then the X-ray emission will be modulated at the spin period. Thus, the pulsation is seen as the neutron star rotates. In general, the X-ray emission is also beamed, enhancing the modulation. Simple blackbody estimation of the emission region gives polar cap areas of typically $A_{polarcap} \sim 1\ \mathrm{km}^2$.

What happened at the magnetospheric radius depends on how the material is accreted. In the case of a simple wind accretion model, the accretion flow is quasi-spherical Bondi-Holey accretion (Bondi & Holey 1944; Davidson & Ostriker 1973) beyond the magnetospheric radius while inside the behavior of matter is governed by the magnetic field. For the accretion from a disk, which can form either the Roche-lobe overflow or the stellar wind, the picture is much more complex (Ghosh & Lamb 1979a,b). The magnetic field is strong enough to disrupt the inner edge of the accretion disk, sweeping up material and funneling it to the poles.

After the accreting matter entrained by the magnetic field, the matter falls onto the neutron star surface with free-fall velocities by ~0.5c. At high accretion rates ($L \geq 10^{36}$ erg s^{-1}), the infalling matter is halted above the neutron star surface, in a standing shock maintained by the radiation pressure (Davidson et al. 1973; Burnard, Arons, & Klein 1991).

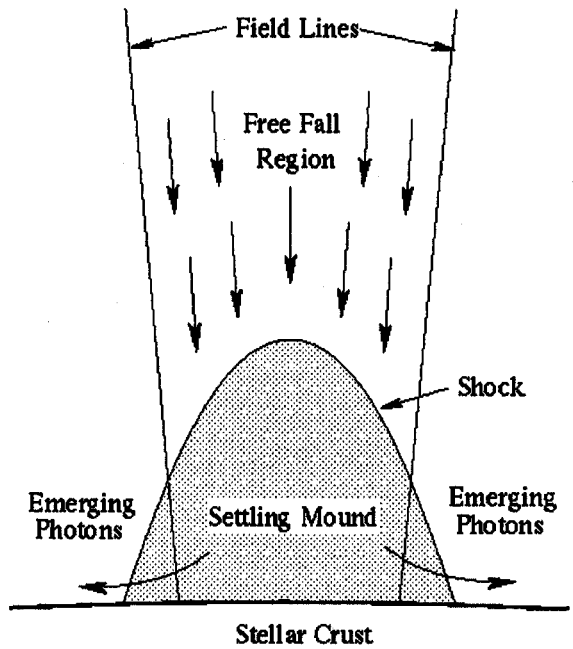

Figure 2.3: Diagram of the accretion flow near the surface of the neutron star, showing the infalling material, standing shock, setting mound, and emergent radiation (Burnard, Arons & Klein (1991)).

In the simplest case, where the accretion is uniform across the polar cap, the postshock emission region may be able to assume a simple mound structure (Figure 2.3). This accretion structure, which is dynamic in nature as the matter both accumulates from above and spreads out at the base, is expected to be inhomogeneous in both the temperature and the density. The steady state shape of the emission region will depend on the details of the accretion into the polar cap as well as the magnetic field configuration. The temporal pulse structure will depend not only on how the emission from the accretion mound is beamed but also on the relative locations of the hot spots on the neutron star surface and the viewing geometry as well.

2.4 Time Variabilities of X-ray Binary Pulsars

In this section, we will review the observational characteristics of X-ray binary pulsars, focusing on time variabilities in the X-ray energy range.

Together with X-ray spectroscopy, the study of time variabilities of XRBs has been one of the very few ways to obtain direct information about the physical circumstances in the vicinities of the compact objects.

In addition to periodic variations, aperiodic variations of Black hole candidates such as QPOs, kHz QPO, and noise have reported (e.g., Miyamoto et al. 1988; van der Klis et al. 1997, 1999). X-ray binary pulsars also show such aperiodic variations as well as periodic variations. Here, the periodic variation means both the coherent pulsation and the long-term variation, such as the spin-up/down of the pulse period (see section 6 in this chapter) and the orbital period change (see details in the chapter 4). The coherent pulsation appears as a series of spikes in power spectral densities (PSDs) corresponding to the fundamental and higher harmonics which is originated from the time variation due to the neutron star rotation. The pulse profile of each pulsar is considered to be a function of geometry of the pulsar system (see White et al. 1983 for a review).

Here, we will review the aperiodic variation of X-ray binary pulsars, such a QPO and kHz QPO. At last of this section, we will also introduce the time lag, which is the main subjects of this thesis.

2.4.1 Aperiodic Time Variation

As an example, Figure 2.4 shows the PSD obtained from Cen X-3 with *Ginga* satellite (Takashima et al. 1991). In addition to the periodic variation around 208 mHz, the aperiodic variation (the broken power-law component (the broken (turn over) frequency, μ_{to},

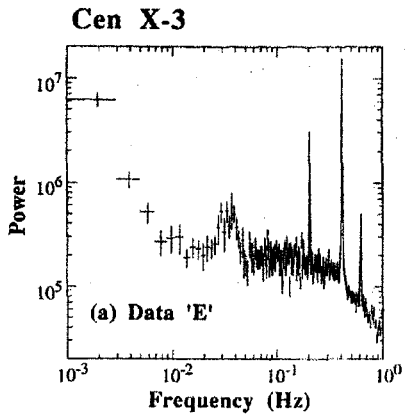

Figure 2.4: QPO feature around 35 mHz obtained by *Ginga* can be clearly seen (Takeshima et al. 1991). Over 10^{-1} Hz, three peaks which correspond to the pulse period(4.8s = 0.21Hz) and its harmonics, respectively.

of 0.41 Hz) in this PSD above the pulsation frequency, the flat part below the pulsation frequency, additional power-law component at lower frequency, and the QPO feature around 35 mHz) are clearly seen.

Takeshima (1992) reported a strong correlation between the turn over frequency of the power-law component of PSDs, μ_{to}, and the pulse frequency among 10 accretion powered pulsars (see Figure 2.5) would seem to suggest that there was a relation between the Kepler frequency, μ_K, at the magnetospheric radius and the time scale of the noise, as, under the assumption that the pulsars on average spin at roughly their equilibrium period, μ_K is predicted to be, on average, roughly equal to the pulse frequency. However, the relative constancy of μ_{to} in EXO 2030+375 over a large range in X-ray intensity is in contradiction with this (van der Klis 1995). This power-law component in PSD has considered to relate to the X-ray emission mechanism in X-ray binary pulsars, and Takeshima (1992) also suggested a periodic modulation of the accretion rate at the Alfv́en shell as a physical model to explain this power-law component: The matter accumulation and the accretion onto the neutron star alternately takes place at the Alfv́en shell. At the phase of the matter accumulation, the Rayleigh-Taylor instability and/or the Kelvin-Helmholtz instability is possible to generate a random noise, and a thermal relaxation of the inhomogeneity will introduce a correlation into the time variability. Then, at the phase of the accretion of the accreting matter, the correlation will diminish. However, the complete physical model to explain this power-law component in PSD have not determined yet.

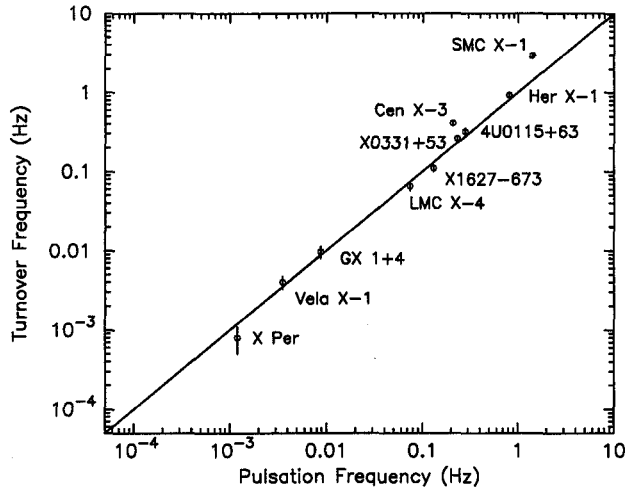

Figure 2.5: The turnover frequency of the PSD is plotted as a function of pulsation frequency. This turnover frequency is consistent with the pulsation frequency within a factor of two. (Takeshima et al. 1992)

Quasi-Periodic Oscillations (QPOs)

Since the discovery of quasi-periodic oscillation (QPO) from GX 5-1 with EXOSAT (van der Klis et al. 1985), QPO with centroid frequencies of about a few tens of mHz to a few hundreds Hz have been detected in many X-ray binaries. In order to explain QPO feature, the beat-frequency model have been applied (Alpar & Shaham 1985; Lamb et al. 1985; Elsner, Shibazaki, and Weisskopf 1987; Shibazaki et al. 1987) and partly have succeeded to explain it. In this model, the QPO sources is assumed to be weakly magnetic neutron stars accreting from Keplerian disks in which there are density and magnetic-field fluctuations. Interaction of the magnetosphere with fractions in the inner disk causes the mass accretion rate and hence the X-ray luminosity to vary at a harmonic of the beat frequency of the revolution of the plasma in the magnetospheric boundary layer and the rotation of the neutron star.

In some XRBs, the relation between the QPO frequency and the X-ray intensity is strongly positively expressed with either a linear or a power law (Figure 2.7), but this result depends on X-ray energy band. But, not much work has been done yet in relating QPO frequency to physically meaningful X-ray spectral components or even the X-ray luminosity.

kHz QPO

After the launch of *RXTE* which has the largest effective area and a reasonable time resolution (see chapter 3), the kHz QPO was discovered (van der Klis et al. 1997). So far, kHz

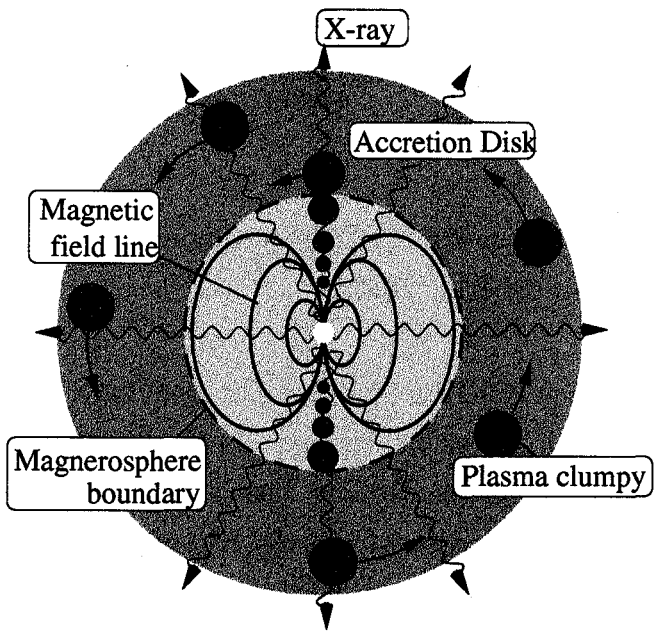

Figure 2.6: The beat-frequency model of QPOs. This shows the inner part of the accretion disk surrounding the neutron star's magnetosphere. Both are rotating rapidly, but accretion of plasma clumps onto the neutron star can only take place when a clump finds itself over the pole of the neutron star. This occurs at a frequency which is difference between the neutron star's spin frequency and the orbital frequency of the inner disk (Philip et al. 1995).

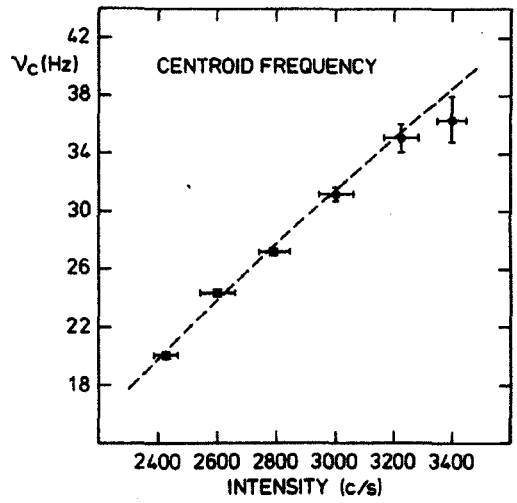

Figure 2.7: The relation between the QPO frequency and the X-ray intensity (1–20 keV) obtained with GX 5-1. (van der Klis. 1985a).

QPO has discovered in dozen of XRBs (van der Klis 1999 for a review), including Cen X-3. Figure 2.8 shows the kHz QPO near 330 Hz and 760 Hz discovered in Cen X-3 (Jernigan et al. 2000). In early works, the magnetospheric beat frequency model was implied when the beat frequency model was mentioned (e.g., van der Klis et al. 1996; Strohmayer et al. 1996), but this model has not recently been applied much to kHz QPOs. In stead of this model, the sonic point beat-frequency model of Miller et al (1996, 1998), the relativistic precession model of Stella and Vietri (1998, 1999), the photon bubble models (Klein et al. 1996), and the disk transition layer models (Titarchuk et al. 1998, 1999) have been strongly argued for the model of the kHz QPO.

It is beyond the scope of this work to provide an in-depth discussion for each model here. Then, we only introduce the photon bubble model to apply for the kHz QPO discovered in Cen X-3 (Jernigan et al. 2000). In this photon bubble model, the mass accretion takes place by way of a magnetic funnel within which accretion is super-Eddington, so that photon bubbles form which rise up by buoyancy and burst at the top of in quasi periodic sequence (Klein et al. 1996).

Time lags

Before the discovery of kHz QPOs with *RXTE,* the study of these aperiodic variabilities, time lags and QPOs, have been investigated mainly for black hole candidates. One of the

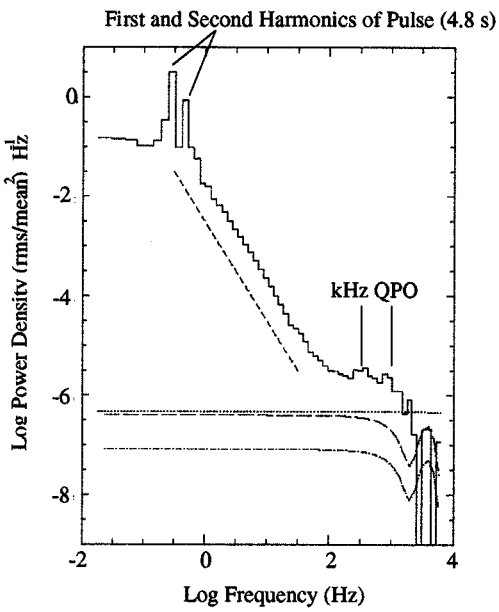

Figure 2.8: Power spectrum of Cen X-3 showing double kHz QPO peaks (Jernigan et al. 2000). The dotted curve shows an estimate of the upper limit to the level of the dead-time corrected Poission level. The long-dashed curve just below the dotted curve shows the upper limit to any additive contribution from the background.

most important result of the study of the aperiodic variation on black hole candidates is the discovery of time lags.

The X-ray emission mechanism of the black hole candidate in its low state had thought to be the inverse Compton scattering of low energy photons by a high temperature plasma cloud situated near the black hole.

But, using Fourier cross spectral techniques which allows to study the frequency dependence of the time lag and makes the basic phenomenology more clearer than using the cross correlation function, variations in higher energy X-rays lag those in lower ones (Miyamoto et al. 1988; Kitamoto et al. 1989). Their results showed that the time delays could not be due to the inverse Compton scattering, and they suggested that the X-ray emitting plasma was heating up near the black hole and disappeared suddenly into the black hole.

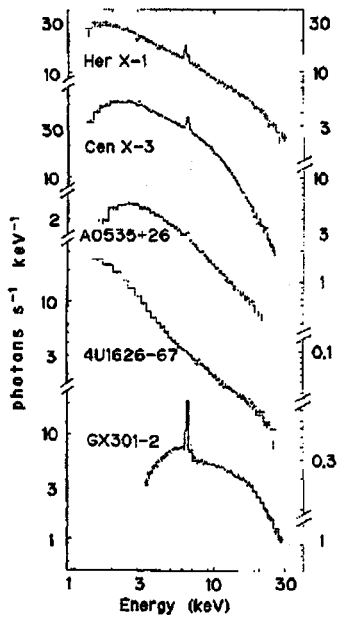

Figure 2.9: .

Phase averaged energy spectrum of five accretion powered pulsars observed by *Tennma* (Nagase et al. 1989). An iron lines around 6.4 keV are seen except for 4U 1626-67.

2.5 X-ray Spectrum of Accretion Powered Pulsars

In this section, we will review both observational characteristics of the X-ray spectrum of accretion powered pulsars and their emission mechanism. Figure 2.9 shows the typical energy spectram obtained from five accretion powered pulsars.

As seen in Figure 2.9, the pulse averaged spectrum of accretion powered pulsars are typically nonthermal and extend upto the medium to the hard X-ray energies. A fairly flat power law shape (photon index $\alpha \sim 0.8$–1.5) is often encountered above a few keV, which becomes much steeper above a break or a cut-off energy $E_c \sim 15$–25 keV. This drop-off sometimes shows an exponential shape (e.g. Joss & Rappaport 1984).

$1\mathrm{km}^2$

In general, at lower energies, the energy spectrum is absorbed by the interstellar medium, in which heavy elements provide bound-bound, bound-free transition and so on whose cross section typically behave toward lower energies as $(E/E_L)^{-3}$ where $0.1 \leq E_L \leq$ few keV is the line or edge energy. As a function of pulse, the continuum above a few keV often shows regular variations of the photon index α and of the cut-off energy E_c.

Many accretion powered pulsars show line emissions around 6.4 keV, ascribed to incom-

pletely ionized iron fluorescence transitions arising in a relatively cooler plasma (White et al. 1983; Nagase 1989). The plasma responsible for this is probably located neighborhood of the neutron star, either near the Alfv́en shell or in the stream of matter coming from the companion. The example of these emission lines is introduced later in this section, and we will discuss on their emission region in this thesis. The equivalent width of this iron fluorescence feature is typically $\geq$ 100 eV, with a relatively narrow line width $\delta E \leq 0.5$ keV. Recent observations with *ASCA*, *Chandra*, and *XMM-newton*, have revealed, so many lines and absorption structure at lower energies, $\leq$ 2 keV. These line features are effected by metals in the stellar wind or in the circumstellar gas around the neutron star (e.g., Liedahl et al. 2000).

The absorption by circumstellar gas around the neutron star causes a turnover at lower energies, and the energy at which this occurs is variable when the gas optical depth changes, as is the case for occupation by the companion star or the accretion flow. As seen in high mass X-ray binary pulsar Vela X-1, the circumstellar absorption varies largely through the eclipse ingress and egress (Nagase et al. 1989).

At the high X-ray energy $\geq$20 keV, cyclotron lines which were suggested by Basko & Sunyaev (1975) may be displayed. This feature was, for the first time, confirmed in the hard X-ray spectrum of Her X-1 (Trümper et al. 1978; Voges et al. 1982) which was interpreted as a cyclotron absorption line at 40 keV or an emission line at 58 keV. Recent X-ray observation with *Ginga*, *Mir-Kvant*, *CGRO*, *BeppoSAX*, and *RXTE* have established $\sim$20 more pulsars as cyclotron pulsars (Makishima et al. 1999).

Table 2.2: Summary of the currently known cyclotron X-ray pulsars (Originated from Makishima et al. 1999)

Object	E_a	E_c	Status	B(10^{12} G)
4U 0115+63 (1990)	11.3±0.6/22.1±0.4	7.7±1.3	Firm	1.0
4U 0115+63 (1991)	15.6±0.4/...	8.8±0.9	Firm	1.3
4U 1907+09	18.9±0.7/39.4±0.6	14.2±0.5	Firm	1.6
4U 1538-52	26.2±0.2/...	14.2±0.6	Firm	1.8
Vela X-1	24.5±0.5/56±2	18.8±0.8	Firm	2.1
Cen X-3	25.8±0.5	14.8±0.4	Firm	2.2
Cen X-3 (this work)	26.4±0.3/...	13.30±0.03	Firm	2.27
X0331+53	27.2±0.3	13.9±0.6	Firm	2.3
Cep X-4	28.8±0.4/...	17.6±0.4	Firm	2.5
Her X-1	33.1±0.5	20.0±0.5	Firm	2.9
4U 1626-67	38.1±0.9	21.1±0.4	Firm	3.3
A0535+26	$\sim 50/110^{+2}_{-4}$	24±2	Firm	4.4
GX 301-2	35.6±1.6	19.6±0.8	Probable	3.1
GS 1843+00	19.8±2.1	19.8±1.1	Possible	1.7
LMC X-4	21.4±1.2	16.1±0.5	Possible	1.8
X2259+586	4.20	...	Doubtful	0.6
4U 0352+309(X per)	$28.6^{+1.5}_{-1.7}$	...	Firm	2.5
XTE J1946+274	$36.2^{+0.5}_{-0.7}$	...	Firm	3.1

2.5.1 X-ray Emission Mechanism of Accretion Powered Pulsars

In this subsection, we will review the emission mechanism of the continuum X-ray and the iron lines observed around ~6.4 keV of the accretion powered pulsars.

Continuum X-rays

Many authors have tried to explain the continuum X-ray emission mechanism as the emission from the accretion column and the general shape of the continuum above several keV, which often resembles a power law with a cut-off above some energy typically in the 10–30 keV and in some notable cases has a cyclotron features just above the cut-off energy (e.g., Araya & Harding 1999; Mészaros 1995; Nagel 1980; Kii 1986; Bulik et al. 1992).

As emphasized by Nagase (1989) and Clark et al. (1990), when a line like structure (hereafter only in this section, line) is present in the energy spectrum, its energy is typically smaller by a factor of ~0.5–0.7 of the cyclotron energy (see also Figure 2.10). Nagel (1981) presents, applying the reasonable optical depth of the accretion column, the line will be negative feature, looking like an absorption line although in reality what happens is that photons are being scattered out of the line of sight. Then, to explain the emission mechanism from the accretion column, it is important to see whether the reasonable optical depths, temperatures, and densities one can get a flux comparable to that observed, with the ratio of continuum (below the cut off energy) to line flux similar to that observed.

For the plasma parameters in the accretion column, one can take the density in the accretion column at least as large as the free fall density $\rho = \dot{M}/2Av_{ff} \sim 10^{-4}L_{38}$ g cm^{-3}, where the v_{ff} is the free fall velocity and A is the X-ray emitting area. The optical depth somewhere between the Thomson depth of free-fall matter across the column width of ~1 km and the nuclear stopping length (τ_T) of infalling protons on atmospheric protons ~55 g cm^{-2}, i.e, $6L_{38} \leq \tau_T \leq 22$. In order to get a sufficiently realistic looking line profile and line depth in the energy spectrum, it is necessary to use cross sections which include at least thermal and vacuum effects. With these, the total flux, the shape of the continuum ratio of the energy spectrum can be reproduced with reasonable parameters (Mészaros and Nagel 1985a). In above calculation, a source of soft photons at energies $E_s \leq 1$ keV is assumed, in order to provide the low energy portion of the spectrum. These soft photons are up-Comptonized by the hot electrons in the atmosphere to produce a power-law shape energy spectrum between E_s and $E \sim kT$. This source of the soft photons is not still clear, although photons from the surface of the neutron star could produce radiation at these energies.

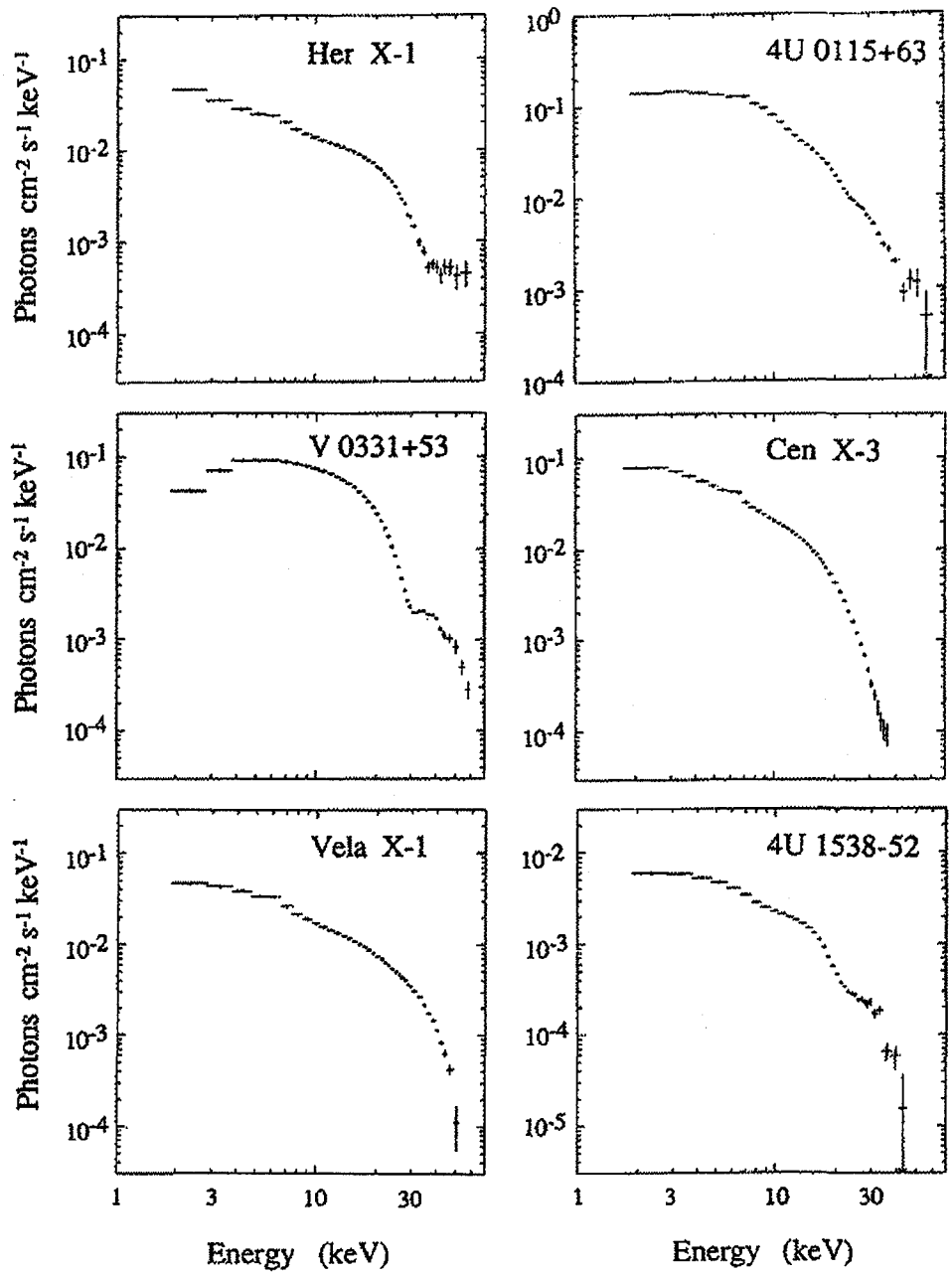

Figure 2.10: The phase averaged energy spectrum of six accretion powered pulsars observed with *Ginga*. Cyclotron line features are clearly seen in the energy spectra of Her X-1, 4U 0115+63, V 0331+53, and 4U 1538-52.

2.6 Magnetic Fields of Neutron Stars

Neutron stars have long been argued to process surface magnetic field of order 10^{12} G on grounds of magnetic flux conservation during the gravitational collapse of supernovae cores (Woltjer 1964; Hoyle, Narlikar & Wheeler 1964; Pacini 1967). At these magnetic field strengths, the characteristic electron cyclotron resonance energy of the field is of order 10% of the electron rest mass, implying that relativistic effects are becoming important. Also, under these conditions, the electron motion transverses to the magnetic field is quantized. The surface of the neutron star itself is at the bottom of a deep gravitational well, with a gravitational acceleration. The combination of relativistic particle energies and quantizing magnetic fields requires a quantum electrodynamics (QED) for the description of the physical processes.

There are several methods for measurements of the magnetic field B. As described before, for rotation powered pulsars which are assumed to be emitting due to magnetic dipole radiation, the magnetic fields are inferred from observations of the spin period, P_{spin}, and period derivative, $\dot{P}_{spin}$ (see section 2.2). These estimations give a dipole magnetic field in the 10^{11}–10^{13} G range. For accretion powered pulsars, there are currently two methods for determining the magnetic field strength. The first method is the measurement of hard X-ray spectral lines or cyclotron lines. The second method is an estimation using an accretion torque theory from the observation spin period, P_{spin}, and the mass accretion rate inferred from the measured flux (Ghosh & Lamb 1979a,b).

2.6.1 Cyclotron Resonance Scattering Features (CRSF)

Cyclotron lines have been detected in a number of accretion powered pulsars (Nagase 1989; Mihara 1995; Makishima et al. 1999; Cobrun 2000), and cyclotron lines are only the direct observational evidence for the magnetic field of the neutron star.

The spectral feature of cyclotron lines is generated by the scattering of resonant photons with the electrons embedded in the magnetosphere of accretion pulsars. This gives the absorption features in the X-ray spectrum, with the centroid of the line at the cyclotron energy. The cyclotron energy is set by the magnetic field strength, and the surface field strength of most neutron star is in the hard X-ray band.

Classically, electrons moving in a uniform magnetic field are free to move along the magnetic fields, while the electron motion transverses to the field is considered to circular motion. The net result is a helical motion, with the radius of the circular component, r_{gy}, given by

$$r_{gy} = \frac{cp_\perp}{eB}. \tag{2.4}$$

Here $p_\perp$ is the electron momentum perpendicular to the field and B is the magnetic field strength. This radius, r_{gy}, decreases with increasing B, until eventually it is of order the de Broglie wavelength ($\lambda = \hbar/p$) of the electron and quantum mechanical effect dominates. Once this is the case, the transverse motion of the electron is quantized into Landau levels. In the non-relativistic limit the n^{th} Landau level is given by

$$E_n = (n' + \frac{1}{2} + s)E_c. \qquad n' = 0, 1, 2, ... \tag{2.5}$$

Here $s = \pm\frac{1}{2}$ is the electron spin and E_c is the cyclotron energy. The non-relativistic cyclotron resonance energy, in terms of the magnetic field B and for $n' = 0$ and $s = -\frac{1}{2}$ is :

$$E_c = \frac{\hbar e}{m_e c}B. \tag{2.6}$$

Or equivalently, scaled by a 10^{12} G field and given in unit of keV, is

$$E_c = 11.6\frac{B}{10^{12}\,\mathrm{G}}\ \mathrm{keV}. \tag{2.7}$$

In equation (2.5), the $(n' + \frac{1}{2} + s)$ term will always result in an integer, allowing the equation to be simplified. Therefore the harmonically spaced Landau levels are given by:

$$E_n = nE_c, \qquad n = 0, 1, 2, ... \tag{2.8}$$

The scattering process produces when a resonant photon is absorbed by an electron in the $n = 0$ ground state which is then excited to an $n \geq 1$ Landau level (depending on whether the photon is at a single or higher multiple of the cyclotron energy). In a plasma that is cool compared to the cyclotron energy, the lifetime of electrons above the $n = 0$ ground state is very short. The radiative cyclotron de-excitation rate is given by (Latal 1986),

$$\nu_r = (\frac{\alpha m_e c^2}{\hbar})(\frac{B}{B_{QED}})^\beta. \tag{2.9}$$

Here $\alpha = e^2/(4\pi\hbar c)$ is the fine structure constant, $B_{QED} = (\mathrm{m}_e^2 c^3)/(\hbar e) \simeq 4.4\times10^{13}$ G is the QED quantum field scale, and $\beta = 2$ for $B < B_{QED}$. In general, accretion powered pulsars have a strong magnetic field $B \sim 10^{12}$ G, then $\nu_r \sim 10^{15}\ (B/10^{12}\mathrm{G})^2\ \mathrm{s}^{-1}$. So an excited electron immediately returns to the ground state by emitting a resonant photon. This prompt returns to the ground state is why, at least for the $n = 1$ to $n = 0$ transition, the process is scattering rather than the true absorption. Because of this, and the fact

that few cyclotron line sources exhibit any features beyond the fundamental, these lines are known as Cyclotron Resonance Scattering Features (CRSFs).

For higher (n >1) harmonics, the decay process is slightly more complex. While the electron may decay directly back down the ground state, it can also cascade down through the Landau levels, producing n photons each with energy E_c keV. This process is known as photon spawning, and is the decay channel preferred in $B < B_{QED}$ field. Due to the prompt decay from all Landau levels, most of the electrons in the scattering region are in the $n = 0$ ground state with aligned spin ($s = -\frac{1}{2}$).

Since the radius of the neutron star is only a few (2-3) Schwartzschild radius, general relativistic effects are important in the emission region. In particular, the CRSF feature will be redshifted by the neutron star gravitational field such that the observed energy, as indicated by a scattering feature in the energy spectrum, is less than the true energy. The correction term is given by:

$$E_c^{obs} = E_c(1+z)^{-1}, \tag{2.10}$$

where

$$(1+z)^{-1} = (1 - \frac{2GM_{N.S}}{R_{N.S}c^2}), \tag{2.11}$$

and z is the gravitational redshift. Assuming a canonical neutron star, $(1+z)^{-1} \simeq 0.76$.

As the cyclotron energy becomes comparable to the electron rest mass, or alternatively as the magnetic field B approaches B_{QED}, relativistic effects start to become important. In this regime, the cyclotron resonance energy is given by (Harding & Daugherty 1991);

$$E_c = m_e^2 c \frac{\sqrt{1 + 2n(B/B_{QED})sin^2\theta} - 1}{sin^2\theta} \tag{2.12}$$

where θ is the angle of the incident photon to the magnetic field. This equation reduces to equation (2.6) in the $B \ll B_{QED}$ limit. The dependence on θ, however, leads to slightly non-harmonic line spacing in the relativistic case which is unlike the classical limit. Since these energies depend sensitively on the photon's propagation angle with respect to the magnetic field, the emergent spectral features are influenced heavily by the spatial distribution of electrons (the plasma "geometry") and by the orientation of the magnetic field inside the scattering region.

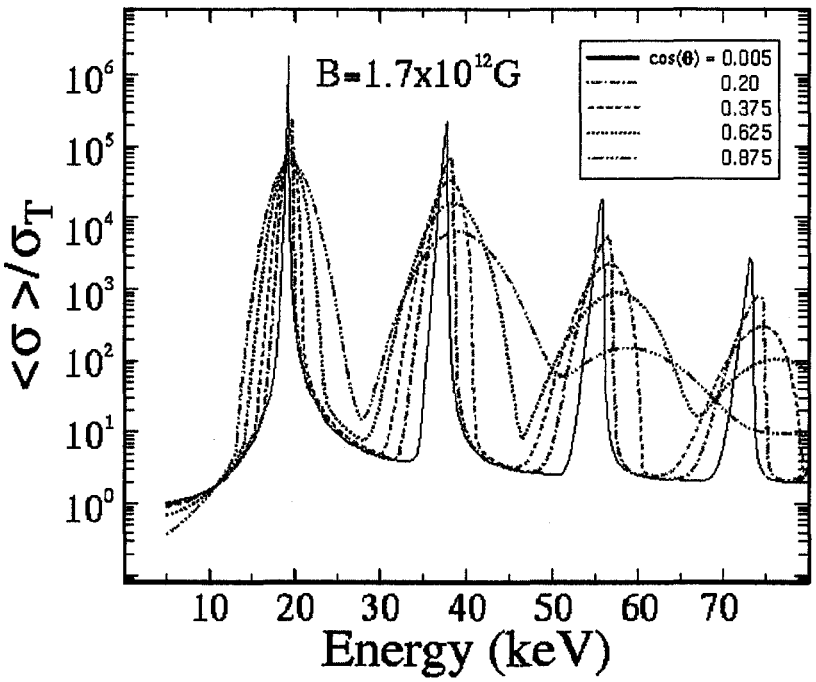

Figure 2.11: Cyclotron scattering cross sections (in terms of the Thomson cross section σ_T) for a $B = 1.7\times10^{12}$ G field. The angle θ is defined as the angle between the magnetic field and photon propagation direction. The tallest, narrowest profile corresponds to $\cos\theta = 0.005$, where the photons travel nearly perpendicular to the field. As the propagation angle decreases, the cross sections become broader and shallower due to thermal motions ($kT_e = E_c/4$ in the simulations) of the electrons along the field lines (Cobrun 2001).

The Scattering Cross Section

So far, in order to explain the CRSFs, many theoretical attempts have been investigated (Mészaros & Nagel 1985a,b; Alexander & Mészaros 1989; Isenberg, Lamb & Wang 1998a,b; Bulik et al 1995; Araya & Harding 1999; Araya-Góchez & Harding 2000; Cobrun 2001), and the cross sections have been calculated by them. Cobrun (2001) calculated the relativistic, magnetic Compton scattering cross section as a function of angle, the results of which for a $B = 1.7\times10^{12}$ G field are shown in Figure 2.11.

The cross section depends on polarizations and directions of incoming and outgoing photons is represented by a linear combination of the following two modes: 1. Extraordinary Mode: the E-vector is perpendicular to magnetic field B, and 2. Ordinary Mode: the E-vector is parallel to B. By integrating over outgoing angles, the scattering cross section

is divided into four combinations of the polarizations of incoming and outgoing photons (Ventura 1979): 1→1, 1→2, 2→1, and 2→2, as a function of the angle θ between the incoming photon direction and the magnetic field.

The remarkable point is that the 1→1 cross section at θ=0^o can be represented by a simple form:

$$\sigma(E) = \sigma_T \frac{E^2}{(E - E_c)^2 + W^2} \tag{2.13}$$

where σ_T is the Thomson cross section, E_c is the resonance energy, and W is the width of the resonance. The incident spectrum I_0 is modified as $I_0(E)\exp(-\sigma(E)N_H)$, where N_H is the column density of the scattering plasma. To fit the obtained energy spectra of CRSF, Mihara et al. (1990) introduced the CYAB (CYclotron ABsorption) model. Mihara et al. (1990) replaced the normalization with $D \equiv \sigma_T\ N_H(E_c/W)^2$, as $\sigma(E)N_H$ takes the value D at $E = E_c$. The parameter D is dimentionless and called as "Depth".

$$CYAB(E) = \sigma(E)N_H = \frac{D(\frac{W}{E_c}E)^2}{(E - E_c)^2 + W^2} \tag{2.14}$$

2.6.2 Theory of Accretion Torques

As shown in Figure 2.12, pulse periods of some accretion powered pulsars decrease their spin period monotonically, while the others show the increase with time or fluctuate randomly. This is because the neutron star interacts strongly with the accreting matter via the its strong magnetic field, exchanging its angular momentum in a complex manner. The simple model to explain these spin-up/down episode was pioneered by Pringle and Ress (1972) and Rappaport and Joss (1977). Then the detailed theoretical treatment of the model, so-called accretion torque theory, was formulated by Ghosh and Lamb (1979a,b). Using this accretion torque theory, magnetic field strength of accretion powered pulsars can be estimated, in addition to measurements of CRSFs.

Due to the strong ($\sim 10^{12}$ G) magnetic field of the neutron star, the accretion flow from the companion star becomes disrupted at a distance r_A (Alfv́en radius), where the magnetic stress becomes comparable to the ram pressure of the accreting matter. Thus, r_A is given by (Pringle & Rees 1972; Lamb, Pethick, & Rines 1973).

$$\frac{B(r_A)^2}{8\pi} \approx \frac{1}{2}\rho(r_A)v(r_A)^2, \tag{2.15}$$

ρ is the density of the accreting matter and v is its velocity. Assuming the dipole magnetic field, spherical accretion and free fall velocity of the accreting matter, r_A is given by

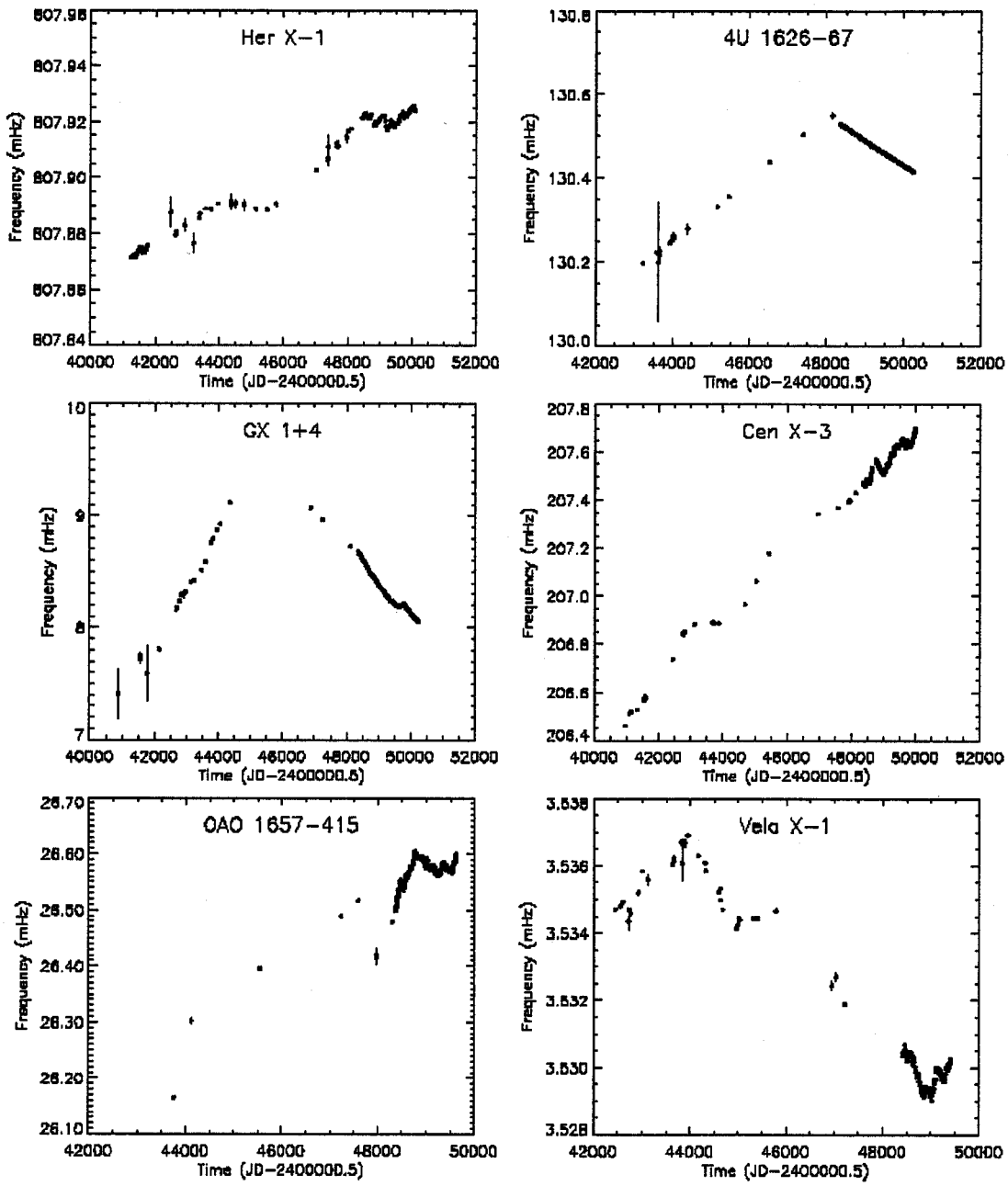

Figure 2.12: Long term frequency history for some pulsars detected by *BATSE*. (Bildsten et al. 1997).

$$r_A = (\frac{\mu^4}{2GM_{n.s}\dot{M}^2})^{1/7} \simeq 6.8 \times 10^8 {\mu_{30}}^{4/7} (\frac{10^{-10} M_\odot \mathrm{yr}^{-1}}{\dot{M}})(\frac{1.4 M_\odot}{M}). \quad (2.16)$$

$\dot{M}$ is the mass accretion rate, and μ_{30} is the magnetic dipole moment of a neutron star in units of 10^{30} G cm^3, and M is the mass of the neutron star.

In many situations, the accreting matter possesses too much angular momentum to accrete radially, but first forms an accretion disk in which excess angular momentum is removed through viscous forces. In this case, the distance from the star at which the accretion flow becomes disrupted is modified to $r_m = \xi r_A$. Estimates of the model dependent dimentionless parameter, ξ, range from $\xi = 0.52$ (Ghosh and Lamb 1979a,b) to $\xi \approx 1$ (Arons 1993; Ostriker and Shu 1995; Wang 1996). As long as r_m is less than the co-rotation radius,

$$r_{co} = (\frac{GMP_{spin}}{4\pi^2})^{1/3}, \quad (2.17)$$

at which the Keplerian disk co-rotates with the neutron star, accretion can occur. However, when $\dot{M}$ is decreased, r_m increases and centrifugal inhibition of accretion occurs when $r_m > r_{co}$. In addition, if the accreting matter couples to the neutron star magnetic field which tries to enforce co-rotation, the former will be expelled, carrying away angular momentum and resulting in spin-down. This phenomenon is known as the propeller effect (Illarionov and Sunyaev 1975).

The condition of a rotational equilibrium of the pulsar can be expressed $r_m = r_{co}$. Substituting equation (2.3) and (2.17), and converting the mass accretion rate into the X-ray luminosity, L_{37} in unit of 10^{37} erg s^{-1}, the equilibrium rotation period, P_{eq}, is expressed as

$$P_{eq} = 1.35\, \mu_{30}^{6/7} L_{37}^{-3/7} R_6^{-3/7} (M/M_\odot)^{-2/7} \quad \mathrm{s} \quad (2.18)$$

where R_6 is the radius of the neutron star in unit of 10^6 cm.

When $r_m < r_{co}$, this theory can further predict the torque exerted from the accreting matter to the neutron star, and relate it to the rotational period change $\dot{P}$ as

$$-\dot{P} = 5.0\, n(\omega_s) \mu_{30}^{2/7} R_6^{6/7} (M/M_\odot)^{-3/7} I_{45}^{-1} (P L_{37}^{3/7})^2 \quad \mathrm{s/yr}, \quad (2.19)$$

where I_{45} is the moment of the inertia of the neutron star in unit of 10^{45} g cm^2, $\omega_s = \Omega_s/\Omega_K(r_0)$ is called fastness parameter ($\Omega_K(r_0)$ and Ω_s is Keplerian angular velocity of the matter at r = r_0 and the angular velocity of the neutron star, respectively), and the function of $n(\omega_s) = (1-\omega_s/\Omega_s)(1-\omega_s)$ is called the torque function. Since P, $\dot{P}$, and L_{37} are obtained by the observation, the magnetic field can be calculated by assuming R_6, M, and I_{45}.

2.7 Previous Observational Results of Cen X-3

Cen X-3 is the first detected X-ray binary pulsar (Giacconi et al. 1971). Since its discoveries, many rotation powered pulsars and accretion powered pulsars have been extensively investigated through *Uhuru* to present X-ray satellite, *BeppoSAX*, *RXTE*, *Chandra* and *XMM-newton*. With respect to Cen X-3, till early 1980 s, the fundamental parameters; spin period, P_{spin}, orbital period, P_{orb}, the mass of compact star, M_c, and the radius of the companion star, R_c, were determined by using timing analysis. Then, spectral analysis with the advent of space born X-ray detectors with a high spectral resolving power has given highly-detailed information about the circumstellar matter around the neutron star. In this section, we will review observational results of Cen X-3.

2.7.1 Before *Ginga* Observation

Before the observation of Cen X-3 with *Ginga* satellite, the main purpose of the observation had been to study the time variability due to the poor performance of the X-ray detector for the spectral analysis.

Chodil et al. (1967) first discovered Cen X-3 in May, 1967 at a flux of 0.7 photons cm^{-2} s^{-1} in the energy range of 2–9.5 keV with two proportional counters on board the rocket. The *Uhuru* satellite discovered 4.87 s pulsations from Cen X-3 in 1971 (Giacconi et al. 1971), and eclipses which recurred with the 2.08712±0.00004 d orbital period (Schreier et al. 1972). The optical companion star of Cen X-3 was soon identified as the O-type supergiant, V779 Cen, and measured the distance to Cen X-3 by ~8 kpc (Krezminski et al. 1974). Then this companion star was classified as O6.5 III, corresponding to an effective temperature of T_* = 39,000 K and an intrinsic luminosity of $L_* \sim 3\times10^5\ L_\odot$ (cf. Howarth & Prinja 1989). Hutchings et al. (1979) found this companion star had a spectral type that varied with orbital phase, ranging from O9 near X-ray eclipse to O6 at phase $\phi = 0.5$, and suggested this evidence of X-ray heating of the stellar surface on the side facing toward the neutron star.

By the timing analysis of Cen X-3, the duration of the X-ray eclipse and the amplitude of radial velocity of the companion star, the stellar parameters of neutron star and of its companion star have been determined using the Doppler analysis of the pulse arrival times (Rappaport & Joss 1983). The mass, M_c, and radius, R_c of the companion star are $20M_\odot$ and $12R_\odot$, respectively. A finite rate of change in orbital period, $\dot{P}_{orb}/P_{orb}$, had been tried to determine by many authors (Schreier et al. 1973; Fabbiano and Schreier 1976; Fabbiano and Schreier 1977; Tuohy 1976; van der Klis, Bonnet-Bidand & Robba 1980; Howe et al.

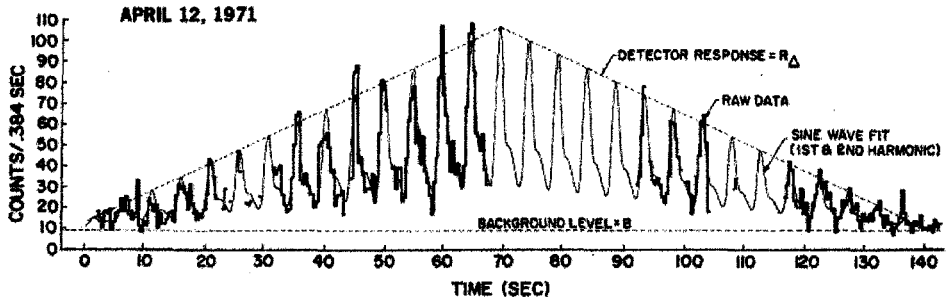

Figure 2.13: Light curve obtained from Cen X-3 observed with *Uhuru* satellite (Giacconi et al. 1971).

1983; Murakami et al. 1983; Kelley et al. 1983), and Kelly et al. (1983) was reported to be -1.8×10^{-6} yr^{-1}. The other important result of timing analysis was the discovery of the QPO using *EXOSAT* (Tennant et al. 1988).

The iron line emission in many binary pulsars including Cen X-3 had been discovered with *HEAO1* and *OSO8* (Pravdo 1979; White et al. 1983; see for review Nagase 1989), and the latter observations with gas scintillation proportional counters on *EXOSAT* and *Tenma* identified their lines as predominantly fluorescent, with energies around 6.4 keV, characteristic of reprocessed emission from "cold" material (Inoue 1985; Nagase 1985; Makishima 1986; Nagase 1989). The reradiation process of the X-ray continuum in the gaseous shell at the Alfv́en surface was begun to interpret as one of the candidate of the emission mechanism of the iron line (Hatchett & Weaver 1977; Basko et al. 1978; Basko et al. 1980).

2.7.2 *Ginga* Observation

Many *Ginga* results on both the timing and the spectroscopic analysis were reported (Tsunemi et al. 1989; Takeshima et al. 1991; Nagase et al. 1992; Day et al. 1993b; Tsunemi et al. 1996).

Using timing analysis, a set of orbital parameters which confirmed the change in the orbital period known previously and yielded an improved rate of change of the orbital period: $\dot{P}_{orb}/P_{orb} = -1.738\times10^{-6}$ yr^{-1} (Nagase et al. 1992). Takeshima (1991) confirmed the QPO features in Cen X-3 and its centroid frequency was 35±2 mHz. This QPO frequency was successively explained by the beat frequency model (Alpar & Shaham 1985; Lamb et al. 1985; Shibazaki & Lamb 1987).

Nagase et al. (1992) detected iron lines around 6.4 keV, and they suggested that the iron line was predominantly due to reprocessing by a cold matter. The line intensities of 6.4 keV after egress increased by a factor 20 in less than 10 minutes, and they estimated the size of the region emitting the 6.4 keV line, $D_{6.4}$:

$$D_{6.4} \leq 3 \times 10^{10}\,\mathrm{cm}. \tag{2.20}$$

They also detected the 6.7 keV K_α line from helium-like iron during the eclipse. The intensity of this 6.7 keV iron line which did not change during the eclipse indicate that its origin of the emission region was extended larger than the companion ($R_c = 12R_\odot$). Thus, they suggested the size of the region which emited the 6.7 keV iron line, $D_{6.7}$, was

$$D_{6.7} > 8 \times 10^{11}\,\mathrm{cm}. \tag{2.21}$$

In addition to Nagase et al. (1992), from both theoretical and observational point of view, Day et al. (1993a) also proposed that photoionization of the circumstellar wind by X-ray irradiation would be significant in Cen X-3.

Day et al. (1993b) discovered the pulsed iron line emission from Cen X-3, and discussed the constraints on the origin of the iron line imposed by their discovery and by the other observations. Until their work, no pulsations in the iron flux had been convincingly detected, and it was thought that the reprocessing region subtended a large solid angle at the neutron star. They derived the pulsed iron line equivalent width by ~100 eV and the column density of 10^{22} cm^{-2}. Their results were well explained if the material emitting the iron line partially enveloped the neutron star, by referring to the results of Inoue (1985) and Makishima (1986) (see Figure 2.14). Then they also suggested the Alfv́en shell was the possible candidate of the iron reprocessing region.

From above results, it is suggested that the Alfv́en shell around the neutron star is plausible reprocessing site for the 6.4 keV line, and the stellar wind from the companion star may be responsible for emitting the lines around 6.7 keV.

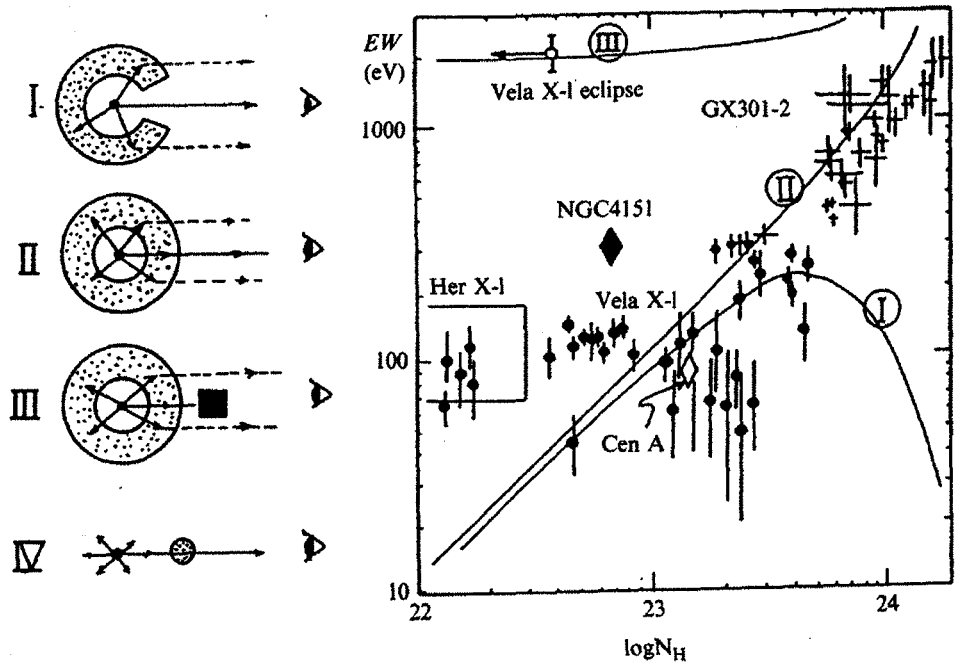

Figure 2.14: The relation between the column density and the equivalent width of iron line which depend on the source geometry (Makishima et al. 1986).

2.7.3 *ASCA* and the Recent Observations

Here we will review the observational results of Cen X-3 with a focus on *ASCA* observation in addition to the other observation, by *BBXRT*, *BeppoSAX*, and *RXTE*.

ASCA Observational Results

As shown in Figure 2.15, CCD camera, named SIS, on board *ASCA* satellite was succeeded, for the first time, to resolve three emission lines at 6.4 keV, 6.7 keV, and 6.97 keV clearly with unprecedented energy resolution at the iron K-energy band (FWHM $\sim$ 2%). At lower energies, lines from hydrogenic ions of Ne, Mg, Si, and S were also resolved (see Figure 2.15 (Ebisawa et al. 1996)).

From the spectral analysis, Ebisawa et al. (1996) confirmed that the 6.4 keV fluorescent iron lines could be emitted from the region close to the neutron star probably at r$\leq 10^{10}$ cm as indicated by Day et al. (1993b), since the ionization stage of 6.4 keV fluorescent iron lines should be less than about sixteen and the ionized parameter $\xi \equiv L/(nr^2) \leq 10^2$ erg cm s^{-1} (Kallman & McCray 1982). Based on the observed iron K-edge depth, corresponding to $\sim 4\times10^{23}$ cm^{-2}, Ebisawa et al. (1996) also proposed the Alfv́en shell or an optically thick accretion disk close to the neutron star are likely candidates for the origin of this fluorescent line and edge.

The ionization parameters for 6.7 keV and 6.97 keV were estimated to be $\sim 10^{3.4}$, then the size and the density of the plasma were estimated as $\sim$16 $R_\odot$ and $\sim 1.3\times10^{11}$ cm^{-3}, respectively.

The Other Observational Results

The other observational results were also reported by many authors (Audley et al. 1996; Audley et al. 1998; Santangelo et al. 1998; Jernigan et al. 2000; Kohmura, Kitamoto, & Torii 2001).

The QPO feature around 40 mHz were confirmed (Audley 1996; Kohmura, Kitamto & Torii 2001) with *BBXRT* and *RXTE*, and CRSF were detected 25.1$\pm$0.2 keV by *RXTE* (Audley 1998), $\sim$28 keV by *BeppoSAX* (Santangelo et al. 1998), and $\sim$26 keV by *RXTE* (Kohmura, Kitamoto, & Torii 2001) respectively. *RXTE* observed QPO feature both at $\sim$330 and at $\sim$760 Hz (Jernigan et al. 2000).

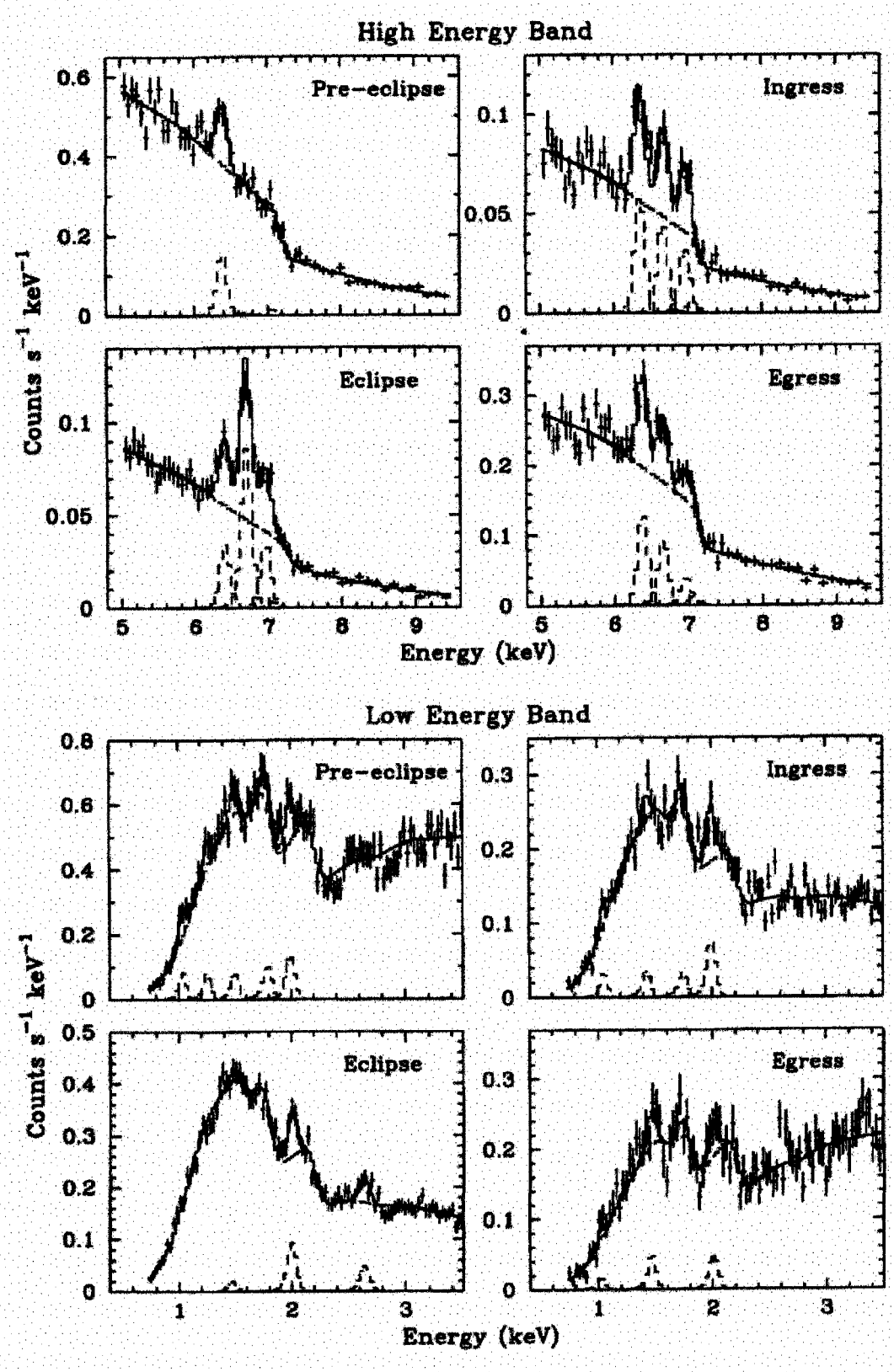

Figure 2.15: Energy spectra obtained by *ASCA* SIS. Upper four panel show the higher energy band (5–10 keV), and bottom four panel show the lower energy band (0.8–4.0 keV) for the pre-eclipse, ingress, eclipse, and the egress period. Model components (continuum and gaussian lines) are shown with broken lines.

Chapter 3

The Rossi X-ray Timing Explorer instrument

To study the timing variability and spectral behavior of X-ray binary pulsars, *RXTE* is the best X-ray satellite which provides us a high time resolution data with excellent statistics and a reasonable energy resolution. In this chapter we will review, entitled the *Rossi X-ray Timing Explorer*, outlines the instrument used to accumulate the spectral and timing information from Cen X-3.

3.1 The *Rossi X-ray Timing Explorer*

RXTE was launched on 1995 December 30 from Cape Canaveral, Florida. The spacecraft was designed and built by the Goddard Space Flight Center (GSFC). It was launched by a Delta II rocket that put *RXTE* into a low-earth circular orbit whose apogee and perigee were 580 km and 560 km, corresponding to an orbital period of about 90 min, at an inclination of 23 degrees. One of the major advantages of the *RXTE* is its maneuverability. The space craft can slew onto a source at 6°/min, allowing it to respond quickly to transient sources. Named after the pioneering Italian astrophysicist Bruno B. Rossi, the nominal lifetime of this mission was only two years, with the goal of five years. The satellite is currently in its 7th year of operation.

Unlike the current generation of X-ray telescopes, such as *ASCA*, *BeppoSAX*, *Chandra X-ray Observatory* and *XMM-newton*, *RXTE* dose not have focusing capabilities. Instead the spacecraft acquires a single spectrum of everything in the 1° Full Width Half Maximum (FWHM) field of view. The source density is very low at these energies and sensitivities, however, and so source contamination other than the X-ray background is rarely a problem.

Figure 3.1 shows a schematic view of *RXTE* satellite in orbit. As shown in Figure 3.1, *RXTE* carries three scientific instruments: Two of them, for pointing observation, are the Proportional Counter Array (PCA) developed by NASA's Goddard Space Flight Center (GSFC) and the High Energy X-ray Timing Experiment (HEXTE) developed by University of California at San Diego (UCSD). PCA covers the lower part of the energy range (2−60 keV), while the HEXTE covers a higher energy range, from 20 keV to more than 100 keV. These instruments are equipped with collimators yielding an angular resolution of 1 degree. The remaining one instrument is for monitoring observation, an All-Sky monitor (ASM) from Massachusetts Institute of Technology (MIT), that scans about 80 % of the sky on every orbit. ASM allows constant monitoring of the sky at time scales of 90 min or longer.

The instruments on board *RXTE* were designed to observe the temporal properties of strong X-ray sources, with moderate spectral energy resolution with wide energy band over ∼2 decades. Simply having μs time resolution is not adequate, however, since large numbers of photons need to be collected to give adequate signal to noise in these thin time bins. Therefore the goal of high time resolution studies, especially below 1 ms, requires large areas with a high throughput as well.

To achieve this high degree of timing accuracy, the *RXTE* mission operation center performs 10 calibration observations for the spacecraft clock per day. The calibration relies on a round trip signal, tagged by the spacecraft clock's time stamp of no more than 1 μs. The dominant uncertainty in this calibration is the clock at the ground station in White Sands, New Mexico, which is typically only kept within 2−5 μs of UTC. Still, the *RXTE* time stamps can be corrected to within 5 μs of absolute time (Rots et al. 1998). This accuracy of the time stamp is quite enough for my study presented later.

In addition to the timing properties of *RXTE*, *RXTE* also have wide spectral energy band from ∼2–250 keV. This wide energy band also enables us to detect the cyclotron resonance scattering features in Cen X-3.

3.2 PCA

3.2.1 System Description

The Proportional Counter Array (PCA, see Figure 3.2) on board the *RXTE* consists of five large proportional counter units (PCUs) sensitive in the range 2–60 keV with anti-coincidence (hereafter "veto") features which provide a very low background. A mechanical hexagonal collimator is carried on each proportional counter, which provides an angular resolution of

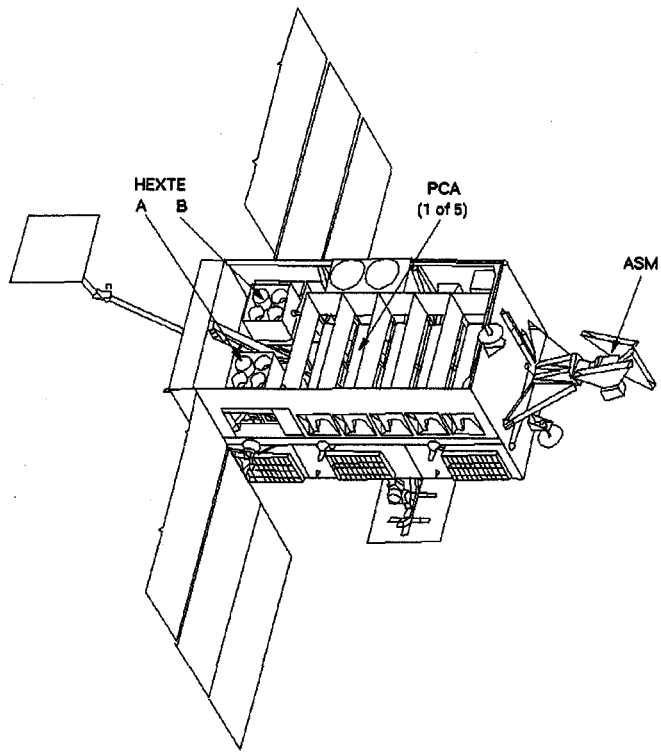

Figure 3.1: Schematic drawing of the *RXTE* satellite. Three kinds of instruments, PCA, HEXTE and ASM are carried on the spacecraft.

1 degree (FWHM). Because of the large effective area, sources as faint as 1 mCrab can be detected only in a few seconds. The detailed description on the PCA design, as well as the orbit performances are given in Jahoda et al. (1996; 1999).

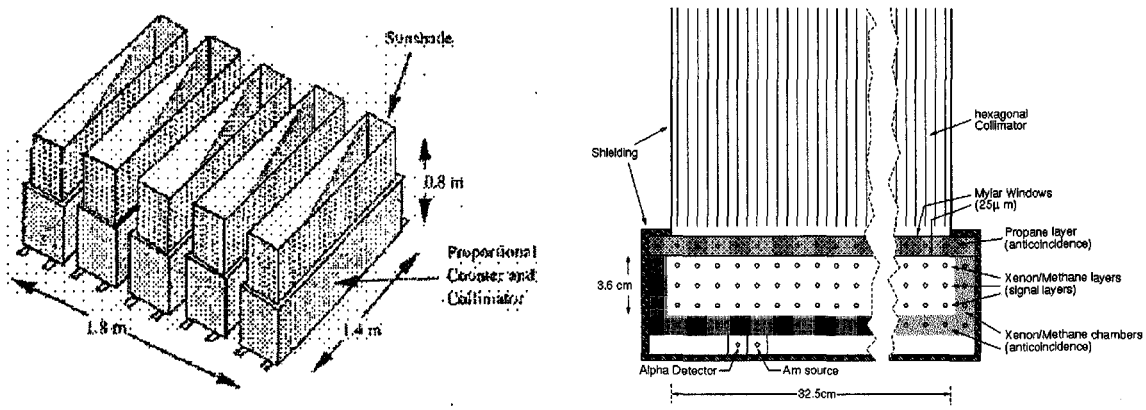

Figure 3.2: *left* : Assembly of 5 PCA counter units onboard the *RXTE*. *right* : The cross section diagram of a PCA. A charge pulse event is classifies as a valid X-ray photons event ("good event") if none of the anti-coincidence anodes, located at the sides and bottom of the chamber, or the propane layer, are simultaneously triggered.

The total area of 5 PCUs is 6250 cm^2. The schematic view of an assembly of five units and each proportional counter are given in Figure 3.2.

Each PCU is collimated to a 1° field of view by a hexagonal collimator of BeCu. Behind the collimator are two mylar windows, each 1 mil thick and coated on both sides with a thin layer of aluminum. These windows are separated by 1.3 cm and contain a layer of propane used to screen out low-energy electrons ($E_e < \sim 2$ keV). Behind the second mylar window is the main detector volume, filled to about 1 atom with a gas mixture of 90% Xenon and 10% Methane. Inside the Xenon/Methane chamber, there are three layers of signal anodes which collect the charge deposited by incident X-rays, follows by a single anticoincidence anode layer at the bottom of the chamber. Side anode provide further anticoincidence, and the detectors are passively shielded (Ti and Zn) to provide additional background reduction. The nominal energy resolution of the 18 % at 6 keV, and achieve low background through efficient veto schemes including side and rear chambers and a propane top layer. We summarize the design parameters and performance of PCA in Table 3.1. Figure 3.3 shows the effective area of the PCA as a function of energy with all 5 PCUs operating. Gain control and calibration are done using a tagged ^{241}Am source in each of the PCUs.

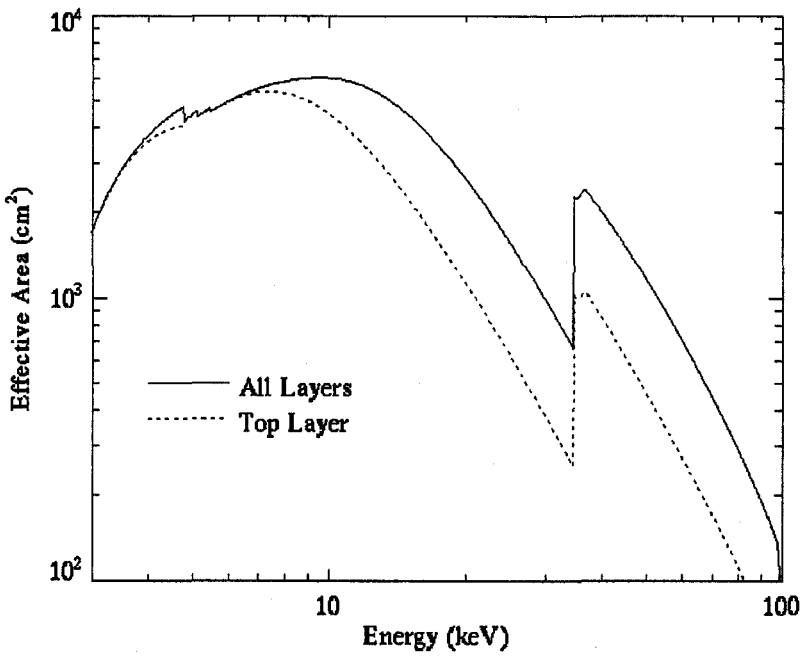

Figure 3.3: The effective area of the PCA as a function of energy with all 5 PCUs operating onboard the *RXTE* satellite. The dotted line is the effective area for the top layer only. Although the area of the top layer alone is less when compared to all layers, the instrumental calibration is superior, resulting in a reduction of the systematic uncertainties in PCA spectra. The absorption L-edges and K-edges of Xenon is clearly seen around 5 keV and 34.6 keV, respectively. (Jahoda et al. 1996)

Table 3.1: Design parameters and performance of *RXTE* PCA

Energy Band	$2 - 60$ keV
Energy Resolution	$\leq 18\%$ at 6 keV (FWHM)
Time Resolution	1 μs
Angular Resolution	1 degree (FWHM)
Detectors	5 proportional counters
Collecting Area	6500 cm^2
Net Area	3000 cm^2 (at 3 keV) and 6000 cm^2 (at 10 keV)
Layers	1 Propane veto, 3 Xe, 1 Xenon veto layer
Sensitivity	0.1 mCrab ($2 - 10$ keV in min)
Background	2 mCrab
Telemetry	18 kb/s

3.2.2 On-Board Data Processing

Due to the large area of instrument the count rates can be large enough to saturate the telemetry capability of the *RXTE* satellite. The processing count rates from the PCA will be up to 5×10^5 cts/s (only 6 % dead time for the Crab) and will be able to determine photon arrival time with an accuracy of ~ 1 μs. In these cases the raw data has to be compressed, selecting only the information desired by the observer. This is the task of the Experiment Data System (EDS). The EDS consists of 8 parallel, independent computers known as Event Analyzers (EAs). Six of them are dedicated to the PCA, while the remaining 2 process data from ASM.

Two of the 6 PCA EAs are intended to be reserved for "standard mode" data with timing and spectral parameters that will remain unchanged throughout the mission to provide a uniform mission data bank. For the remaining 4 PCA EAs, however, processing modes are flexibly selected by guest observers to accommodate the scientific requirements.

Standard Mode

The standard observation mode consists of *Standard*-1 and *Standard*-2. The PCA *Standard*-1 data has a temporal resolution of 0.125 s without any spectral information. The PCA *Standard*-2 data has a temporal resolution of 16 s, with 129 pulse height analyzer (PHA) channels for each layer of each PCU. The *Standard*-2 data is the basis of most of the phase average spectral analysis presented in this thesis. The 16 s time resolution is, however, in-

adequate for timing analysis for our study. So, for timing analysis in this thesis, the data obtained by specific observation modes are used (see section 3.5 in this chapter).

The Other Specific Observation Mode

For the PCA, each EA can process a different "observation mode", or a prescription for compressing the data based upon time and energy resolution. The available PCA data modes span nearly continuously the phase space between temporal and spectral resolution. It is up to the observer to choose which combination of maximum telemetry rate are allowed. There are two main classes of observation modes. The first set is the "event mode", where each photon collection is registered as an event. For example, the event mode designated as "`E_31us_16M_36_1s`" has events tagged with 31 μs time resolution, the full energy range has been compressed from the original 256 channels into 16 channels using the "M" rebinning scheme and starting at channel 36, and events are read out every second.

As counting rates increase, the ability to preserve each photon individually is lost. For these sources, including Cen X-3, the "binned mode" is available, where histograms instead of events are telemetered to the ground. This is designated in a fashion similar to the "event mode" data. For example, the binned mode "`B_16ms_16A_0_35_H`" produces a histogram every 16 ms with 16 spectral channels rebinned from the original channels 0–35 using the "A" scheme. The final "H" denotes how many bits each histogram contain.

If the source counting rate is low enough, then there is no need for any onboard data compression. For these sources, the "`GoodXenon`" data mode is available, which preserves all information, such as spectral information of 256 channel, and so on.

3.2.3 Reduction of PCA Data

Energy Response

As we have seen in Figure 3.2, each PCU detector, from the top, consists of a thermal shield, a collimator, an aluminized mylar window, a propane volumes, and a detector body. The low energy threshold of the PCA is determined by the transmission of the aluminized mylar window (1 mil each) and the propane volume. For generating the response matrix, the important quantity is the photo-electric stopping power of each layer and all exterior layers.

The gain of the counter is monitored continuously with an ^{241}Am radioactive source for which detection of the α particle identifies the calibration X-rays.

PCA response matrices map 900 energies from 0.023 to 100 keV to 256 PHA channels. Half of the energy channels are equally spaced below 10 keV, except that the three channels

which include one of the Xe-L edges are split into two channels with channel boundary matching the atomic edge. The remaining channels are also equally divided except that the channel including the Xe-K edge is again split into two channels.

Background

The detector background mainly consists of two components. The first is internal to the instrument, caused by interactions of cosmic rays and their secondaries with the detector material and by short-term radioactivity produced during passages through the SAA. The second is a contamination of the source spectrum due to the diffuse cosmic X-ray background whose radiation is thought to be produced by the superposition of many weak active galactic nuclei. For the PCA, these background components cannot be observed directly, and therefore have to be modeled.

To model the background, it is assumed that the internal background varies on a time scale which is longer than the natural time scale of the PCA *Standard*-2 data (16 s). The design is such that the model can be evaluated once every 16 s, and that the equivalent of the *Standard*-2 data file can be created with separate information for each detector and each anode chain.

The modeled background spectrum can be based on parameters measured at the time of the observation. These parameters describes the condition and position of the spacecraft as well as the evolution of the spacecraft. PCA background models based on these parameters have been constructed in two ways: using the data from blank-sky observations and using the data from periods of Earth occultation. The models based on the local particle parameters are constructed using the data from only those spacecraft orbits in which the SAA-induced activation is small. Some of these data are still significantly contaminated by SAA-induced activation but this contamination can be later removed by an appropriately constructed model of the activation component of the background.

Electron Contamination

The background models are parameterized in terms of the particle rate. In addition to the high energy protons and ions, low energy electrons may also lose their energy within the detector. Electrons with several tens of keV may come through the collimator and stop in the first Xe layer. The rate of propane plus first layer coincidences measures such a population. These events are vetoed, and the rate can be used to screen periods when there could be increased background, for instance due to the same electrons fluorescing the collimator. For

the reliable data reduction, we have screened the data when the electron rate is significantly high.

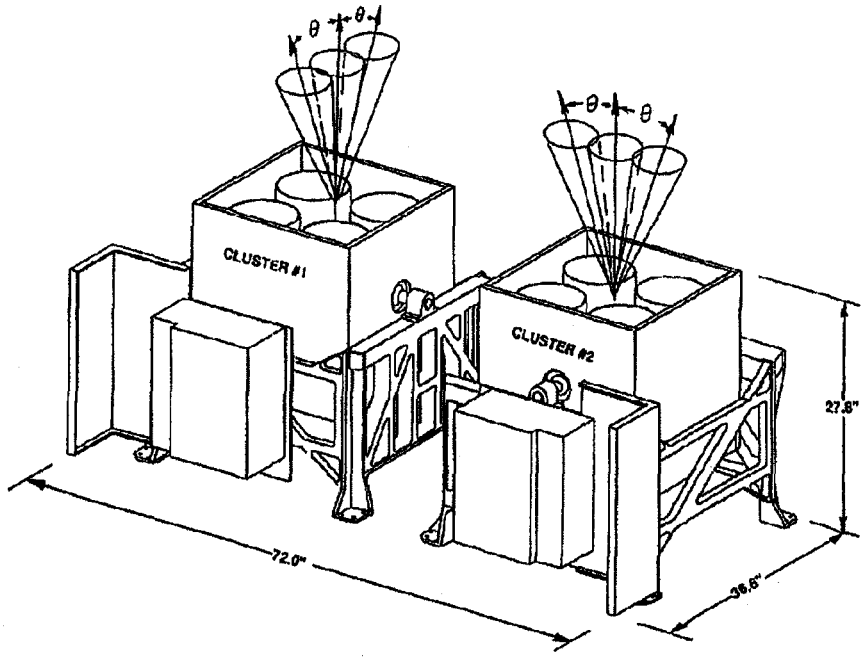

Figure 3.4: Schematic view of two HEXTE clusters onboard the *RXTE*.

3.3 HEXTE

The High Energy X-ray Timing Experiment (HEXTE) instrument on the *RXTE* was designed and built at UC San Diego. The HEXTE consists of two assemblies for four NaI(Tl)/CsI(Na) phoswich scintillation counters, named clusters "A" and "B", respectively. Figure 3.4 shows the schematic view of HEXTEs. Rothschild et al. (1998) describes HEXTE instrument in details.

The HEXTE is collimated to 1° FWHM using a lead honeycomb and is coaliged to the same pointing field of view as the PCA. The nominal area of each cluster is 800 cm^2, and the HEXTE has a maximum time resolution of 8 μs and a energy resolution is 16% at 60 keV. As shown in Figure 3.4, eight "Phoswich (NaI+CsI)" detectors are arranged in two clusters, each of which rocks on and off the source.

Gain control and calibration in the HEXTE is done using ^{241}Am mounted into the collimator of each phoswich (see Figure 3.5). Compared with the PCA, the HEXTE has far fewer data modes available. But, due to the smaller area of the instrument, coupled with the fact that most sources have a lower luminosity in the HEXTE energy range, there is less of a requirement on the telemetry.

On 1996 March 21, one of the pulse height analyzers in cluster B failed, effectively

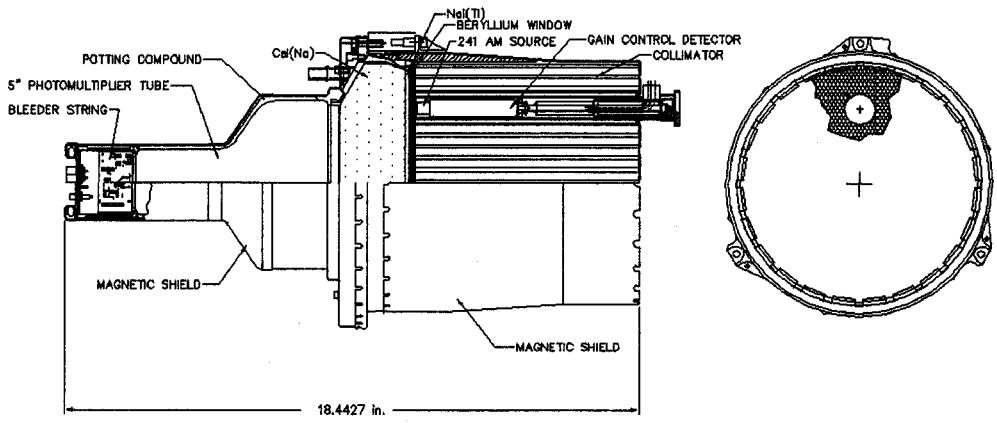

Figure 3.5: Cutaway schematic view of a HEXTE phoswich detector unit.

reducing the area of that cluster by 25%. The current effective area of each clusters is shown in Figure 3.6. We summarize the design parameters and performance of HEXTE in Table 3.2.

Table 3.2: Design parameters and performance of *RXTE* HEXTE

Energy Band	20 – 200 keV
Energy Resolution	$\leq$ 18% at 60 keV (FWHM)
Time Resolution	10 μs
Angular Resolution	1 degree (FWHM)
Detectors	2 clusters of NaI(Tl) and CsI(Na) phoswich units (4)
Collecting Area	1600 cm^2
Net Area	1200 cm^2 (at 50 keV) and 300 cm^2 (at 200 keV)
Sensitivity	1 mCrab (90 – 110 keV; 3 σ for 10^5 s pointing)
Background	100 mCrab
Telemetry	5 kb/s

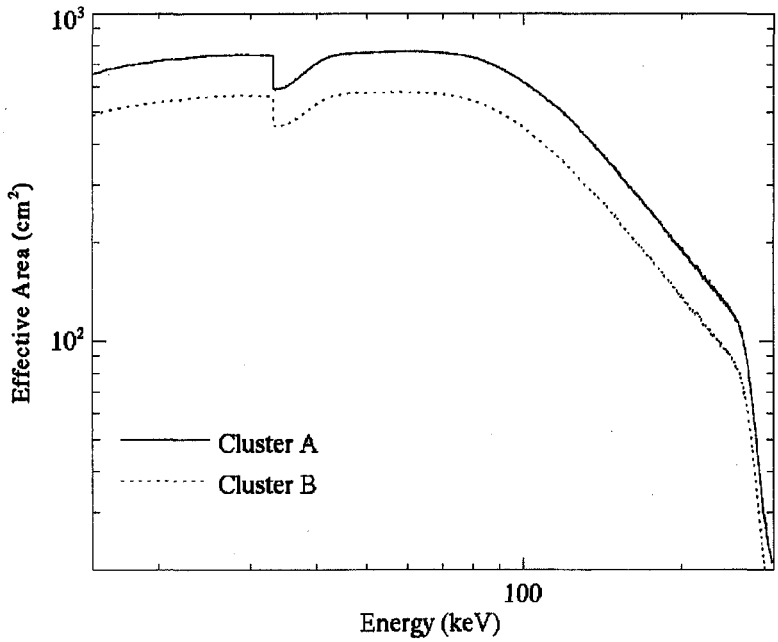

Figure 3.6: The effective area of the two HEXTE clusters. Cluster B has a slightly lower effective area due to the loss of a phoswich early in the mission. The reduction of lower energies is due to the housing of the detector, while higher is due to the finite thickness of the detector. Around ~33 keV, Iodine K-edge is clearly seen.

3.4 ASM

The third instrument onboard the *RXTE* is the All Sky Monitor (ASM), built by the Center for Space Research at MIT. The ASM was designed to monitor the fluxes of many discrete sources simultaneously (Levine et al. 1996). ASM also has been vital in identifying and monitoring outbursts from transient sources.

ASM consists of three rotating Scanning Shadow Cameras (SSCs) that can scan about 80 % of the sky in 90 min in the energy range of 1.5–13 keV. The field of view of each SSC is collimated to a 6°×90° FWHM, the detector has a spatial resolution of $3'\times15'$. The shadow mask on each of the SSCs is a thin aluminum sheet divided into 6×2 subsections. Each of the 12 subsections contains ~15 open and ~16 closed slit elements arranged in 1 of 6 carefully chosen pseudo-random patterns. The SSC detectors contains a Position Sensitive Proportional Counter (PSPC) with an effective area of ~30 cm^2. The PSPC is used to measure the displacements and strengths of the shadow patterns cast by X-ray sources within the field of view, and thereby allowing source intensities and directions to be measured.

The camera provides measurements of intensities of about 75 known celestial sources in a day and can measure the position of a previously unknown source with a precision of about 3'.

3.4.1 System Description

Figure 3.7 the shows schematic view of the assembly of shadow cameras and their scan directions. The design parameters and performance of ASM are summarized in Table 3.3.

Each SSC is a one-dimensional "Dicke camera" consisting of a 1-dimensional mask and a 1-dimensional PSPC (Figure 3.7). Because of the mask ('slit') above the PSPC, the X-rays coming from different directions should make different images on anodes, which is the principle of the Shadow Camera. The gross field of view of a single SSC is 6° × 90° FWHM, and the angular resolution in the narrow (imaging) direction is 0.2 degree.

A motorized drive rotates the three SSCs from field to field in 6° steps. At each resting position, a ~ 100 s exposure of the X-ray sky is made; a complete rotation, thus, spends 90 min. Since the 'crossed-field detectors' are stepped by only the 6° FWHM angle, each source is viewed twice. In this manner, each source gives rise to the entire mask pattern in the accumulated data, thus minimizing aliasing and side bands in the deconvolved results. During each rotation, ~ 80 % of the sky is surveyed to a depth of ~ 20 mCrab (about 50 sources). Frequent spacecraft maneuvers make it likely that 100 % of the sky is surveyed

each day. In one day, the limiting sensitivity becomes $\leq$ 10 mCrab ($\sim$ 75 sources).

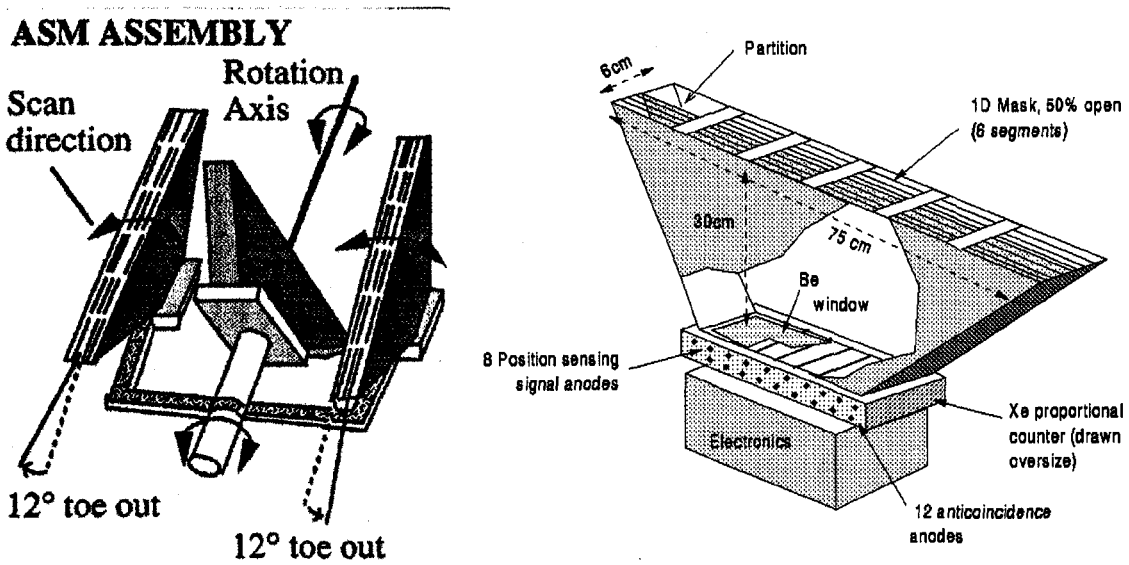

Figure 3.7: *Left* : All-Sky Monitor assembly of 3 Shadow Cameras. ASM scans 80 % of the sky every 90 min to monitor the intensity of the brightest 75 X-ray sources and to provide an alert if a source changes state or brightness suddenly. This allows the spacecraft to be maneuvered to observe with more powerful PCA/HEXTE systems. *Right* : Shadow Camera (1 of 3) of All Sky Monitor. Each SSC is a sealed proportional counter filled to 1.2 atm with Xe-CO_2, and sensitive depth of 13 mm.

Table 3.3: Design parameters and performance of *RXTE* ASM

Energy Band	2 – 10 keV
Energy Resolution	$\sim$20% in 2 – 10 keV (3 energy channels)
Scan Time	90 min: 80 % of the sky per orbit
Angular Resolution	0.2 degree
Positional Resolution	3' $\times$ 15'
Detectors	3 Scanning Shadow Cameras
Collecting Area	180 cm^2 (without masks)
Net Area	90 cm^2 (3 detectors)
Sensitivity	20 mCrab in 90min; $\leq$ 10 mCrab in a day
Telemetry	3 kb/s

3.4.2 Reduction of ASM Data

The position histograms are analyzed in near-real time in the Science Operations Facility at GSFC. The data is first fit with the model responses of each SSC to the cataloged bright X-ray sources within the field of view. A linear least squares calculation yields the strengths of each of these sources. Next, the fit residuals are examined via a cross-correlation technique for evidence of previously unknown or unexpectedly bright sources. When a new source is found, its coordinates are entered into the source catalogue. For quick-look analysis, the data will be performed on a dwell-by-dwell and SSC-by-SSC basis. For the definitive analysis, the analysis will be performed simultaneously on data from neighboring dwells and from multiple cameras. The resultant ASM light curves are open to public and one can obtain the data via online service for 75 sources (http://space.mit.edu/XTE/asmlc/ASM.html).

3.5 Observation of Cen X-3

RXTE has observed Cen X-3 twelve times with various observation modes of PCA. For this work, four of twelve data are available with both the adequate time resolution and reasonable energy resolution. In Table 3.4, we summarize the observation mode of PCA of the four observations.

Table 3.4: Summary of PCA observation of Cen X-3

Observation ID	Date	PCA data mode
P10134	1996 September 10–27	`B_16ms_64M_0_249`
P20104	1997 February 28 – March 3	`B_16ms_16A_0_35_H`
P30084	1998 June 26 – July 5	`B_4ms_16A_0_35_H`
	1998 October 1 – 10	`B_4ms_16B_0_249_Q`
P40072	2000 February 2–4	`GoodXenon`

Chapter 4

Orbital Period and Orbital Phase of Cen X-3

In this chapter, we will present a new eclipse center epoch for Cen X-3 based on pulse-timing analysis obtained with *RXTE* from 1997 February 28 to 1997 March 3 (Observation ID = 20104).

4.1 Introduction

The long term decrease of 4.8 s pulse period of Cen X-3 has provided a support for the accretion torque model for pulse period changes as seen in many X-ray pulsars (see Bildsten et al. 1997 for review). In addition, Cen X-3 is the only massive X-ray binary for which a finite rate of change of the orbital period has been obtained.

Kelley et al. (1983) obtained a negative rate of orbital period change, $\dot{P}_{orb}/P_{orb} = -(1.78\pm0.08)\times10^{-6}$ yr^{-1}, using a set of eclipse epoch data observed between 1971 and 1981 with X-ray satellites from *Uhuru* to *SAS-3*. They suggested this orbital decay was mainly due to the result of tidal torque between the distorted companion star and the neutron star. Nagase et al. (1992) reported $\dot{P}_{orb}/P_{orb} = -(1.738\pm0.004)\times10^{-6}$ yr^{-1} by adding three more set of eclipse epoch data obtained with *Hakucho*, *Tennma*, and *Ginga* to the data of Kelley et al. (1983). Table 4.3 shows the available eclipse center epoch and the corresponding uncertainties of Cen X-3 including this work.

Since the present observation with *RXTE* in 1997 has significantly extended the observation baseline, we have re-examined the change of the orbital period by combining the eclipse center epoch obtained with previous derived epochs (see Kelley et al. 1983; Nagase et al. 1992). In addition to our new result, we included the other new two intermediate

epochs obtained with *Ginga* and *ASCA* as well. Their epochs were JD 2,446,969.70±0.02 (Tsunemi et al. 1989) and JD 2,449,163.230±0.020 (Ebisawa et al. 1996), respectively. Our result shows that the $2^d.1$ binary period is decreasing with an average rate of $\dot{P}_{orb}/P_{orb}$ = – (1.77±0.04)×10^{-6} yr^{-1} including all published eclipse time based on Doppler delay measurements.

In this chapter, we will present a new precise mid-eclipse time measurement with *RXTE*, and will also present the interpretation of the decrease of the orbital period according to the discussion by Kelley et al. (1983), using our new result.

4.2 *RXTE* Observation and Result

RXTE has carried out observations of Cen X-3 on twelve occasions since 1996 (as of 2002 Jan). As shown in Figure 4.1, only one observation (Observation ID=P20104) among twelve observations observed whole two orbital cycles of Cen X-3.

Instead of `Standard-2` mode with only 16 s time resolution, for the pulse period analysis we used the data obtained with the binned mode (`B_16ms_16A_0_35_H`) whose time resolution was 16 ms and energy band was 2–13 keV. The data reduction method of *RXTE* will be described in the next chapter.

We first filtered the event files for all layers of all PCUs, then we accumulated those files using a similar procedure as for `Standard-2` mode (see next chapter). When we extracted the light curve from the event file, we used all events between 2–13 keV, and made the barycentric correction to the light curve using the ftools **fxbary**. Next, using ftools **efsearch**, we calculated the pulse period from the extracted light curve. We obtained total of 55 pulse periods through this observation (the calculated 55 pulse periods are plotted in Figure 4.2).

Figure 4.2 shows the Doppler delays of pulse period due to a circular orbit of Cen X-3. By applying a simple sinusoidal model to this data, we derived the projected semimajor axis of the X-ray star orbiting with an inclination angle i, $a_x \sin i$, a spin period, P_{spin}, an orbital period, P_{orb}, and a time of mid-eclipse T_e, respectively. In this analysis, we assumed a circular orbit since the eccentricity, e = 0.0004±0.0002 (Kelly et al. 1983), was too small to affect the present analysis. In addition, we assumed the pulse period was constant during this observation as well. These best fit parameters are summarized in Table 4.1.

Our derived spin period was smaller by ∼8 ms than that obtained with *Ginga* (Nagase et al. 1992), demonstrating that the source was still in a spin up state (see also Figure 2.12 in chapter 2).

To study orbital period changes of Cen X-3, we have used all available mid-eclipse times

(see Table 4.3). Assuming a constant rate of change of the orbital period, the time of the Nth mid-eclipse can be fitted with:

$$T_N = T_0 + P_{orb}N + \frac{1}{2}P_{orb}\dot{P}_{orb}N^2, \tag{4.1}$$

where P_{orb} and $\dot{P}_{orb}$ are the orbital period and its derivative at time T_0, respectively. The delays of the eclipse time from a linear ephemeris, together with residuals of delays from the best fit quadratic ephemeris, are shown in Figure 4.3. When carrying out this χ^2 fits to a series of data points obtained in previous observations, the total χ^2/D.O.F of our result was 630.56/27. This result was statistically unacceptable. Then, in order not to underestimate the uncertainties of each parameter, we fitted these data series again after scaling up the error bars on the individual measurements until χ^2 per degree of freedom equaled unity.

Similar to the Nagase et al. (1992), except for the first few data sets obtained with *Uhuru* satellite as shown in Figure 4.3, all the above mentioned data were reasonably fitted with the quadratic ephemeris, given

$$\dot{P}_{orb}/P_{orb} = -(1.77 \pm 0.04) \times 10^{-6} yr^{-1}. \tag{4.2}$$

The calculated uncertainties of each parameter, including $\dot{P}_{orb}/P_{orb}$, were larger by about an order than that of Nagase et al. (1992), even if we used more data series by three than Nagase et al. (1992). This was because Nagase et al. (1992) underestimated these uncertainties.

Comparing to the result of Kelly et al. (1983), our derived value of $\dot{P}_{orb}/P_{orb}$ is consistent within one σ error of their result, and more precise by a factor of two. In addition, $\dot{P}_{orb}/P_{orb}$ derived by Nagase et al. (1992) is within one σ error of our result.

This result suggests that the rate of changes of orbital period has been stable for 23 yrs period since the *Uhuru* observations. The orbital period ephemeris by our best fit values is summarized in Table ??.

Table 4.1: Circular orbit fits to the Cen X-3 observed with *RXTE*.

Parameter	Value
$a_x \sin i$	39.81±0.06 (lt-s)
P_{spin}	4.814249±0.000009 (s)
P_{orb}	2.088±0.001 (d)
T_e	2,450509.3745±0.0009 (JD)

Table 4.2: Long-Term Orbital Period Behavior of Centaurus X-3.
Time of the Nth mid-eclipse and orbital period.
$T_n = T_0 + P_{orb}N + 1/2\ P_{orb}\ \dot{P}_{orb}N^2$

Parameter	Value
T_0	2440958.85082± 0.00002 (JD)
P_{orb}	2.0871390±0.0000003 (d)
$1/2\ P_{orb}\ \dot{P}_{orb}$	$-(1.06\pm0.02)\times10^{-8}$ (d)
$\dot{P}_{orb}$	$-(1.01\pm0.02)\times10^{-8}$
$\dot{P}_{orb}/P_{orb}$	$-(1.77\pm0.04)\times10^{-6}$ yr^{-1}

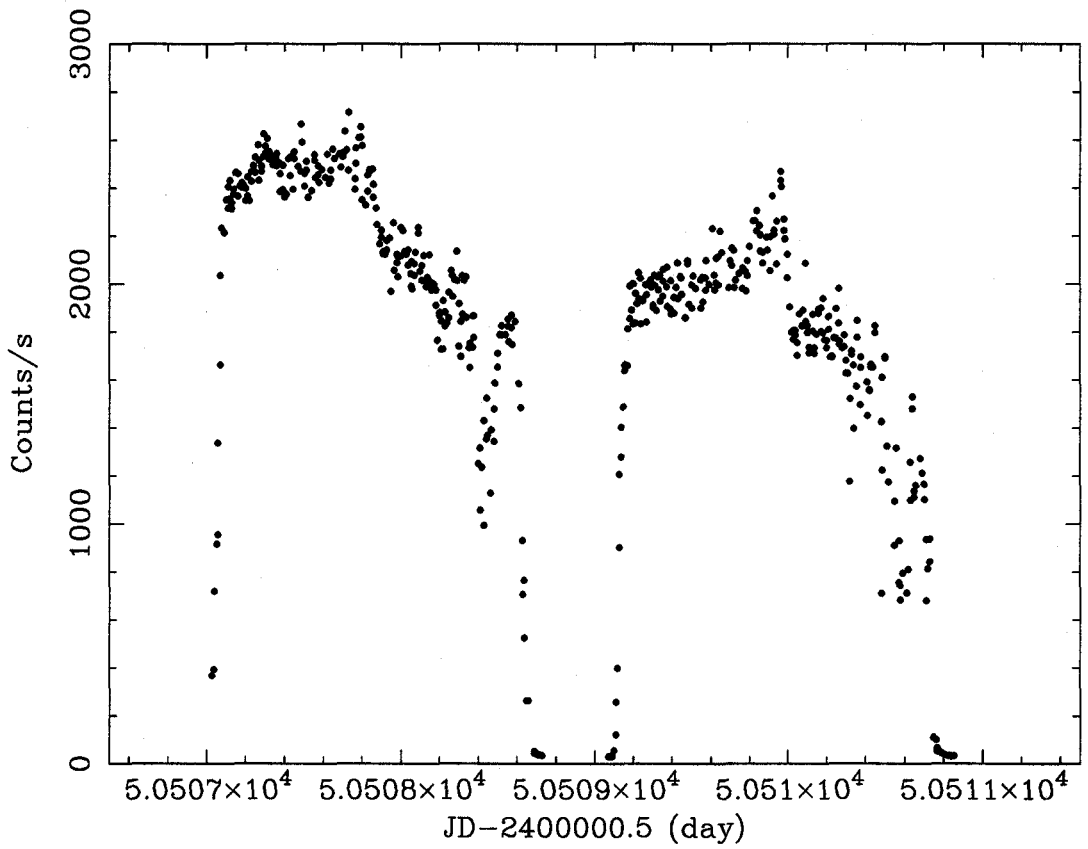

Figure 4.1: The background subtracted light curve of the entire observation in 2–50 keV with 512 s bin observed with *RXTE* PCA *Standard*-2 mode from 1997 Feb 28 to 1997 March 3. Almost two orbital cycles were observed. Eclipses and pre-eclipsing dips are clearly seen.

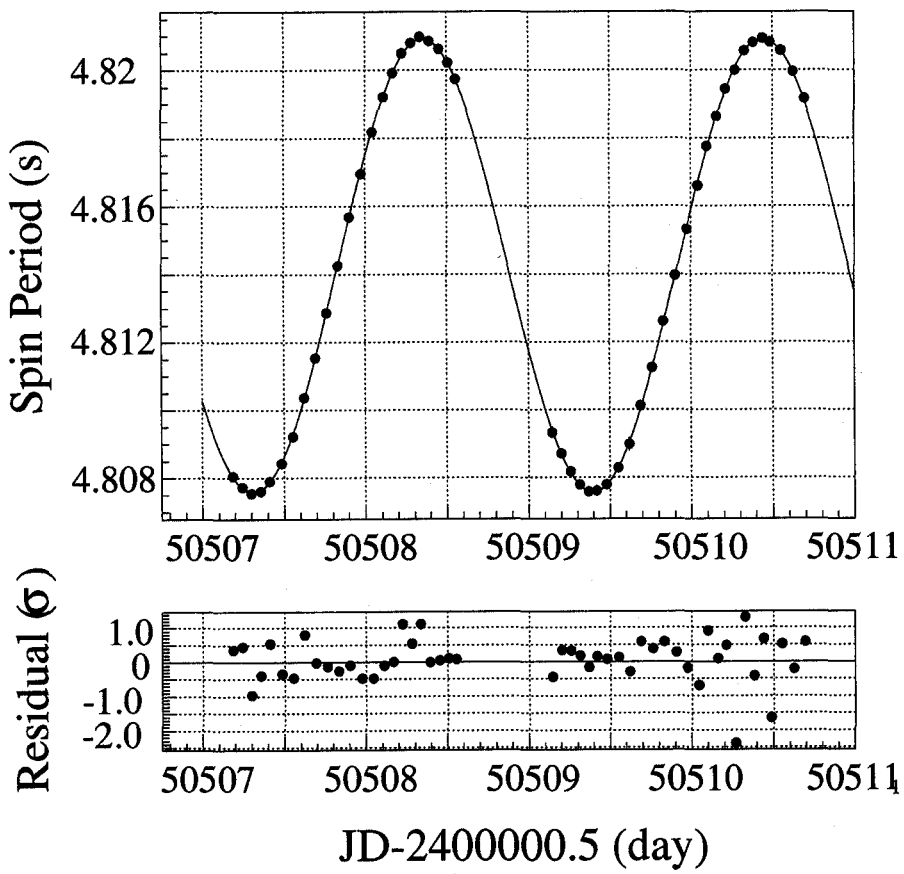

Figure 4.2: Doppler curve of pulsation period and the best fit orbit model Cen X-3.

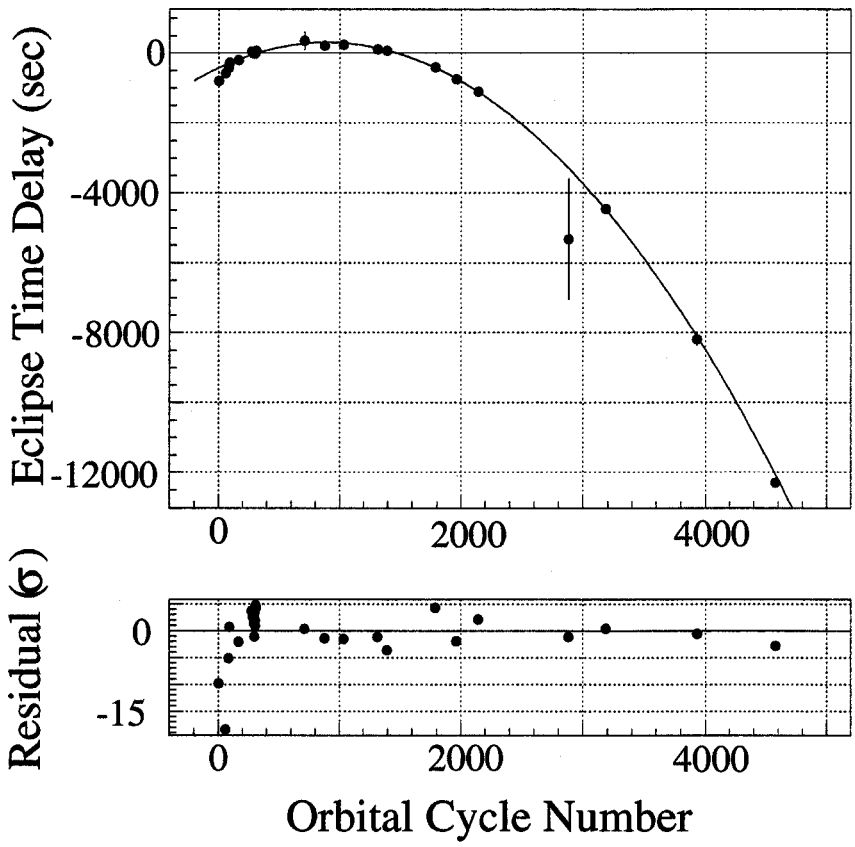

Figure 4.3: Delays of mid-eclipse time of Cen X-3. Upper panel shows that the observed-minus-calculated eclipse times (filled squares) with respect to a linear ephemeris. The eclipse times and references are given in Table 4.3. Lower panel shows the residual of the observed eclipse times from the best fitting quadratic ephemeris.

Table 4.3: Cen X-3 Eclipse Times

Orbital Cycle	Time JD – 2440,000.0	Reference
0	958.84643±0.00045	Fabbiano & Schreier 1977
57	1077.81497± 0.00015	Fabbiano & Schreier 1977
83	1132.08181±0.00029	Fabbiano & Schreier 1977
91	1148.78051±0.00016	Fabbiano & Schreier 1977
166	1305.31533±0.00014	Fabbiano & Schreier 1977
273	1528.64010±0.00030	Fabbiano & Schreier 1977
284	1551.59789±0.00017	Fabbiano & Schreier 1977
293	1570.38199±0.00011	Fabbiano & Schreier 1977
295	1574.55610±0.00013	Fabbiano & Schreier 1977
296	1576.64330±0.00010	Fabbiano & Schreier 1977
297	1578.73037±0.00007	Fabbiano & Schreier 1977
298	1580.81722±0.00009	Fabbiano & Schreier 1977
300	1584.99193±0.00010	Fabbiano & Schreier 1977
303	1591.25328±0.00015	Fabbiano & Schreier 1977
304	1593.34025±0.00015	Fabbiano & Schreier 1977
307	1599.60212±0.00015	Fabbiano & Schreier 1977
308	1601.68930±0.00014	Fabbiano & Schreier 1977
309	1603.77671±0.00021	Fabbiano & Schreier 1977
709	2438.628±0.003	Tuohy 1976
876	2787.1755±0.0007	van der Klis, Bonnet-Bidaud, & Robba 1980
1032	3112.76642±0.0004	Kelley et al. 1983
1314	3701.33275±0.00043	Howe at al. 1983
1395	3870.38910±0.00002	Kelley et al. 1983
1786	4686.44760±0.00005	Murakami et al. 1983
1960	5049.6025±0.0001	Nagase et al. 1984
2142	5429.45421±0.00005	Nagase et al. 1984
2880	6969.70±0.02	Tsunemi et al. 1989
3186	7608.3688±0.0008	Nagase et al. 1992
3931	9163.230±0.002	Ebisawa et al. 1996
4576	10509.3745±0.0009	This work

4.3 Interpretation of the Orbital Decay in Cen X-3

In this section, we will interprete of the decrease of the orbital period in Cen X-3 according to the discussion by Kelley et al. (1983), using our new result.

In general, the rate of change of the orbital period of a binary system is determined primarily by considerations of angular momentum. In particular, there are two principal ways in which the orbital period may change, and it will be caused

1. by mass exchange and/or the mass loss taken by a critical potential lobe overflow or by a stellar wind,

   or

2. by the tidal interaction.

If the mass loss occurs in binary system, it is likely to carry away angular momentum. Or, one or both members of a binary system will be tidally distorted, and, through viscous forces, the tides raised on one star will lag (or lead) the other orbiting component as long as the stellar rotation is not synchronous with the orbit. Then, a torque is exerted which trends to decrease (or increase) the orbital angular momentum.

In the binary system of Cen X-3, the orbital period decreasing over 23 yr probably ultimately has also produced by tidal coupling of Krezeminski's star (V779 Cen) to the orbiting neutron star.

The orbital angular momenta of companion star, l_c, and the compact star, l_x, are related by $l_x = l_c\ (M_c/M_x)$, here M_c, and M_x is the mass of the companion star and the compact star, respectively. If mass transfer and mass loss occur, the rate of change of l_x, and hence the effective torque on the orbiting compact star, is given:

$$\dot{l}_x = l_c \frac{\dot{M}_c}{M_c}\left(\frac{1+\beta/q}{1+q}\right) + \dot{l}_T\left(\frac{1}{1+q}\right). \tag{4.3}$$

Here $l_T\ (= l_x + l_c)$ is the total orbital angular momentum, $q = M_x/M_c$, and β is the fraction of mass lost by M_c that is captured by M_x ($\beta = -\dot{M}_x/\dot{M}_c$).

In general, the mass transfer process is not conservative in both total mass and angular momentum, then the rate at which angular momentum is lost from the system is parameterized as follows,

$$\dot{l}_T = \xi \dot{M}_T a_c^2 \omega_K = \xi \dot{M}_c (1-\beta) a_c^2 \omega_K. \tag{4.4}$$

Here ξ is a dimensionless parameter that is to be specified or determined, M_T is the total mass of the binary system, a_c is the semimajor axis of the orbit of the companion star, and ω_K is the orbital angular velocity. Here, Kelley et al. (1983) define a torque on the compact star due to the mass loss and the mass exchange by $N_x^{\dot{m}} \equiv \dot{l}_x$. Then, the equation (4.3) can be rewritten as follows;

$$N_x^{\dot{m}} = \dot{M}_c a_c^2 \omega_K \frac{[1+\beta/q+\xi(1-\beta)]q^2}{(1+q)^3}. \tag{4.5}$$

To account explicitly for the tidal interaction, a simple one parameter expression for the tidal torque on the orbiting neutron star due to a tidal lag has been adopted (Kelley et al. 1983):

$$N_x^t = -I_c \frac{(\omega_K - \omega_C)}{\tau}, \tag{4.6}$$

where I_c is the moment of inertia of the companion star, ω_C is its angular frequency, and τ is a synchronization time scale (which, for radiatively damped dynamical tides (Zahn et al. 1977), is itself a function of (ω_K - ω_C)).

The dynamical equations governing the evolution of the system are given by

$$\frac{dJ_c}{dt} = N_c^t + N_c^{\dot{m}}, \tag{4.7}$$

and

$$\frac{dJ_x}{dt} = N_x^t + N_x^{\dot{m}}, \tag{4.8}$$

where J_c and J_x are the total angular momenta of the companion star and the compact star, and N_c^t and $N_c^{\dot{m}}$ are the mass loss and tidal torques on the companion star, respectively. The spin angular momentum of the compact star (neutron star) of Cen X-3 is much smaller than the orbital angular momentum and, thus, can be neglected in equation (4.8) (i.e., $J_x \simeq l_x$). As results from above equations in addition to the Kepler's third law, $a^3\omega_K^2 = GM_T$:

$$\frac{\dot{P}_{orb}}{P_{orb}} = 3f\frac{\dot{M}_c}{M_c} - 3g\frac{\omega_K - \omega_C}{\omega_K}\frac{1}{\tau}, \tag{4.9}$$

where

$$f = \frac{\beta}{q} - \frac{\frac{2}{3}+\frac{\beta}{3}+q[1-\xi(1-\beta)]}{1+q}, \tag{4.10}$$

and

$$g = \eta \frac{(1+q)^2 (\frac{R_c}{a})^2}{q}. \tag{4.11}$$

Here the quantity η is the moment of inertia of the companion star in units of $M_c R_c^2$.

To investigate the implications of above equations (4.9) – (4.11), the next two limiting case are considered:

1. the synchronization time scale is much longer than the time scale for orbital decay ($P_{orb}/\dot{P}_{orb} \simeq 5\times10^5$ yr), and the orbital period changes are, therefore, entirely due to the effect of both the mass loss and the mass exchange, and

2. tidal effects dominate the orbital dynamics.

The relation between the X-ray luminosity, L_x, and the mass accretion rate, $\dot{M}_x$, provides an additional constraint on the mass loss rate:

$$\frac{\dot{M}_c}{M_c} = \frac{1}{\beta}(\frac{R_x L_x}{G M_c M_x}), \tag{4.12}$$

or, for the parameter of Cen X-3 given below,

$$\dot{M}_c \simeq -6 \times 10^{-9} \frac{1}{\beta}(\frac{L_x}{6 \times 10^{37} \mathrm{ergs\,s^{-1}}}) M_\odot \ \mathrm{yr}^{-1}. \tag{4.13}$$

4.3.1 Mass Loss Dominated Case

To investigate the effects of the above case 1, which orbital decay are dominated by the mass loss, equations (4.9) – (4.11) and equations (4.12) – (4.13) are combined with $\tau \rightarrow \infty$, thus we obtain a relation between the orbital angular momentum loss parameter ξ and the mass capture fraction, β. Figure 4.4 shows this relation for smaller values of the rate of decay of the orbital period in addition to the new value obtained from this work. Because this new result is quite similar value that obtained with Kelly et al. (1983), and it is almost overlapped. Therefore only our new result are plotted in Figure 4.4.

Large values of ξ could be attained if the characteristic "lever arm" for the ejected matter were closer in size to full semimajor axis, a, rather than to the value of a_c as used in equation (4.4). This might seem a more reasonable choice for the case of the mass loss via a moderately high velocity stellar wind, since the specific angular momentum of the matter at the surface of a nearly corotating companion star would be significantly larger than that implied by equation (4.4). But, this angular momentum comes from the rotational angular momentum of the companion star and not directly from the orbit, unless there is the

appropriate coupling by tidal torques. In addition, expected capture fraction from a high velocity stellar wind is $\beta \leq 10^{-3}$ in the Cen X-3 (Davidson and Ostriker 1973; Lamers et al. 1976; Bonnet-Bidaud & van der Klis 1979), and this value leads $\dot{M}_c \geq 6{\times}10^{-6}\ M_\odot\ \mathrm{yr}^{-1}$ from equation (4.13), which is at the high end of the range of the stellar wind mass loss rates expected for a star of spectral type O6–8f (Hutchings et al. 1979): $\sim 2{\times}10^{-7} - 6{\times}10^{-6}\ M_\odot\ \mathrm{yr}^{-1}$ (Abbott et al. 1980; Garmany et al. 1981; Larmers 1981).

A mass loss mode that could yield a large value of ξ ($\geq 10^2$) would occur if much of the matter leaving Krezeminski's star escaped via the Roche lobe overflow by the loss from the system through the Lagrange, L_2, point. The corresponding mass capture fraction obtained from our new result in Figure 4.4 is $\beta \approx 2.3{\times}10^{-3}$. In this picture, matter flows through the inner Lagrange point, L_1, at a rate of $\sim 3{\times}10^{-6} M_\odot\ \mathrm{yr}^{-1}$ calculated from equation (4.13) with only a small fraction captured by the neutron star. This much matter flowing in a relatively thin disk or a streamlike structure with a typical velocity of a few hundred km s^{-1} could result in densities in excess of $\sim 10^{14}\ \mathrm{cm}^{-3}$, and column densities of up to $10^{26}\ \mathrm{cm}^{-2}$. It seems highly unlikely that such a stream of matter would have gone undetected in orbital phase dependent X-ray and optical observations. The column densities obtained with X-ray observations has been of order of only $\sim 10^{22}\ \mathrm{cm}^{-2}$ including with this work, except for the value of $\sim 10^{23}\ \mathrm{cm}^{-2}$ during the pre-eclipsing dips at orbital phase around ~0.6–0.8 (Pounds et al. 1975; Jackson 1975; Schreier et al. 1976). Kelley et al. (1983), therefore, tentatively discount this mode of the mass transfer for driving the orbital decay, although they cannot completely rule out the possibility that we are viewing the system at just the right inclination to observe broad eclipses while avoiding the obscuration effects of such large matter flow.

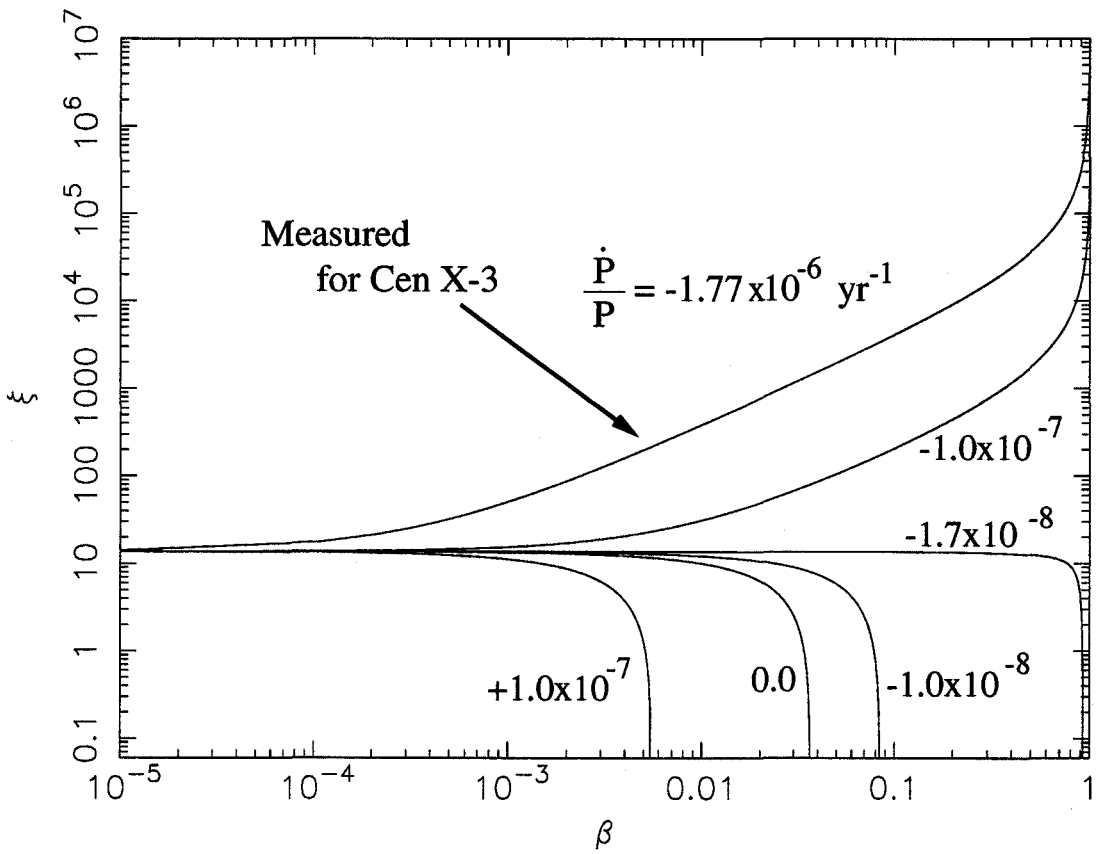

Figure 4.4: Angular momentum loss parameter, ξ, vs mass capture fractions. β. Six solid curves are plotted in this Figure. One of them (the top) gives the relation between ξ and β for the case that the mass and the angular momentum loss from the Cen X-3 system account for the orbital period changes obtained with this work. The other solid curves indicate illustrative values of ξ and β that would result in different rates of orbital period changes (including positive values of $\dot{P}_{orb}$). These curves are calculated for orbital parameters and the X-ray luminosity of Cen X-3. Here we apply $M_x = 1.0M_\odot$, $M_c = 19.0M_\odot$, $R_x = 10.0$ km, and $L_X = 5\times10^{37}$ ergs s^{-1} (see, e.g., Rappaport and Joss 1981; 1983) and $\dot{P}_{orb}/P_{orb} = 1.77 \times 10^{-6}$ yr^{-1} (this work).

4.3.2 Tidal Interaction Dominated Case

To explore the effect of the tidal interaction given by equation (4.6), we will examine equations (4.9) – (4.11) with $f = 0$. In this case, a simple relation between the degree of asynchronism, $(\omega_K - \omega_C)/\omega_K$, and the synchronization time scale, τ. Figure 4.5 shows this relation. As an example, it is found that the observed orbital period decrease can be account for with a synchronization time scale of $\sim 10^5$ yr if the system is out of corotation by only ~10%. The dashed portion of the curve in Figure 4.5 corresponds to a sense of a rotation of the companion star that is opposite to that of an orbital motion.

Zahn et al. (1975, 1977) gives an expression for the tidal torque for the case of radiatively damped dynamical tides. When we apply the Zahn's (1977) equation (5-6), equation (4.6) can transform into

$$N_x^t = -I_c \frac{(\omega_K - \omega_C)}{\tau_D} \left(\frac{(\omega_K - \omega_C)}{\omega_K}\right)^{5/3}. \tag{4.14}$$

Here

$$\tau_D^{-1} = 3 \times 2^{5/3} \frac{GM_c}{R_c^3}^{1/2} \frac{R_c}{a}^{17/2} \eta^{-1} q^2 (1+q)^{5/6} E_2, \tag{4.15}$$

and E_2 is Zahn's tidal coefficient. Kelley's definition of τ_D is the same to within a factor 5/3 of Zahn's t_{sync} (Zahn's (1977) equation (7a)). Then, equation (4.9) with $f = 0$ becomes

$$\frac{\dot{P}_{orb}}{P_{orb}} = -3g \left(\frac{\omega_K - \omega_C}{\omega_K}\right)^{8/3} \frac{1}{\tau_D}. \tag{4.16}$$

This equation gives a simple relation between τ_D and $(\omega_K\text{-}\omega_C)/\omega_K$, which is also shown in Figure 4.5. The numerical value of E_2 for a Krezeminski's star is probably in the range 3×10^{-6} – 1×10^{-5} (Zahn 1975,1977). From Figure 4.5, we can infer a value of ~20% for $(\omega_K - \omega_C)/\omega_K$.

From the above discussion as described in Kelley et al. (1983), to explain both the magnitude and the sign of the overall long term orbital period changes, the mass loss and concomitant orbital angular momentum loss in Cen X-3 is probably insufficient by itself (i.e., in the absence of tidal effects), and the tidal effect is needed to explain the long term orbital period changes, even if we include our new result. (see detailed discussions in van den Heuvel and de Loore 1973; Wheeler, McKee, and Lecar 1974; Sparks 1975; Chevalier 1975; Fabbiano and Screier 1977; Thomas 1977). Moreover, Kelley et al. (1983) also suggests it is quite plausible that the observed long term orbital period decrease could be due largely to tidal effects.

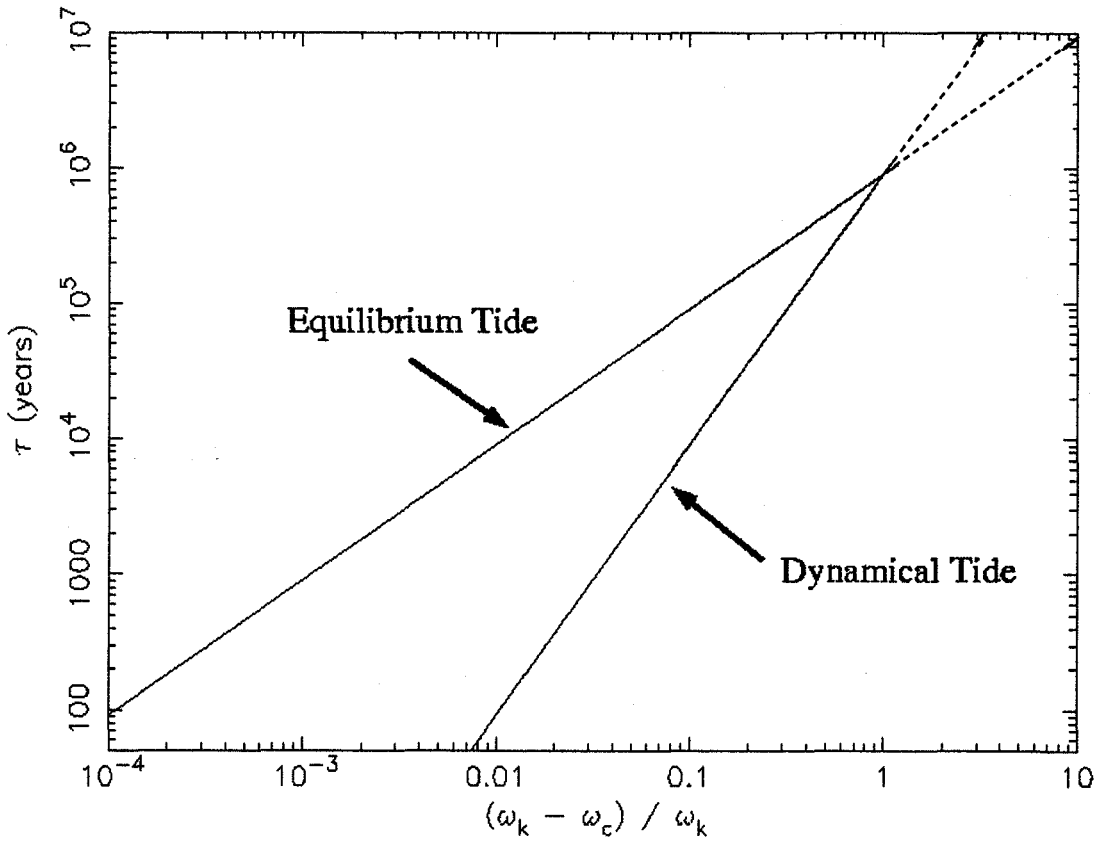

Figure 4.5:

Relation between the synchronization time scale, τ, and the synchronism parameter, $\gamma = (\omega_K - \omega_C)/\omega_K$, required to explain the observed rate of decrease in the orbital period of Cen X-3. Synchronism corresponds to $\gamma = 0$, the tidal case to $\gamma = 1$, and counter-rotation to $\gamma > 1$. The curves labeled "equilibrium tide" and "dynamical tide" are plotted, with $f = 0$ (pure tidal interaction), and $\dot{P}_{orb}/P_{orb} = -1.77\times10^{-6}$ yr^{-1}. Here, we applied $R_c/a = 0.65$ (Rappaport and Joss (1983)), and adopted a value for $\eta = 0.06$ (Kelley et al. 1983).

Chapter 5

Analysis and Result of *RXTE* Observations

In this chapter, we will describe our method to analyze the *RXTE* PCA data. At first we will show the way to reduct the PCA data. Next, we will show the results of the determination of the binary phase and the energy spectral analysis of Cen X-3. At last of this chapter, we will show the result of cross spectral analysis of Cen X-3.

5.1 Data reduction and its Procedure

The first step in the analysis procedure is the conversion of PCA raw data files provided by the *RXTE* Guest Observer Facility (GOF) into meaningful X-ray counts spectra and light curves. This is done in a straight forward manor using the `HEAsoft` analysis tools released by NASA. The entire data collection process is outlined in "The RXTE Cook Book : Recipes for Data Analysis and Reduction", provided by the High Energy Astrophysics Science Archive Research Center (HEASARC) and is available via the WWW at the *RXTE* GOF. Further information can be found in "The ABC of XTE" guide which is, also available at the *RXTE* Guest Observer web site.

5.1.1 Data Collection

In order to determine source "goodtime" intervals, in which we extracted the source (or background) photons, we used the following data selection criteria.

We have to consider about two kinds of contamination by X-rays from the Earth's limb and by high energy particle during the passage of South Atlantic Anomaly (SAA). To avoid the contamination by X-rays from Earth's limbs, the data was accumulated only when the

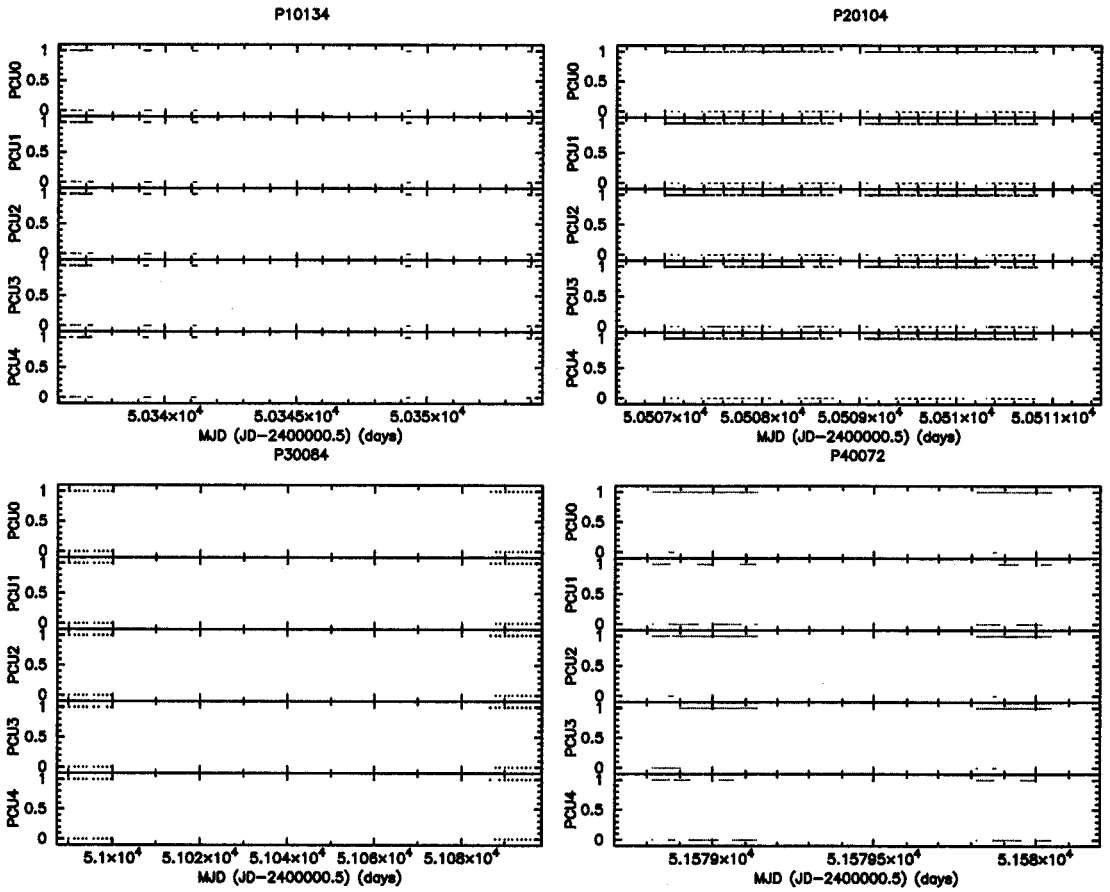

Figure 5.1: The history of the high voltage status of each PCA of each observations. The vertical axis of each panel means that 1 is the turning on the high voltage and 0 is the turning off the high voltage, respectively. The horizontal axis is the time based on the MJD.

satellite was pointing more than 10° above the horizon. To exclude the PCA data obtained during the passage through the SAA, we rejected data from a 30 min interval beginning with the satellite entering the SAA because the PCA detector was activated during SAA and the background increased significantly after the passage of SAA. We also excluded data obtained when the difference between the actual pointing direction and the scheduled direction is larger than 1.2 arcmin since the attitude of satellite is not stable just after changing the pointing direction. In addition, especially when *RXTE* PCA observes a faint source, it is required to filter out time when electron rate in each of the accumulate PCUs is larger than 0.10. These kind of electrons creates background components by interaction with spacecraft or detector body. But we neglected this criterion because the Cen X-3 was a bright source.

In March 1996, PCU3 and PCU4 began to experience occasional breakdowns. Since then, the HV of all the PCUs have been carefully managed to prevent further damage. Figure 5.1

shows that the history of the high voltage of each PCU during observations of Cen X-3.

For spectral analysis, we used the data from all 5 PCUs (PCU0, PCU1, PCU2, PCU3, and PCU4). The PCUs have three xenon layers (so called X1, X2, and X3) and each of them consists of two anodes chains (so called Left and Right). The top layer detects roughly 90% of the cosmic photons and 50% of the internal instrumental background. Thus, the best signal-to-noise especially for weak sources are achived by selecting only events from the top layer (X1) and by excluding events from the mid and bottom layers. But, for timing analysis, we accumulate all PCUs data (PCU0, PCU1, PCU2, PCU3, and PCU4) and all layers (X1, X2, and X3) from the statistical point of view.

Table 5.1: Screening criteria for *RXTE* PCA analysis

screening item	screening criteria
Elevation	$< 10.0°$
Attitude stability	< 1.2 arcmin
Time since SAA	>30 min
Electron Rate	< 0.1
PCU (for spectral analysis)	PCU0,PCU1,PCU2,PCU3,PCU4
PCU (for timing analysis)	PCU0,PCU1,PCU2,PCU3,PCU4
Xenon Layer (for spectral analysis)	X1
Xenon Layer (for timing analysis)	X1, X2, X3

Next we estimated the PCA background for each observation. Since the PCA is not an imaging detector like a CCD, a modeled background has to be subtracted from the source data. The PCA background consists of two components. One is the diffuse sky background which enters through the collimator as X-rays, and the other is the internal background which arises from interactions between radiation or particles in an orbital environment with the detector or the spacecraft. While the diffuse sky background is assumed to be constant at any one pointing position, the internal background may vary as the detectors move through a different ambient condition. The estimation of background is based on the detailed modeling of activation, especially during the SAA passage and instantaneous particle flux coming into the detector.

To estimate those background, we used the latest version of `pcabackest` supplied from *RXTE* Guest Observer Facility (GOF). It was assumed that the internal background varies on a long time scale compared to 16 s, the natural time scale of the PCA `Standard-2`

data mode. The background model was evaluated once every 16 s, and the equivalent of a `Standard-2` data file was created with separate information for each detector and each anode chain. We applied all of the goodtime intervals to the output files from `pcabackest` when we analyzed `Standard-2` data to obtain the energy spectra of Cen X-3. But, for timing analysis, we concentrated on the faster time variation than that of background, we did not subtract the background data from the obtained light curve.

Figure 5.2 shows the example of both source and background light curves summed over the top layer (X1) of three PCUs (PCU0, PCU1, and PCU2) detectors with the binning time of 128 s. The upper data sets are the source light curve including the background photons, and the lower is the modeled background light curve. Then, we subtracted the background light curve from the source light curve to obtain the background subtracted light curve. Figure 5.5 shows the background subtracted light curve.

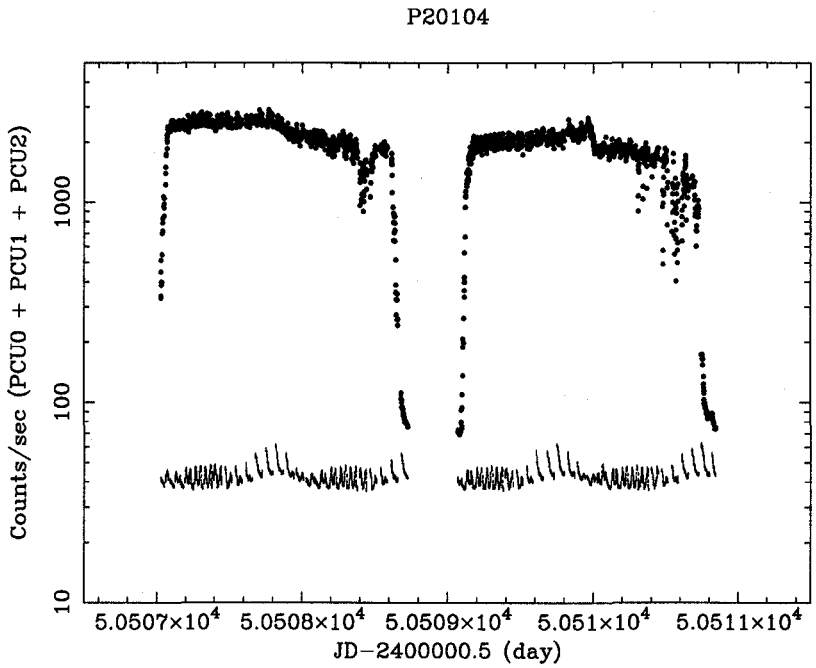

Figure 5.2: Source and background light curves obtained with *RXTE* PCA `Standard-2` mode. Upper data sets are the source light curve of Cen X-3 and the lower are the background light curve. The data of top layer (X1) of PCU0, PCU1, and PCU2 are accumulated.

Figure 5.3 shows the example of both source and background energy spectra summed over the photons detected only the top layer (X1) of three PCUs (PCU0, PCU1, and PCU2) detectors. The upper data sets are the photon counts from the source including the background, and the lower are the modeled background. Line features are present due to Cu fluorescence (~8 keV, primarily from the backplane), unflagged calibration events, and a contribution which appears to come from residual activity in the collimator.

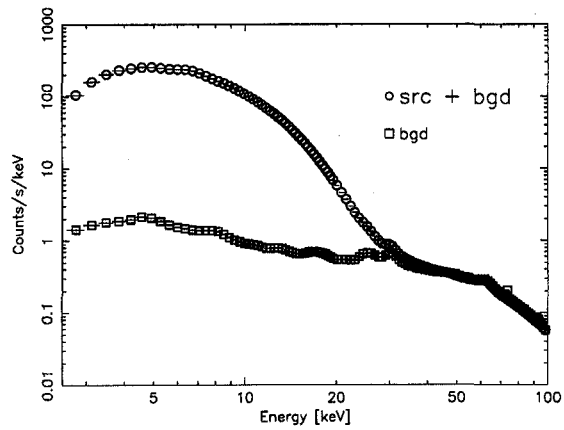

Figure 5.3: Source and background energy spectra obtained with *RXTE* PCA `Standard-2` mode. The data of top layer (X1) of PCU0, PCU1, and PCU2 are accumulated.

5.2 Temporal Timing Analysis of PCA Data

In this section, at first we will show the light curves of Cen X-3 obtained with *RXTE* PCA and their binary phases. Next, we will show the results of timing analysis to search the QPO using power spectral density.

5.2.1 Light Curves and Binary Phases

Here we will show the light curves of Cen X-3 obtained with *RXTE* PCA `Standard-2` mode. Count rates are extracted from the sum of X-ray photons in the energy range from 2.5 keV to 50 keV detected with the top layer (X1) of each PCU0, PCU1, and PCU2 data. In addition we will show the Doppler curve of the pulse period to determine the orbital period for each observation.

- P10134

  This observation was carried out between 1996 September 10 and September 27 for five times, and this data was published by Audley et al. (1998). During this observation, Cen X-3 alternated between its high state and extended low state. The data was taken using binned data mode `B_16ms_64M_0_249` as well as `Standard` (`Standard-1` and `Standard-2`) mode. The binned mode of `B_16ms_64M_0_249` is 16 ms time resolution with 64 spectral channels rebinned the original channels from 0 to 249 channel.

  To determine the orbital phase of this observation, we used the data obtained with `B_16ms_64M_0_249` mode, and we collected the data with energy range from 2.5 keV to 50 keV. Then, we carried the barycentric correction by using `fxbary` and calculated the power spectrum to obtain the pulse period of each observation. The right panel of Figure 5.4 plots the calculated pulse period as a function of the MJD. We could not get any pulsation from #4 observation in Figure 5.4. Next we fitted the obtained Doppler curve with a sinusoidal model. The projected semi-major axis, $a_x \sin i/c$, was fixed to the value of 39.81 lt-s derived in the previous chapter 4, and the $\dot{P}_{spin}$ and ellipticity, e, were assumed to be zero. The eclipse center time was derived using the value predicted by our result (see previous chapter 4), and fixed the eclipse center time to be 50335.6533 d (MJD). Two free parameters were used in the fit: orbital period and spin period. The best fit parameters are shown in Table 5.2, and calculated orbital phases are shown in Table 5.3, respectively.

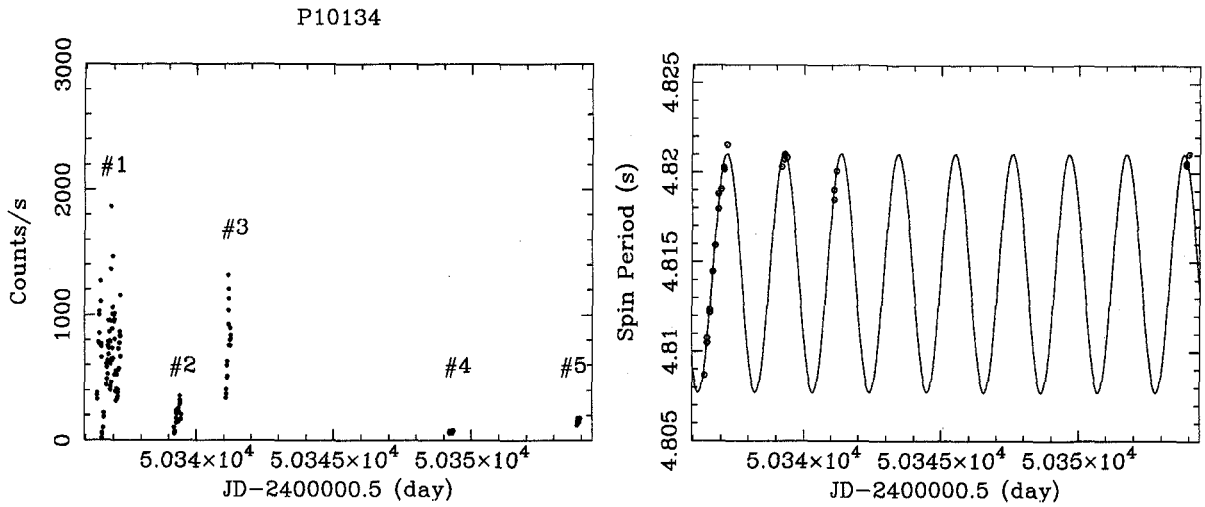

Figure 5.4: *Left*: The PCA light curve of Cen X-3 (P10134). # mark means the observation number and is described as reference. *Right*: Doppler curve of the pulse period and the best fit orbit.

Table 5.2: Orbital parameters obtained with P10134

P_{orb}	2.084±0.002 (d)
P_{spin}	4.8±0.2 (s)
Eclipse Cnter time (fixed)	50335.6533 (MJD)
$a_x \sin i/c$ (fixed)	39.81 (lt-s)
$\dot{P}_{spin}$ (fixed)	0
e (fixed)	0

Table 5.3: Orbital phase of P10134

Number	start (MJD)	Exposure (s)	orbital phase
#1	50336.390	17423	0.35–0.75
#2	50339.180	3712	0.69–0.80
#3	50341.036	4060	0.58–0.67
#4	50349.004	3949	0.73–0.78
#5	50353.835	4485	0.72–0.80

- P20104

  Here, we just show the light curve and the Doppler curve of the pulse period (see Figure 5.5) and the best fit orbit as compared since we described the light curve and its orbital parameter in previous chapter 4 in detail. This observation was carried out from 1997 February 28 to 1997 March 3, and this data was archived by Jernigan et al. (2000) and by Kohmura et al. (2001). Eclipses and pre-eclipsing dips observed just before eclipse ingress were clearly seen. This data was taken by the binned data mode `B_16ms_16A_0_35_H` as well as `Standard` mode. This binned mode was 16 ms time resolution with 16 spectral channels rebinned the original channels from 0 to 35 channel.

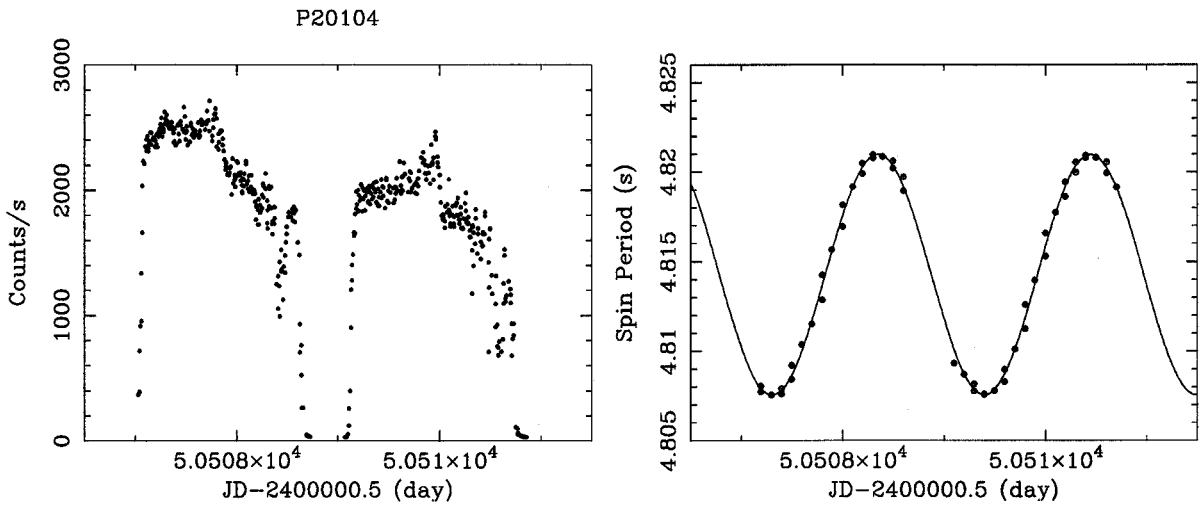

Figure 5.5: *left*: The PCA light curve of Cen X-3 (P20104). *right*: Doppler curve of the pulse period and the best fit orbit.

- P30084

  This observation was carried out between 1998 June 28 and July 5 for ten times, and this data has not been published yet by any authors. In this observation, the data was taken using two binned data mode `B_4ms_16A_0_35_H` and `B_16ms_64M_0_249` and as well as `Standard` mode. The binned mode of `B_16ms_64M_0_249` is 16 ms time resolution with 64 spectral channels rebinned the original channels from 0 to 249 channel, and `B_4ms_16A_0_35_H` is 16 ms time resolution with 16 spectral channels rebinned the original channels from 0 to 35 channel.

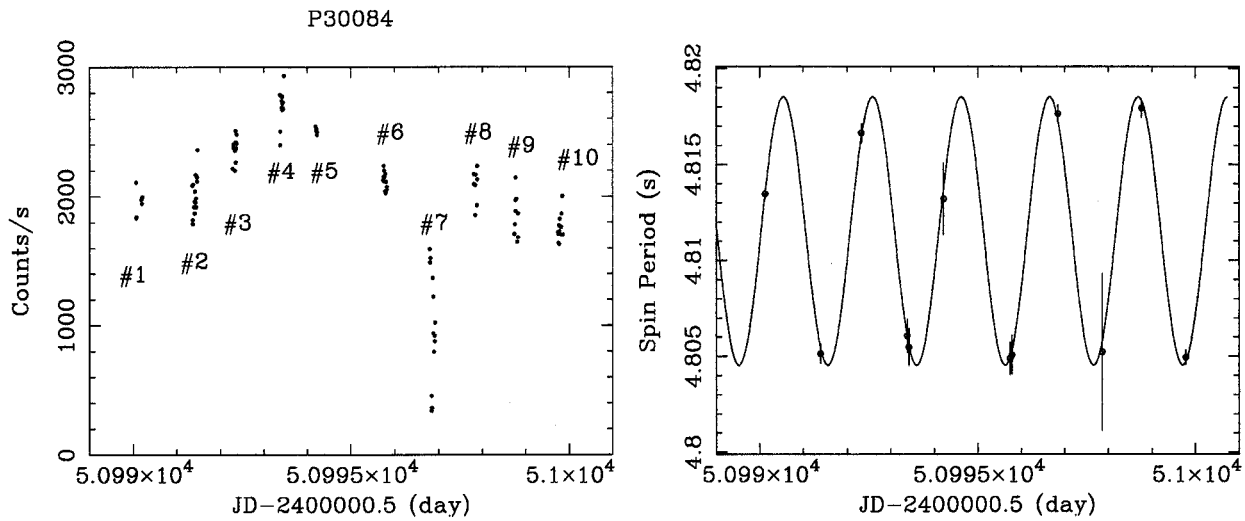

Figure 5.6: *left*: The PCA light curve of Cen X-3 (P30084). The # number is described as reference. *right*: Doppler curve of the pulse period and the best fit orbit.

To determine the orbital phase, we used the data obtained with both observation mode of `B_16ms_64M_0_249` and `B_4ms_16A_0_35_H`, and we analyzed the same procedure as described for P10134 observation. To fit the Doppler curve of the pulse period with a sinusoidal function, the eclipse center time was derived using the value predicted by our result (see previous chapter 4), and fixed the eclipse center time to be 50993.0711 d (MJD). Two free parameter were used in the fit: orbital period and spin period. The best fit parameters are shown in Table 5.4, and the calculated orbital phase are shown in Table 5.5, respectively.

Table 5.4: Orbital parameters obtained with P30084

P_{orb}	2.0947±0.0005 (d)
P_{spin}	4.8114±0.0002 (s)
Eclipse Center time (fixed)	50993.0711 (MJD)
$a_x \sin i/c$ (fixed)	39.81 (lt-s)
$\dot{P}_{spin}$ (fixed)	0
e (fixed)	0

Table 5.5: Orbital phase of P30084

Number	start (MJD)	Exposure (s)	orbital phase
#1	50989.953	6249	0.51–0.58
#2	50991.351	3648	0.18–0.22
#3	50992.280	3632	0.62–0.66
#4	50993.360	3184	0.14–0.17
#5	50994.198	1096	0.54–0.59
#6	50995.726	3552	0.27–0.31
#7	50996.794	4728	0.78–0.83
#8	50997.862	464	0.29–0.29
#9	50998.726	3376	0.70–0.73
#10	50999.726	4696	0.17–0.23

- P40072

  This observation was carried out between 2000 February 4 and February 5 for six times, and this data has not been published yet. In this observation, the observation data was taken using two binned data mode `GoodXenon` as well as `Standard` mode. The `GoodXenon` is $\sim$1 μs time resolution with 256 spectral channels.

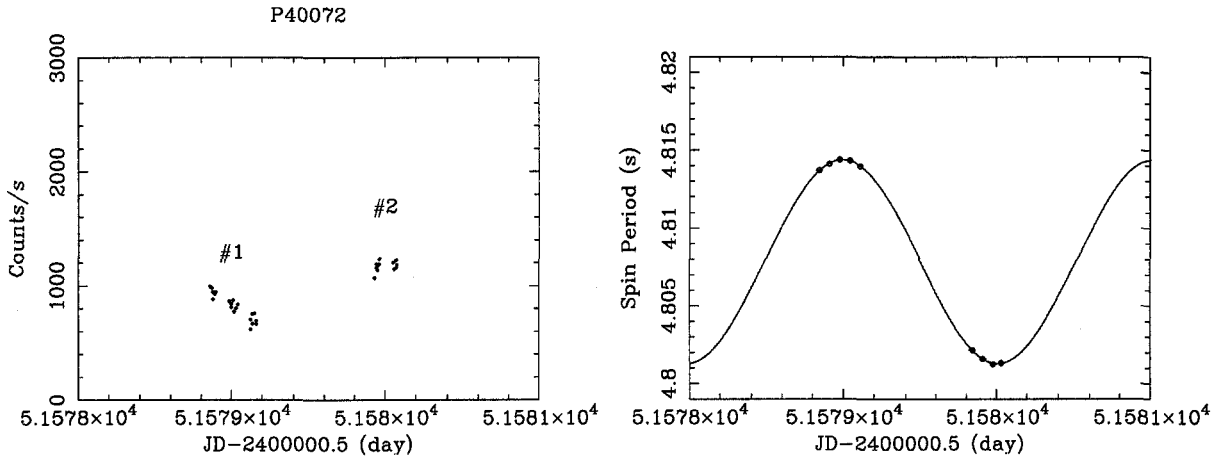

Figure 5.7: *left*: The PCA light curve of Cen X-3 (P40072). We called former three observations #1 and the later two observation as #2. These # number are described as reference. *right*: Doppler curve of the pulse period and the best fit orbit.

When we determined the orbital phase of this observation, we used the data obtained with `GoodXenon` and analyzed the same procedure as described for P10134 observation. To fit the Doppler curve of the pulse period with a sinusoidal function, the eclipse center time was derived using the value predicted by our result (see previous chapter 4) and fixed the eclipse center time to be 51579.5029 d (MJD). Two free parameter were used in the fit: orbital period and spin period. The best fit parameters are shown in Table 5.6, and the calculated orbital phase are shown in Table 5.7, respectively.

So far, we have determined the orbital phase of each observation of Cen X-3. As shown in Figure 5.5, some observations might were carried out during the eclipses and pre-eclipsing dips. The data during the eclipses as well as the pre-eclipsing dips might have rich information on the circumstellar matter (Nagase et al. 1992). For our purpose to determine the distance between the neutron star and the reprocessor using the cross spectral analysis, however, we need data obtained in a simple physical situation without both the eclipses and the pre-eclipsing dips. Therefore, we excluded the data during both eclipses and pre-eclipsing

Table 5.6: Orbital parameters obtained with P40072

P_{orb}	2.1025±0.0004 (d)
P_{spin}	4.80782±0.000004 (s)
Eclipse Center time (fixed)	51579.5029 (MJD)
$a_x \sin i/c$ (fixed)	39.81 (lt-s)
$\dot{P}_{spin}$ (fixed)	0
e (fixed)	0

Table 5.7: Orbital phase of P40072

Number	start (MJD)	Exposure (s)	orbital phase
#1	51578.844185	9100	0.67–0.82
#2	51579.841696	6360	0.16–0.27

dips from this work, referring these orbital phases and results of the energy spectral analysis discussed later.

5.2.2 Search for QPOs

As mentioned before, some authors reported the QPO from Cen X-3 (Tennant et al. 1988, Takeshima et al. 1991; Audley et al. 1996). We tried to detect the QPO from the data obtained with *RXTE* PCA. Except for P10134 data, we could detect the QPO around ~40 mHz as follows.

QPO from P20104, P30084, and P40072 Observations

The power spectral densities (PSDs) calculated from P20104 observation data in the energy band 3.3-13.1 keV and in the frequency range 0.004–32 Hz are shown in Figure 5.8. These power spectral densities were computed by co-adding 316 separate power spectral densities derived from 256 s exposure with 15.625 ms time resolution. The noise due to Poisson statistics component was subtracted. The fundamental and higher order harmonics of 4.8 s pulsation were detected, and a broad peak around ~40 mHz was also detected.

To determine the centroid frequency of the QPO, we fitted this PSD with a model of narrow lines, a broken-power law, and a Lorentzian (Takeshima et al. 1994). As a result, the QPO component was confirmed with the centroid frequency of 41±3 mHz. Aperiodic time variation was significantly detected up to ~25 Hz.

This observation covers two orbital phases, and we divided this observation into two phases, so called "seg1" and "seg2". Then, we calculated the PSDs using the data of seg1 and seg2 (see Figure 5.8), respectively. The the centroid frequency of the QPO of each observation was consistent with each other within one σ error.

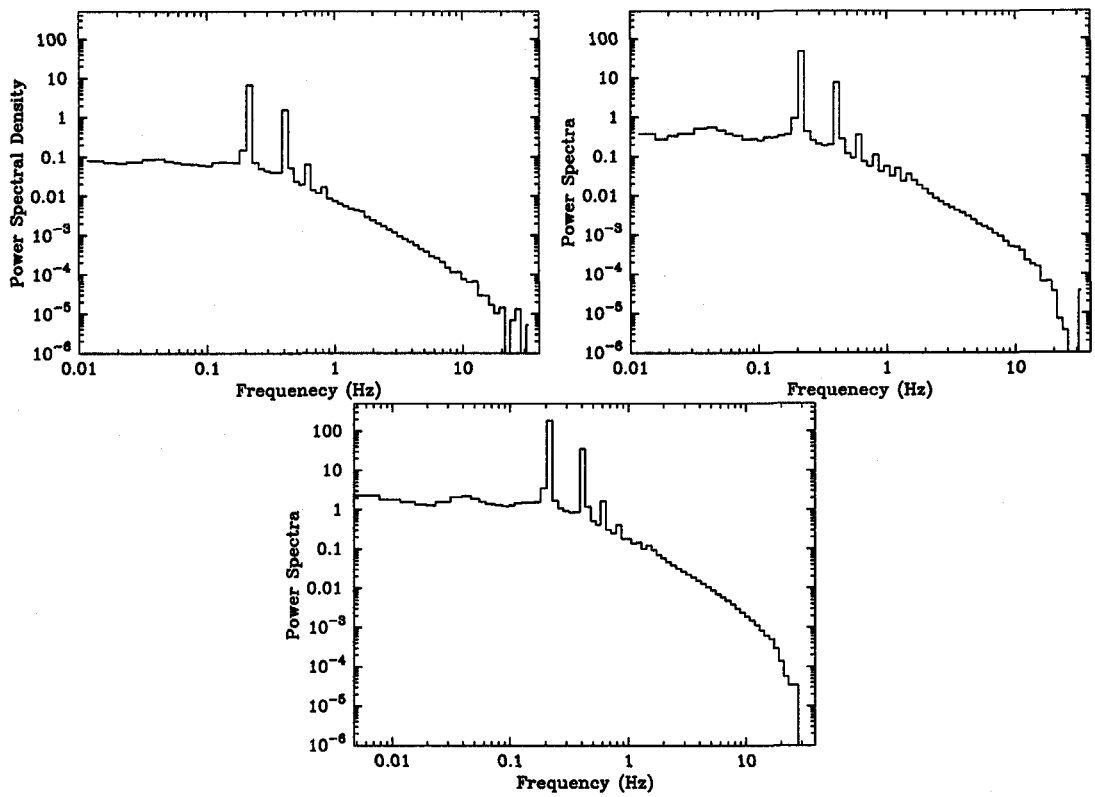

Figure 5.8: Upper two panels show the PSDs obtained from seg1 and seg2 of P20104, and their centroid frequencies of QPOs are 40±5 mHz and 42±2 mHz respectively. Lower panel shows the PSD obtained from all data of P20104 in the energy range from 3.3 keV to 13.1 keV, excluding data during eclipses and pre-eclipsing dip intervals. The centroid frequency of QPO is 41±3 mHz.

We also calculated the PSD for the other two observation data, P30084 and P40072 using the same method in P20104. As mentioned in the previous subsection 5.1.1, two different PCA observation mode, `B_16ms_64M_0_249` and `B_4ms_16A_0_35_H`, were used during P30084 observation, and we calculated the PSD for each observation mode (Figure 5.9). Figure 5.10 shows the PSD derived from P40072 observation.

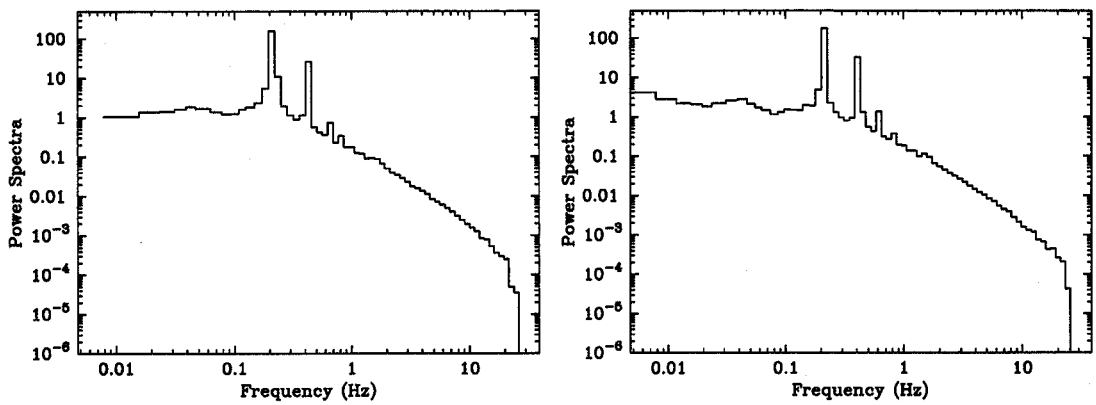

Figure 5.9: *left*: The data during the #1 – #5 (`B_4ms_16B_0_249_Q` mode) observation of P30084 detected the QPO with the centroid frequency 46±4 mHz. *right*: The data during the #6 – #10 (`B_4ms_16A_0_35_H` mode) of P30084 observation also detected the QPO with the centroid frequency 39±1 mHz.

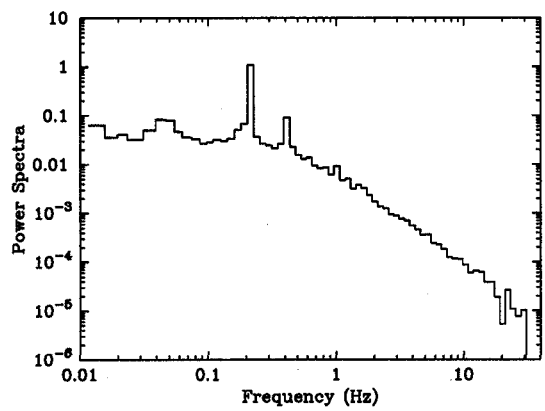

Figure 5.10: The power spectral density obtained for P40072 observation in the energy range from 3.2 keV to 50.0 keV. The QPO was clearly detected around 46±1 mHz.

Results of QPO Search

We obtained the QPOs from three observations with *RXTE*. These results are summarized in the Table 5.8. These QPO frequencies are ranging from 39 mHz to 46 mHz. A little high frequencies of 46 mHz were detected in P30084 (#1 – #5) and P40072. These data is containing high energy X-rays. As shown in Figure 5.10, the QPO of P40072 data shows a narrow peak.

All of our results of QPOs show higher frequency than that of obtained by *Ginga* (Takeshima et al. 1991) of 35 mHz. Figure 5.11 shows our results of the QPO frequency plotted as a function of observed X-ray flux. In addition, the QPOs obtained with *Ginga* (Takeshima et al. 1991) and *BBXRT* (Audley et al. 1996) are also plotted in this Figure.

Figure 5.11 may suggest that the QPO frequency obtained from Cen X-3 is positively correlated to the observed X-ray flux and may be related to the QPO mechanism. But, as mentioned in the previous chapter 2, this results depends on X-ray spectral band. In our data, we used three kind of data, due to the PCA observation mode, in the energy range of 3–13, 3–34, and 3–50 keV. Takeshima et al. (1991) used 1–37 keV and Audley et al. (1996) used 1-10 keV. Then, we could not determined whether Figure 5.11 implied the positively correlated to the observed X-ray flux or not. In our thesis, the change of the centroid frequency of the QPO is rather small, and this only little affects on the size of the Alfv́en radius (see equation 6.2), and we don't discuss it here.

Table 5.8: Detected QPO frequency obtained from *RXTE* PCA.

Obs ID	QPO frequency (mHz)	Energy range (keV)	Number of co-adding PSDs
P20104 (all data)	41±3	3.3–13.1	316
P20104 (seg1)	40±5	3.3–13.1	160
P20104 (seg2)	42±2	3.3–13.1	142
P30084 (#1–#5)	46±4	3.6–34.1	134
P30084 (#6–#10)	39±1	3.3–13.1	123
P40072	46±1	3.2–50.0	62

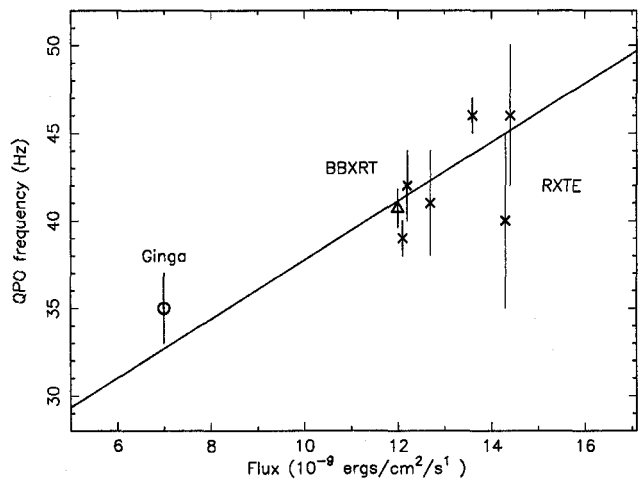

Figure 5.11: QPO frequency obtained from Cen X-3 as a function of observed X-ray flux. The open circle and the triangle are the data obtained with *Ginga* (Takeshima et al. 1991) and *BBXRT* (Audley et al. 1996), and their centroid frequencies are 35±2 mHz and 40.7±1.1 mHz. Cross marks are our derived results with *RXTE*. The linear function are also plotted as a just for reference.

5.3 Spectral Analysis

In this subsection, we will show the result of our energy spectral analysis of Cen X-3 obtained with *RXTE* PCA `Standard-2` mode. The energy spectra obtained with `Standard-2` mode has 129 energy channels in the energy range 2-100 keV, but we ignored the energy spectra below 2.5 keV because of the uncertainty of its response function.

5.3.1 Fitting Model

So far, some spectral fitting model have been applied to fit the energy spectra of X-ray binary pulsars. Especially, when searching for Cyclotron Resonance Scattering Features (CRSFs), having a good model of the underlying continua that the lines modified is very important, because CRSFs can be such a subtle and rather broad feature in the energy spectrum that its identification depends critically on the modeling of the shape of the underlying X-ray continuum.

There are three major analytic realizations of the spectrum shape of accretion powered pulsars; the power-law with a high energy cutoff (*PLCUT*), a power-law with a Fermi-Dirac form of the cutoff (*FDCO*), and dual power-laws with opposite signs along with an exponential cutoff (*NPEX*).

Here we will review these continuum models and the model for CRSFs.

- *ECUT*

  The historical version of the standard spectral model for the continuum X-ray is the power-law with a high energy cut off (*ECUT*). This model is described as follows (White, Swank & Holt 1983).

$$ECUT(E) = AE^{\alpha} \times \begin{cases} 1, & for\, E \leq E_{cut} \\ e^{-(E-E_{cut})/E_{fold}} & for\, E \geq E_{cut}. \end{cases} \tag{5.1}$$

  Here, *ECUT* is the photon number flux, E is the X-ray energy, α is the spectral photon index, E_{cut} is the energy where the spectrum breaks (so-called "cutoff energy"), and E_{fold} is the folding energy describing the cutoff steepness. But, this model has a problem of having a discontinuous derivative at the cutoff energy E_{cut}, while the source spectrum probably dose not have such a sudden change. This "kink" in the model can cause line-like residual errors at the cutoff energy (Makishima et al. 1990).

- *FDCO*

  Another standard model for the continuum X-ray, proposed Tanaka (1986), and Makishima et al. (1992), is the Fermi-Dirac cutoff power-law (*FDCO*). This is of the form:

$$FDCO(E) = AE^{-\alpha} \times \frac{1}{1 + e^{(E-E_{cut})/E_{fold}}} \tag{5.2}$$

  where E_{cut} and E_{fold} are the cutoff and folding energies of this model. The chief advantage of this model is that it has a smooth and continuous turnover. There are, however, very different forms of an exponential cutoff, and the fitting parameters from *ECUT* and *FDCO* can not be directly compared each other. Although the *FDCO* cutoff is the same as the Fermi-Dirac distribution from statistical mechanics, it is used solely for its analytic shape and not because of some underlying fundamental physics.

- *NPEX*

  Another spectral shape that approximates the continuum X-ray avoiding a discontinuity is the Negative and Positive power-law EXponential (*NPEX*), first suggested by Mihara (1995). It is realized in the form:

$$NPEX(E) = (A_n E^{-\alpha 1} + A_p E^{+\alpha 2}) \times e^{-E/kT} \tag{5.3}$$

  where $\alpha 1$ and $\alpha 2$ are both positive numbers, and kT is a typical temperature of the X-ray emitting plasma.

  The physical meanings of *NPEX* continuum is as follows; it approximates a photon number spectrum for an unsaturated thermal Comptonization (e.g., Sunyaev & Titarchuk 1980; Mészaros 1992) in a plasma of temperature T. At low energies, it reduces to the ordinary power law with negative slope. As the energy increases, the positive power-law term becomes progressively dominant, so that the model can take a concave curvature on a log-log plot in the energy spectrum. At $E \sim kT$, the positive power-law term simulates the Wien hump in the Comptonized radiation, especially when the positive photon index is fixed at the value of $+\alpha 2 = 2.0$. Finally, for $E \gg kT$, the model exhibits a thermal rollover with temperature T.

  Mihara (1995) found that this model fitted a wide variety of energy spectrum of accretion powered pulsars observed with *Ginga* satellite in the energy range of 1.5–37.0 keV. But, Cobrun (2001) reported that when fitting the full *RXTE* energy range (i.e., 2.5–100.0 keV) this form can not always be applied successfully.

- Cyclotron Resonance Scattering Features ($CRSFs$)

  As mentioned the previous chapter 2, CRSFs in the energy spectrum have detected in many accretion powered pulsars and have been successfully modeled with the simple analytical model, so-called "CYCLABS". This is realized in the form:

$$CYCLABS(E) = e^{-(\tau 1+\tau 2)}, \quad \tau 1 = \frac{D_1(W_c E/E_c)^2}{(E-E_c)^2 + {W_c}^2}, \quad \tau 2 = \frac{D_2(2W_c E/2E_c)^2}{(E-2E_c)^2 + (2W_c)^2} \tag{5.4}$$

  where τ_1 is the optical depth of the fundamental cyclotron scattering in a cold plasma. τ_2 is that for the 2nd harmonic. E_c is the resonance energy, W_c is the width of the resonance, and D_1 and D_2 are the depths of the resonances.

Historically, before the discovery of the CRSF in Cen X-3, the 1–40 keV X-ray spectrum of Cen X-3 was fitted by a power law with a high energy cutoff, iron line, and a soft X-ray absorption (White et al. 1983). The energy spectrum obtained by *Ginga* (Nagase et al. 1992) showed that the high energy cut off was better modeled by a quasi-Lorentzian high energy turn over resembling effects of the CFRS, rather than by the usual e-folding energy cutoff, although their fit did not provide the firm evidence of the CRFS, because the energy of the cyclotron line ($\sim$30 keV) was very close to the upper end of the *Ginga* LAC detectors. The presence of cyclotron line at $\sim$30 keV was confirmed by Santangelo et al. (1998) and Burderi et al. (2000) using the data obtained by *BeppoSAX* in the energy range from 0.1 to 100.0 keV. They were succeeded in fitting the energy spectrum applying the model – a power law with a high energy cutoff and cyclotron absorption lines plus a gaussian emission line, taking into account photo-electric absorption.

The energy spectrum obtained by *RXTE* PCA is ranging upto $\sim$50 keV. The best model to apply to our model seems to be the model used by Burderi et al. (2000), because it reasonably fits all over the spectral shape upto the high energy range, though it is rather inconvenient model. In this thesis, we will apply the model of Burderi et al. (2000).

5.3.2 Fitting Results of each Observation

In this subsection, we will show the phase averaged energy spectrum of Cen X-3 and their fitting results.

- P10134

  It is known that pre-eclipsing dips occures at the phase between 0.6 and 0.9 (e.g., Nagase et al. (1992)). Therefore we first checked our derived orbital phases (see Table 5.3), and found that the #2 and #5 might contain the pre-eclipsing dips.

  Second, we analyzed each energy spectrum and fitted the data as follows (see Figure 5.14). The typical characteristics of energy spectrum during pre-eclipsing dip is heavier absorption in the soft X-ray energy than the other orbital phase except for an eclipse. To compare the photo-electric absorption with each observation, we fixed the photon index $\alpha = 0.91$ which was the value of #1 observation. Figure 5.12 shows the photo-electric absorption value of each observation.

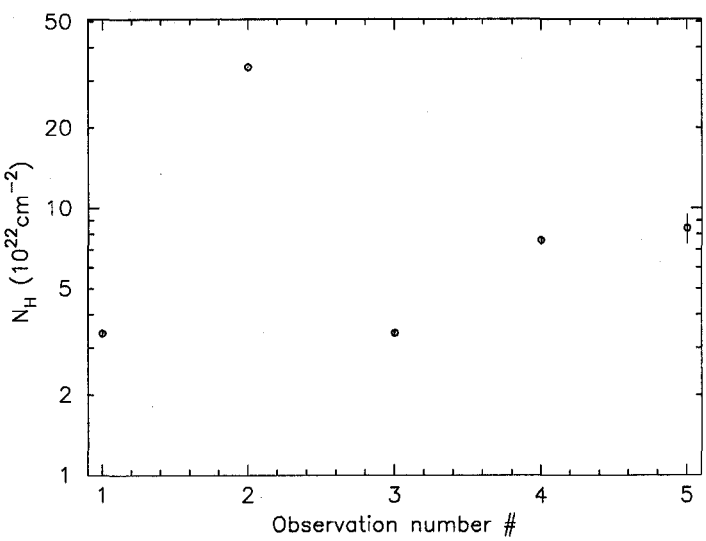

Figure 5.12: The photo-electric absorption compared with each observation, #1, #2, #3, #4, and #5.

  Except for #3, the photo-electric absorption was larger than that of #1. Then, considering both the orbital phase and the photon absorption, we determined that three observations,#2, #4, and #5, included the pre-eclipsing dips. Thus, we did not use them in this work.

Finally, we extracted the energy spectrum only using #1 and #3. Figure 5.13 shows the extracted energy spectrum and its best fit model. Although the model was formally rejected with reduced χ^2 of 12.2, the overall spectral shape and the region around iron K line were well represented by this model. The derived best fit-parameters are summarized in Table 5.9.

The equivalent width of the iron line is 386±3 eV and the line center energy is 6.475±0.004 keV (here and after, the errors are 1-σ statistical errors unless otherwise stated). Thus, it is confirmed that the dominant emission around ~6.4 keV is the K line emission from irons in low ionization state. But, the equivalent width of the iron line, 386 eV, is much larger value by factor of 3 than the other observations (P20104, P30084, and P40072), and the photon index of this observation is smaller than the other observation. Moreover, the light curve shown in Figure 5.4 shows a big fluctuation. These facts imply that the #1 and #3 observations also include the pre-eclipsing dip.

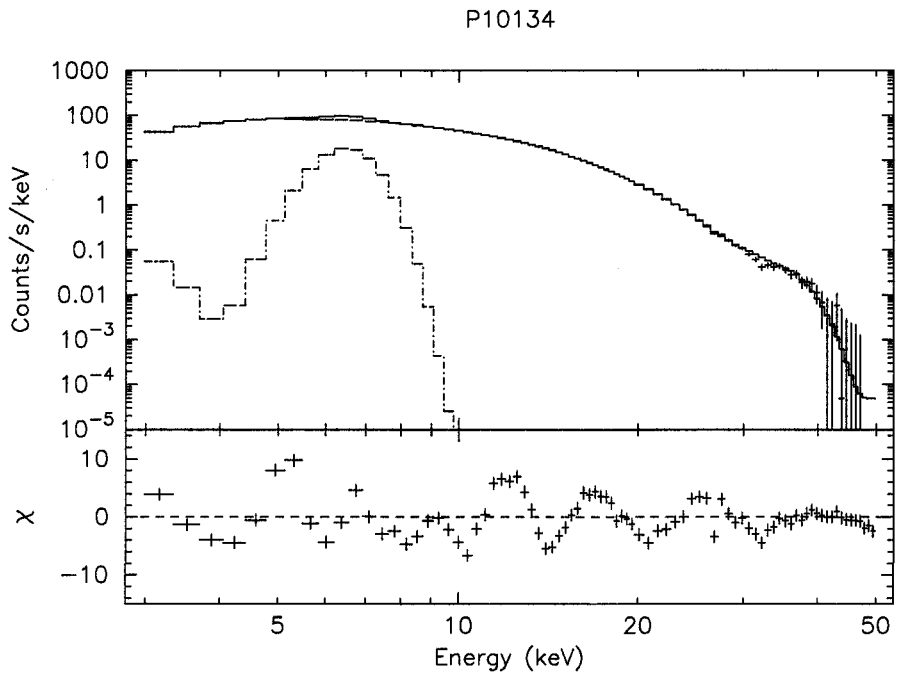

Figure 5.13: The energy spectrum obtained with `Standard-2` mode of P10134. This energy spectrum was extracted only from #1 and #3. The best fit curve is also plotted in this Figure. The lower panel shows the residuals in units of standard deviation with respect to the best fit model.

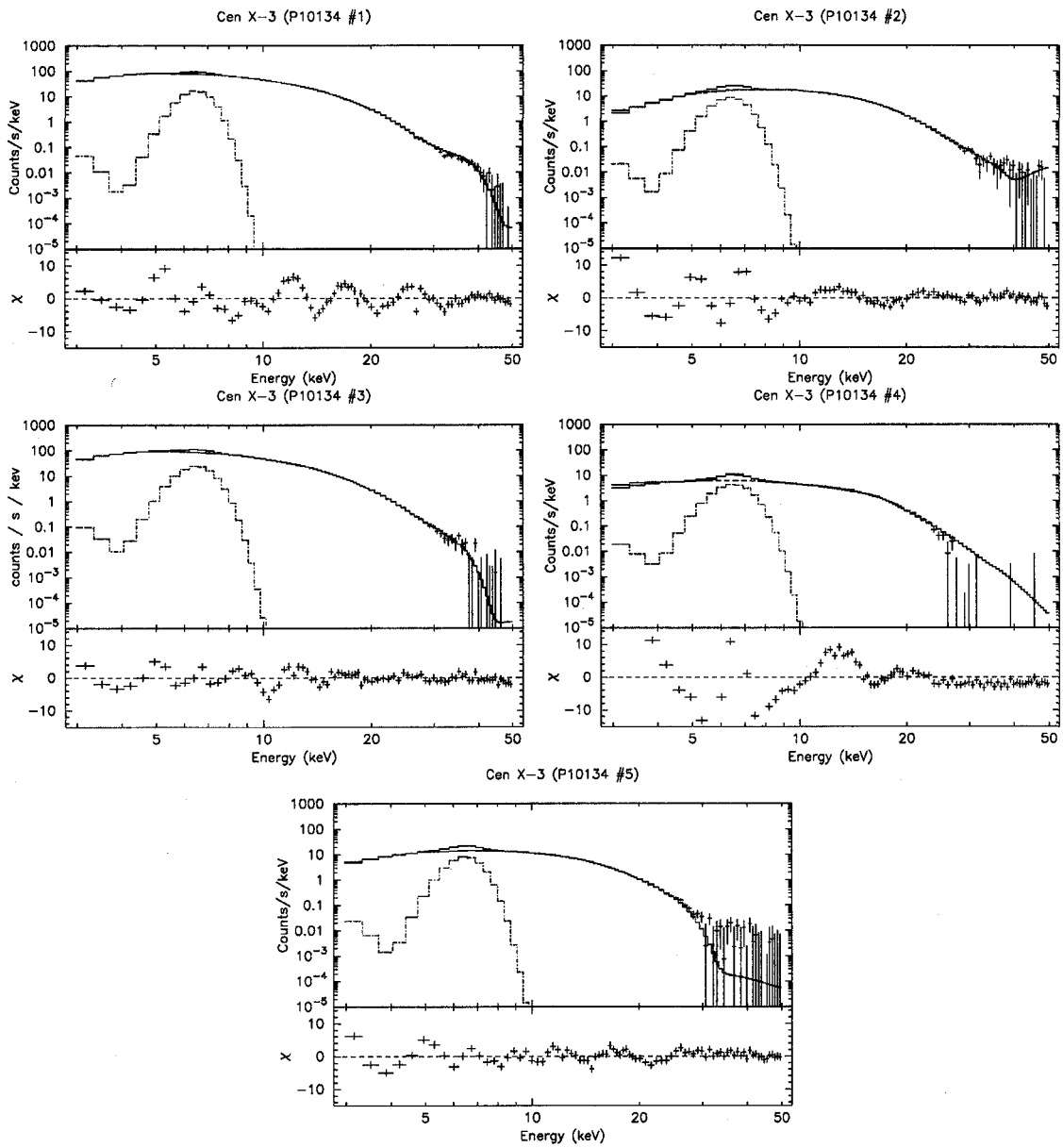

Figure 5.14: The PCA energy spectrum of each observation, #1, #2, #3, #4, and #5 (The # number is described as reference). These energy spectram were also obtained with $Standard-2$ mode. The upper two panels show #1 ($left$) and #2 ($right$). The middle two panels show #3 ($left$) and #4 ($right$). The bottom panel shows #5.

Table 5.9: The best fit parameters of the Cen X-3 spectrum (OBS ID = 10134)

	P10134 (B_16ms_64M_0_249)
N_H (10^{22} cm^{-2})	3.67±0.04
Photon Index	0.957±0.004
Normalization (photons cm^{-2} s^{-1} keV^{-1} at 1 keV)	0.158±0.001
E_{cut} (keV)	13.87±0.03
E_{fold} (keV)	12.9±0.3
First E_{cyc} (keV)	26.4±0.3
First $Depth_{cyc}$ [a]	1.01±0.08
First $Width_{cyc}$ (keV)	6.1±0.4
Second $Depth_{cyc}$ [a]	10±3
Second $Width_{cyc}$ (keV)	–
E_{Fe} (keV)	6.475±0.004
σ_{Fe} (keV)	0.378±0.006
I_{Fe} (photons cm^2 s^{-1})	(8.82±0.08)×10^{-3}
EW_{Fe} (eV)	386±3
Observed flux (ergs cm^{-2} s^{-1}) in 2-10 keV	2.2×10^{-9}
Observed flux (ergs cm^{-2} s^{-1}) in 2-50 keV	5.1×10^{-9}
Mean luminosity (erg s^{-1}) in 2-50 keV [b]	∼3.8×10^{37}
χ^2/D.O.F	878.6/72

[a] Optical depth at the cyclotron center energy.

[b] Assuming a distance of 8 kpc (cf. Krzeminski 1974; Day & Tennant 1991).

- P20104

  As seen in Figure 5.5, this observation covered almost whole two orbital cycle of Cen X-3. We excluded the data during the pre-eclipse dips and the eclipses. Figure 5.15 shows the phase averaged energy spectrum obtained in P20104 observation. The derived best fit parameters are summarized in Table 5.10. Here, we divided this observation into two segment, "seg1" and "seg2", based on the orbital cycle. Figure 5.16 shows the energy spectrum obtained from the seg1 and the seg2, and their derived best fit parameters are summarized in Table 5.10.

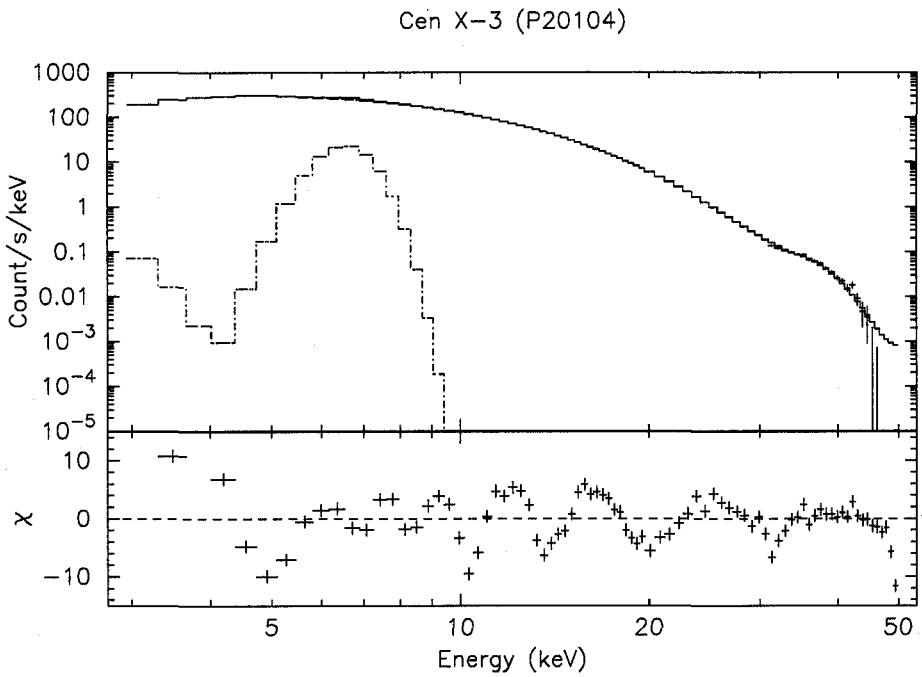

Figure 5.15: The phase averaged energy spectrum obtained by `Standard-2` mode of all orbital cycle of P20104 except for the pre-eclipsing dips and the eclipses.

Table 5.10: The best fit parameters of phase averaged energy spectrum obtained from all orbital cycle, the seg1, and the seg2 of P20104.

P20104 (B_16ms_16A_0_35_H)	all	seg1	seg2
Parameter		Value	
N_H (10^{22} cm^{-2})	2.13 ±0.01	2.19±0.01	2.08±0.02
Photon Index	1.245±0.001	1.270±0.002	1.219±0.003
Normalization (photons cm^{-2} s^{-1} keV^{-1} at 1 keV)	0.860±0.003	0.938±0.004	0.724±0.004
E_{cut} (keV)	13.30±0.04	13.36±0.04	13.28±0.04
E_{fold} (keV)	23.6±0.3	21.7±0.4	23.7±0.5
First E_{cyc} (keV)	26.4±0.3	26.2±0.2	26.1±0.3
First $Depth_{cyc}$ [a]	1.3±0.1	1.24±0.07	1.14±0.06
First $Width_{cyc}$ (keV)	10.7±0.1	10.1±0.3	10.0±0.5
Second $Depth_{cyc}$ [a]	10±3	9±3	8±2
Second $Width_{cyc}$ (keV)	9±1	10±3	14±3
E_{Fe} (keV)	6.547±0.003	6.546±0.003	6.537±0.004
σ_{Fe} (keV)	0.305±0.005	0.298±0.007	0.328±0.007
I_{Fe} (photons cm^2 s^{-1}) $\times 10^{-3}$	9.86±0.07	10.22±0.09	9.23±0.08
EW_{Fe} (eV)	128±1	119±1	129±1
Observed flux (ergs cm^{-2} s^{-1}) in 2-10 keV	6.3×10^{-9}	7.6×10^{-9}	6.0×10^{-9}
Observed flux (ergs cm^{-2} s^{-1}) in 2-50 keV	12.7×10^{-9}	14.3×10^{-9}	12.2×10^{-9}
Mean luminosity (erg s^{-1}) in 2-50 keV [b]	$\sim8.8\times10^{37}$	–	–
χ^2/D.O.F	1909.70/72	1490.74/72	1097.78/72

[a] Optical depth at the cyclotron center energy.

[b] Assuming a distance of 8 kpc (cf. Krzeminski 1974; Day & Tennant 1991).

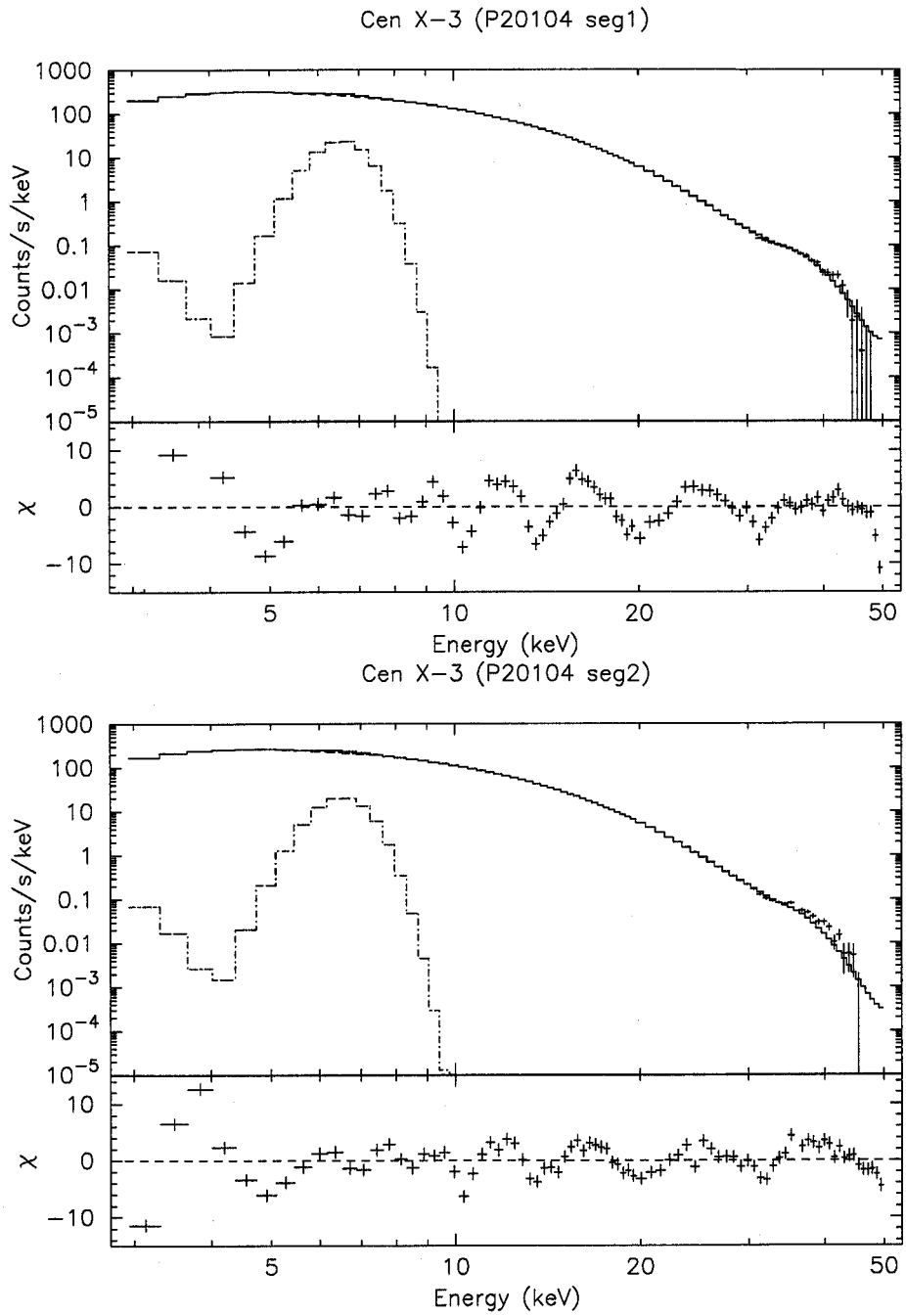

Figure 5.16: The upper panel and the lower panel show the phase averaged energy spectrum obtained in the seg1 and the seg2 of P20104, respectively. These energy spectrum dose not include the data of the pre-eclipsing dips and the eclipses.

- P30084

  We determined which data in this observation could be available for our analysis as follows.

  Considering to the orbital phase of this observation as described in Table 5.5, two observations of #7 (ϕ = 0.78–0.83) and #9 (ϕ = 0.70–0.73) possibly include the pre-eclipsing dip.

  In order to examine whether these two data included the pre-eclipsing dip or not, we analyzed the same way as we did for P10134. To compare the photo-electric absorption of the #2 (ϕ = 0.18–0.22), which did not include pre-eclipsing dip, with #7 and #9, we derived the photon index of $\alpha = 1.037$ from #2. Then, we fitted the energy spectrum of both #7 and #9 using the $\alpha = 1.037$, and derived $N_H = 4.32\pm0.03\times10^{22}$ cm^2 and $0.97\pm0.03\times10^{22}$ cm^2 respectively. The former #7, 4.32×10^{22} cm^2, was larger value than that of #2, $1.23\pm0.04\times10^{22}$ cm^2, and the similar value of P10134 observation. Considering the orbital phase of #7 (ϕ = 0.78–0.83) and the widely varied light curve of #7 as seen in Figure 5.6, we determined #7 included the pre-eclipsing dip. Thus we excluded #7 data from this work.

  Figure 5.17 shows the phase averaged energy spectrum obtained of P30084 without #7 observation. In addition, we divided this observation into two groups based on the observation mode of PCA. The observation modes of PCA during #1–#5 and #6–#10 were `B_4ms_16B_0_249_Q` and `B_4ms_16A_0_35_H` respectively. Figure 5.18 shows the energy spectrum of #1–#5 and #6–#10. The derived best fit parameters are summarized in Table 5.11.

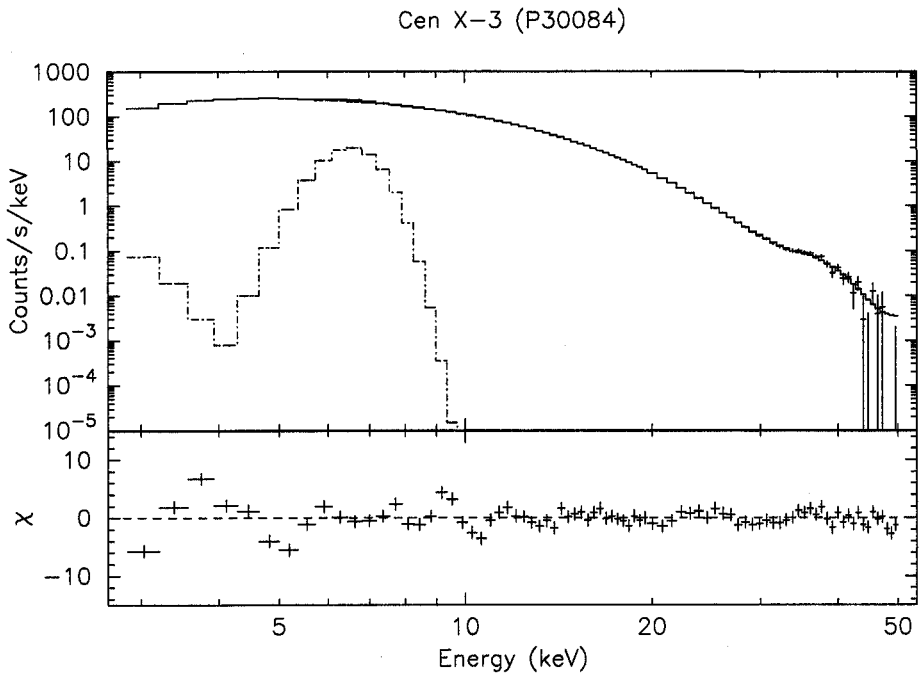

Figure 5.17: The phase averaged energy spectrum of **Standard-2** mode obtained in all data of P30084 except for #7.

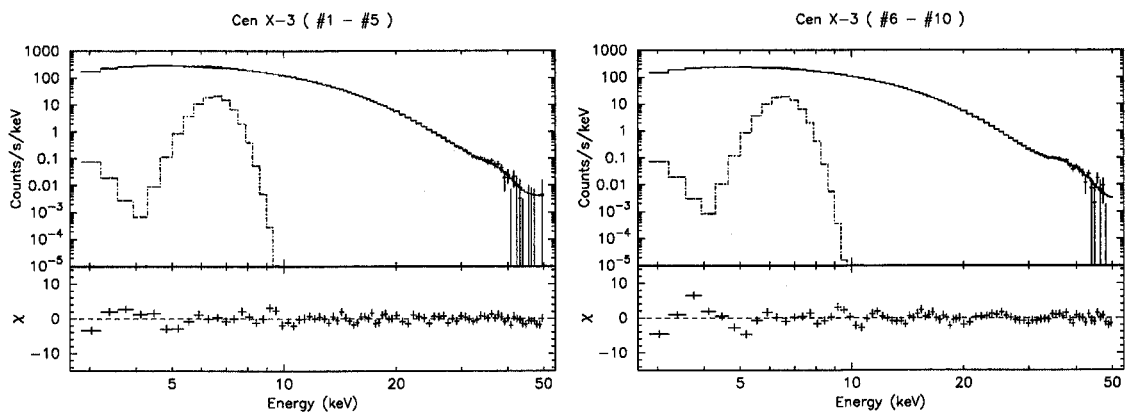

Figure 5.18: *Left*: The phase averaged energy spectrum obtained during #1–#5 of P30084. *Right*: The phase averaged energy spectrum obtained during #6–#10 of P30084 except for #7.

Table 5.11: The best fit parameters of phase averaged spectrum of all P30084 data

P30084	all	#1–#5	#6–#10*
Parameter		Value	
N_H (10^{22} cm^{-2})	1.75±0.02	1.95±0.03	1.343 ±0.03
Photon Index	1.150±0.004	1.173±0.004	1.101±0.006
Normalization (photons cm^{-2} s^{-1} keV^{-1} at 1 keV)	0.744±0.002	0.835±0.006	0.595±0.006
E_{cut} (keV)	13.0±0.07	13.1±0.1	12.9±0.1
E_{fold} (keV)	37±1	36±2	39±2
First E_{cyc} (keV)	25.4±0.4	24.9±0.7	26.7±0.2
First $Depth_{cyc}$ [a]	1.68±0.03	1.60±0.06	1.92±0.08
First $Width_{cyc}$ (keV)	14.2±0.3	14.2±0.4	14.3±0.4
Second $Depth_{cyc}$ [a]	13±6	–	–
Second $Width_{cyc}$ (keV)	5±5	–	–
E_{Fe} (keV)	6.546±0.004	6.537±0.006	6.562±0.009
σ_{Fe} (keV)	0.32±0.01	0.32±0.01	0.30±0.02
I_{Fe} (photons cm^2 s^{-1})×10^{-3}	9.85±0.07	10.61±0.01	8.66±0.02
EW_{Fe} (eV)	121±1	114±1	124±1
Observed flux (ergs cm^{-2} s^{-1}) in 2-10 keV	7.2×10^{-9}	7.8×10^{-9}	6.3×10^{-9}
Observed flux (ergs cm^{-2} s^{-1}) in 2-50 keV	13.5×10^{-9}	14.4×10^{-9}	12.1×10^{-9}
Mean luminosity (erg s^{-1}) in 2-50 keV [b]	∼5.9×10^{37}	–	–
χ^2/D.O.F	883.8182/72	549.62/72	435.79/72

* The #7 observation is not included in this analysis.

[a] Optical depth at the cyclotron center energy.

[b] Assuming a distance of 8 kpc (cf. Krzeminski 1974; Day & Tennant 1991).

- P40072

  In this observation, the orbital phase were determined ϕ = 0.67–0.82 and 0.16–0.27. Here, we examined whether the data obtained in the orbital phase, ϕ = 0.67–0.82, was available for our analysis or not, using the same way as we described previous analysis for P10134 and P30084.

  First, we derived the photon index, α of 1.05 $\pm$0.01 and the photo-electric absorption, N_H of 1.12$\pm$0.06$\times 10^{22}$ cm^2 from the energy spectrum in the orbital phase, ϕ, 0.16–0.27.

  Second, we fitted the energy spectrum in the orbital phase, ϕ = 0.67–0.82, using the same value of the photon index of ϕ = 0.16–0.27. As a result, the derived photo-electric absorption of ϕ = 0.67–0.82 was 0.37$\pm$0.02$\times 10^{22}$.

  Then, we concluded that the data in the orbital phase, ϕ = 0.67–0.82, did not include the pre-eclipsing dip. We applied all the data obtained in P40072. Figure 5.19 shows the phase averaged energy spectrum obtained in P40072. The derived best fit parameters are summarized in Table 5.12.

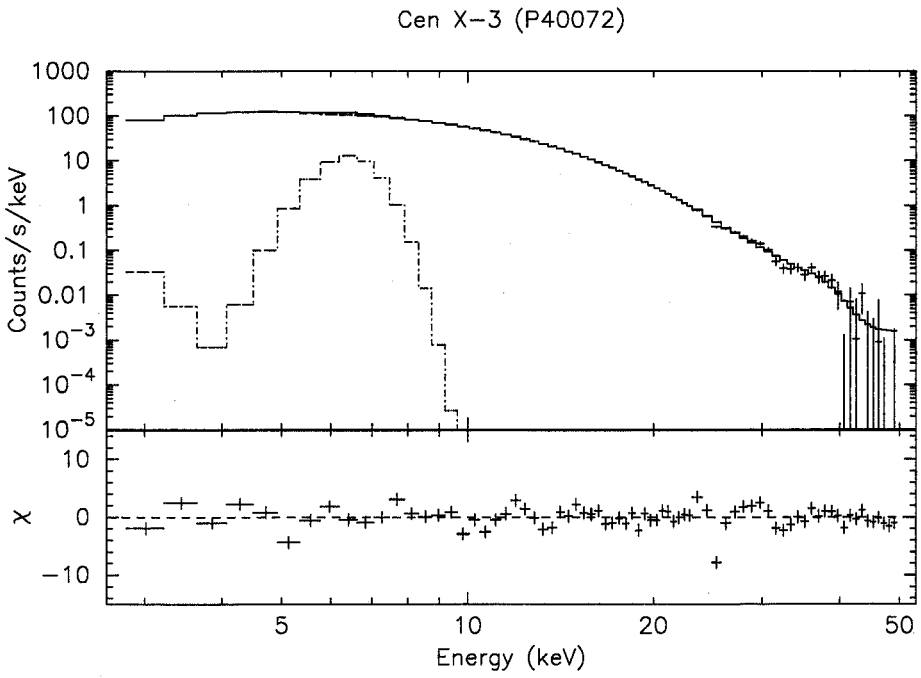

Figure 5.19: The phase averaged energy spectrum of `Standard-2` mode obtained in all the data of P40072.

Table 5.12: The best fit parameters of phase averaged spectrum of all P40072 data

	P40072 (GoodXenon)
N_H (10^{22} cm^{-2})	0.8675±0.0084
Photon Index	1.018±0.001
Normalization (photons cm^{-2} s^{-1} keV^{-1} at 1 keV)	0.5603±0.0003
E_{cut} (keV)	13.14±0.03
E_{fold} (keV)	25.0±0.2
First E_{cyc} (keV)	24.18±0.03
First $Depth_{cyc}$ [a]	1.135±0.004
First $Width_{cyc}$ (keV)	10.90±0.06
Second $Depth_{cyc}$ [a]	1.96±0.01
Second $Width_{cyc}$ (keV)	–
E_{Fe} (keV)	6.429±0.004
σ_{Fe} (keV)	0.349±0.009
I_{Fe} (photons cm^2 s^{-1})	(13.10±0.01)×10^{-3}
EW_{Fe} (eV)	152±2
Observed flux (ergs cm^{-2} s^{-1}) in 2-10 keV	6.7×10^{-9}
Observed flux (ergs cm^{-2} s^{-1}) in 2-50 keV	13.6×10^{-9}
Mean luminosity (erg s^{-1}) in 2-50 keV [b]	∼9.9×10^{37}
χ^2/D.O.F	486.36/63

[a] Optical depth at the cyclotron center energy.

[b] Assuming a distance of 8 kpc (cf. Krzeminski 1974; Day & Tennant 1991).

5.3.3 Summary of Spectral Fitting Results

Consequently, we have analyzed energy spectrum obtained with `Standard-2` mode of five data sets, two in P20104, two in P30084, and P40072. The equivalent widthes of iron lines and their central energies are ranging from 114 eV to 152 eV and from 6.413 keV to 6.54 keV, respectively. These values are consistent to the previous works. These results imply that the iron ions are not highly ionized one. The flux of our five data sets are ranging from 2.9×10^{-9} to 7.6×10^{-9} ergs cm^{-2} s^{-1} in 2–10 keV, and these correspond to the luminosity from 1.5 to 5.4 erg s^{-1} in 2–10 keV. We also analyze P10134, which may include the pre-eclipse dips with the same way. Comparing P10134 to others will also help to check the state of Cen X-3 whether the data includes the unstable state such pre-eclipsing dips or not, and to decide the data is available for our analysis or not.

5.4 Cross Spectral Analysis

As we reviewed in chapter 2, the iron emission line has been thought to be fluorescent lines in origin and to be emitted by the matter around the neutron star. Then, we expect that the time variation of light curves containing the iron K lines delays from those of the other continuum X-rays and the delay time is corresponding to the difference of the light pass beteen the neutron star and the emitting region of the iron lines, assuming that the fluorescent iron lines are reprocessed in the circumstellar matter by the continuum X-ray from the neutron star.

Figure 5.20 is an example of a detailed light curve, which displays the aperiodic time variation along with the coherent pulses. We are attempting to analyze the aperiodic time variation rather than the coherent pulsations. The best method to use is the cross spectral analysis, since the cross spectra make it possible to distinguish the pulse component from the interesting aperiodic component. The method of cross spectral analysis was introduced for the investigation of the short term variation of low mass X-ray binaries by van der Klis et al. (1987) and has also been applied to black hole candidates (Miyamoto et al. 1988; see also appendix A.3 in this thesis).

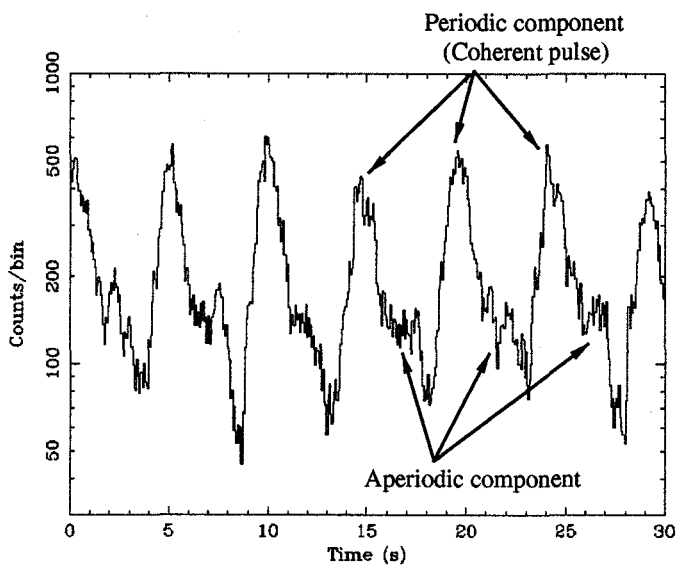

Figure 5.20: An example of a detailed light curve obtained from the data of P20104 observation. The time resolution is 64 ms bins in the energy range of 3.3–13.1 keV. Aperiodic time variation can be seen as well as the coherent pulses.

5.5 Analysis

Here, we will show the calculated coherence and phase lag using the cross spectral analysis for each observation.

5.5.1 P10134

As mentioned previous section 5.1, this observation was carried out with the binned mode, `B_16ms_64M_0_249`, with the time resolution of 16 ms and 64 spectral channels rebinned from the original channels 0–249 corresponding the energy range from 0.1 keV to 101.0 keV. We excluded the observed data in clear pre-eclipsing dips, and used data only both #1 and #3 observed data. This data may include pre-eclipsing dips.

At first, we extracted the light curves in seven energy bands (1.9–4.4, 4.4–5.8, 5.8–7.3, 7.3–8.7, 8.7–12.3, 12.3–17.1, 17.1–31.0 keV). This energy boundaries were determined as having a roughly equal count-rate each other. From the fitting result of the energy spectrum derived from `Standard-2` mode, the equivalent width of the iron K lines is ∼328 eV, the contribution of iron line photons to the energy band from 5.8 keV to 7.3 keV is estimated to be ∼22%. We refer to this energy range as the "iron-band".

We calculated the cross spectra between the X-ray light curve in the iron-band and the other energy bands, and studied the coherence and the phase lag between them. The data were divided into 571 segments, each with a 64 s exposure. The complex Fourier transforms for each of the two energy bands in each data sets were computed using the Fast Fourier Transform (FFT) technique. These complex Fourier components were averaged over the 571 segments. The relative phase and coherence were calculated from these averaged complex Fourier components. Finally, we averaged again these calculated phase lags and coherences within a certain frequency range. For the error estimation, we referred to Bendat and Piersol (1971).

Figure 5.21 shows the calculated phase lag of time variations in the six energy bands from that of iron-band as a function of the frequency. The scattered component below 1 Hz is due to the pulsed component, the shape of which is different according to the energy. A prominent structure at around 1.4 Hz may be another phenomenon and we do not discuss on this structure in this thesis. Figure 5.22 shows the coherence calculated between the iron-band and the other X-ray bands as a function of the frequency. Below 1 Hz, the coherences are above 0.55, and significant coherence can be clearly seen up to ∼20 Hz.

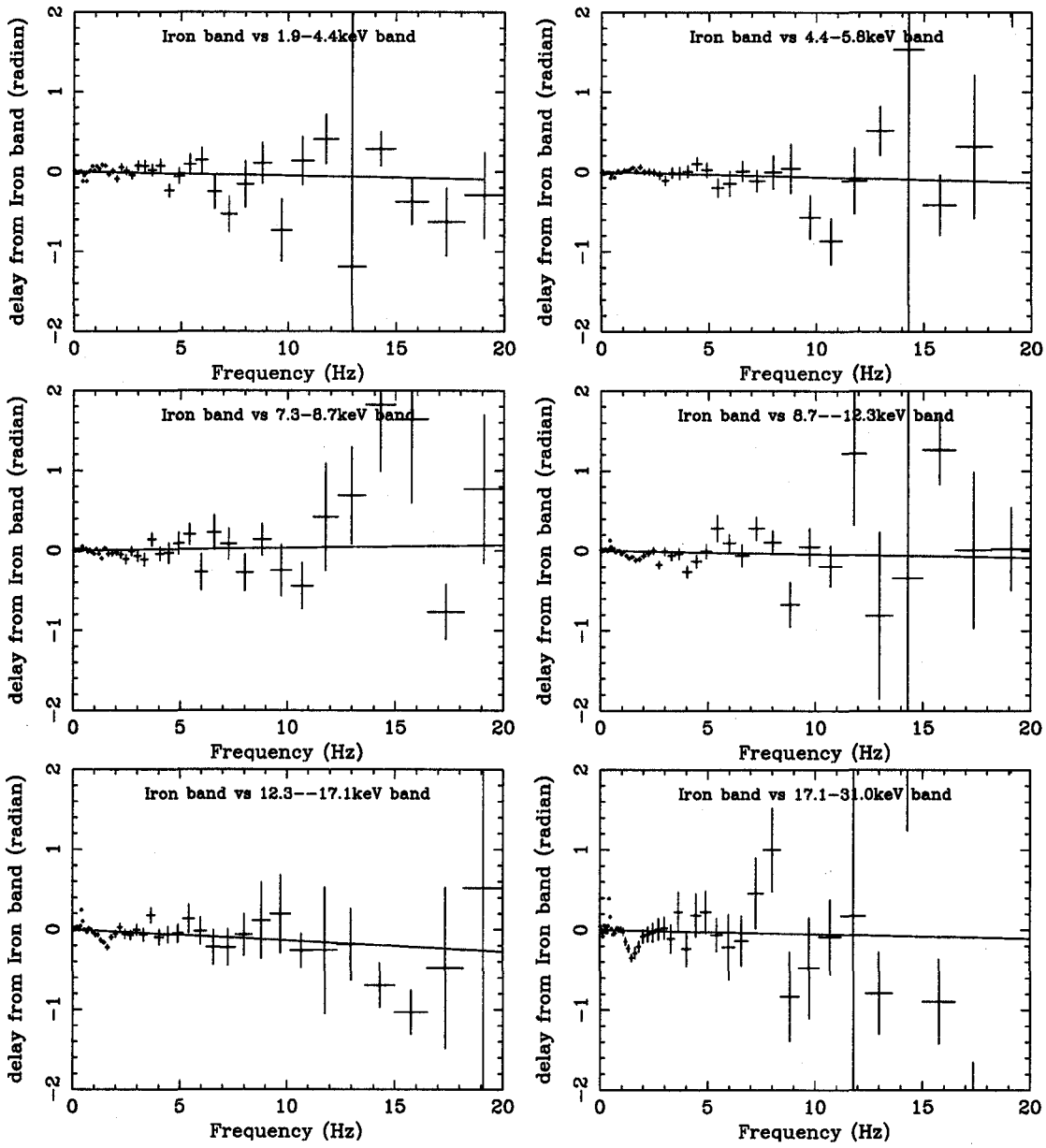

Figure 5.21: Phase lags calculated between the iron-band and the other X-ray bands in P10134 are plotted as a function of frequency. The best fit linear function with no offset is also plotted.

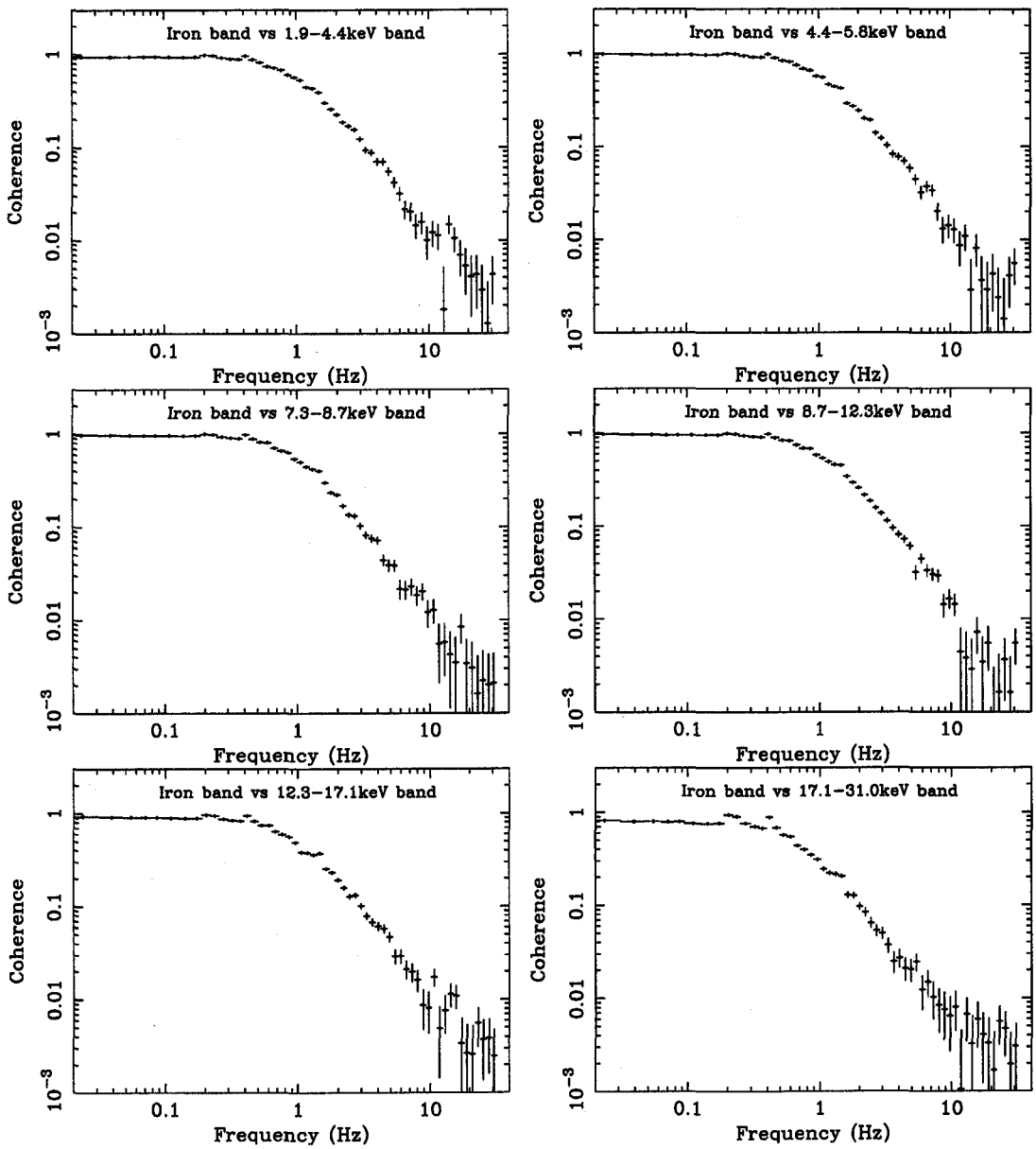

Figure 5.22: Coherences calculated between the iron-band and the other X-ray bands in P10134 are plotted as a function of frequency.

5.5.2 P20104, P30084, and P40072

We also applied the cross spectral analysis for the other data of P20104, P30084, and P40072. When we calculated the cross spectra between the iron-band and the other energy bands, we divided each of the two energy bands into 502 segments with 64 s exposure time for P20104, and 502 segments with 64 s exposure time for P30084, and 252 segments with 64 s exposure for P40072.

The other detailed information for the cross spectral analysis of each observation are summarized in Table 5.13.

Table 5.13: The detailed information for the cross spectral analysis of each observation.

P10134	
PCA Mode	B_16ms_64M_0_249
Binned time resolution of LC (ms)	15.625
Energy bands of each LC	7 energy bands (1.9–4.4, 4.4–5.8, 5.8–7.3[§], 7.3–8.7, 8.7–12.3, 12.3–17.1, 17.1–31.0 keV)
EW_{Fe} (eV)	328±1
Fraction of iron-photon in the iron-band	~22%
Phase lags (Coherences)	Figure 5.21 (Figure 5.22)
P20014 (all, seg1, seg2)	
PCA Mode	B_16ms_16A_0_35_H
EW_{Fe} (eV)	128±1[*], 119±1[†], 129±1[‡]
Binned time resolution of LC (ms)	15.625
Energy bands of each LC	6 energy bands (3.3–4.7, 4.7–5.8, 5.8–7.2[§], 7.2–8.7, 8.7–10.9, 10.9–13.1 keV)
iron-photon in the iron-band	~9%[¶]
Phase lags (Coherences)	Figure 5.23[a], Figure 5.25[b], Figure 5.27[c] (Figure 5.24[a], Figure 5.26[b], Figure 5.28[c])
P30084	
PCA Mode	B_4ms_16B_0_249_Q
Binned time resolution of LC (ms)	15.625
Energy bands of each LC	8 energy bands (0.0–3.5, 3.5–6.1, 6.1–7.2[§], 7.2–8.2, 8.2–10.4, 10.4–13.0, 13.0–18.2, 18.2–34.1 keV)
EW_{Fe} (eV)	114±1
Fraction of iron-photon in the iron-band	~11%
Phase lags (Coherences)	Figure 5.29 (Figure 5.30)
PCA Mode	B_4ms_16A_0_35_H
Binned time resolution of LC (ms)	15.625
Energy bands of each LC	7 energy bands (3.3–4.7, 4.7–5.8, 5.8–7.2[§], 7.2–8.0, 8.0–9.4, 9.4–10.9, 10.9–13.1 keV)
EW_{Fe} (eV)	124±1
Fraction of iron-photon in the iron-band	~9%
Phase lags (Coherences)	Figure 5.31 (Figure 5.32)
P40072	
PCA Mode	GoodXenon
Binned time resolution of LC (ms)	15.625
Energy bands of each LC	6 energy bands (1.5-4.1, 4.1-5.8, 5.8-7.5[§], 7.5-9.6, 9.6-15.2, 15.2-26.2 keV)
EW_{Fe} (eV)	152±2
Fraction of iron-photon in the iron-band	~9%
Phase lags (Coherences)	Figure 5.33 (Figure 5.34)

[§] This energy band is the iron-band.

[*], [†], [‡] The data of all data, seg1 and seg2 of P20104 observation respectively.

[¶] All the data of P20104 (all, seg1, seg2) have a same fraction of iron photon of ~9%.

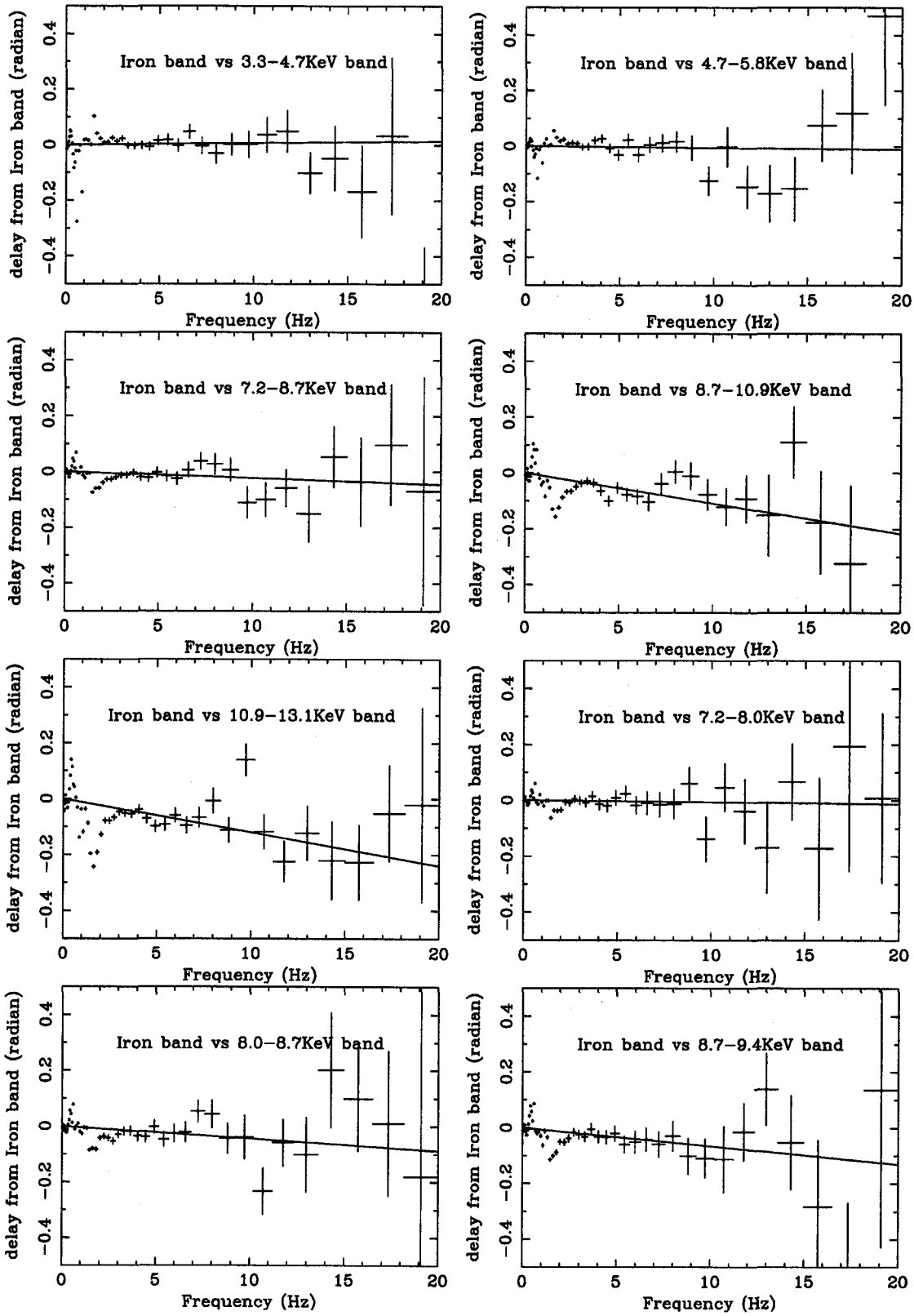

Figure 5.23: Phase lags calculated between the iron-band and the other X-ray bands in P20104 are plotted as a function frequency. The best fit linear function with no offset is also plotted.

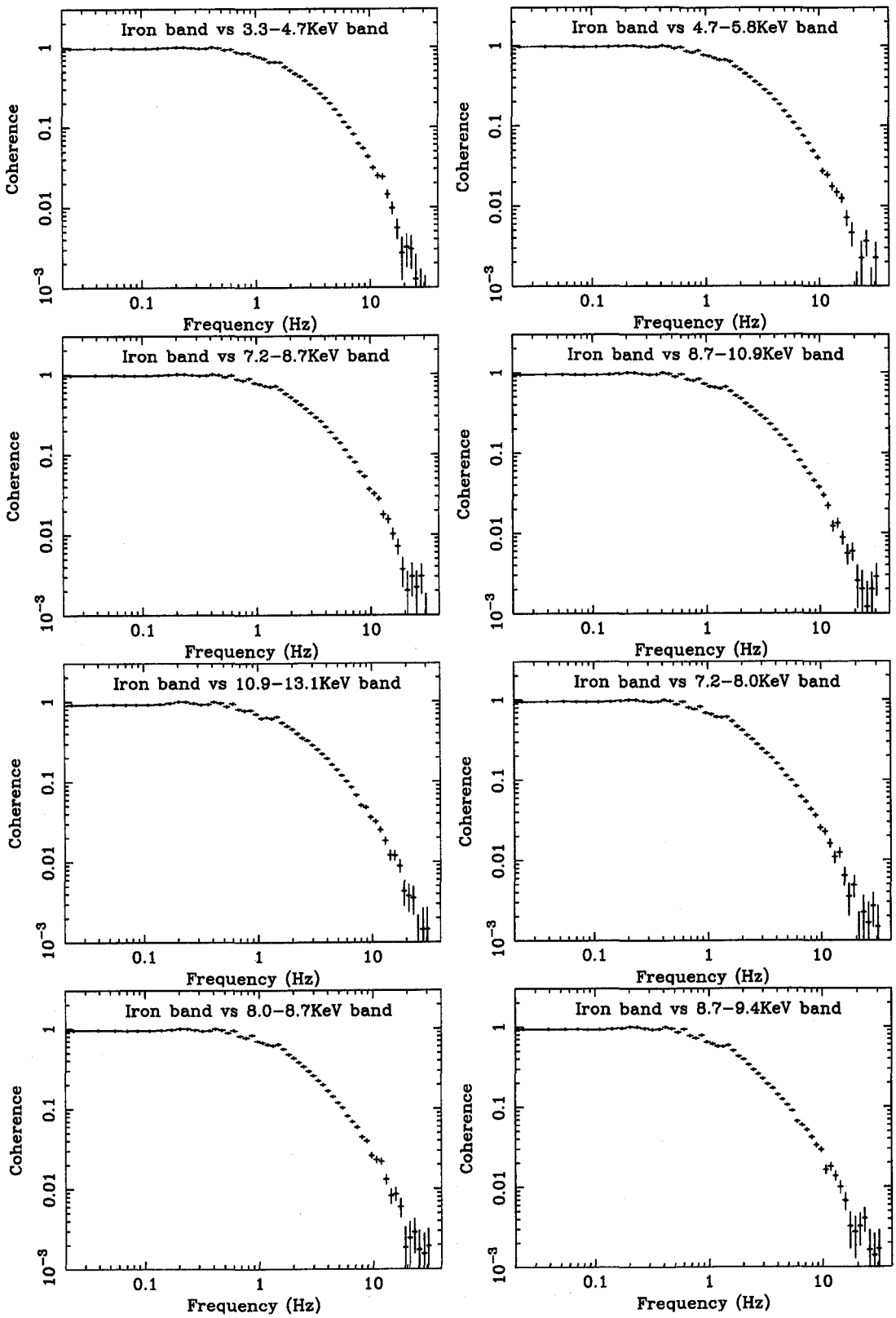

Figure 5.24: Coherences calculated between the iron-band and the other X-ray bands in P20104 is plotted as a function frequency.

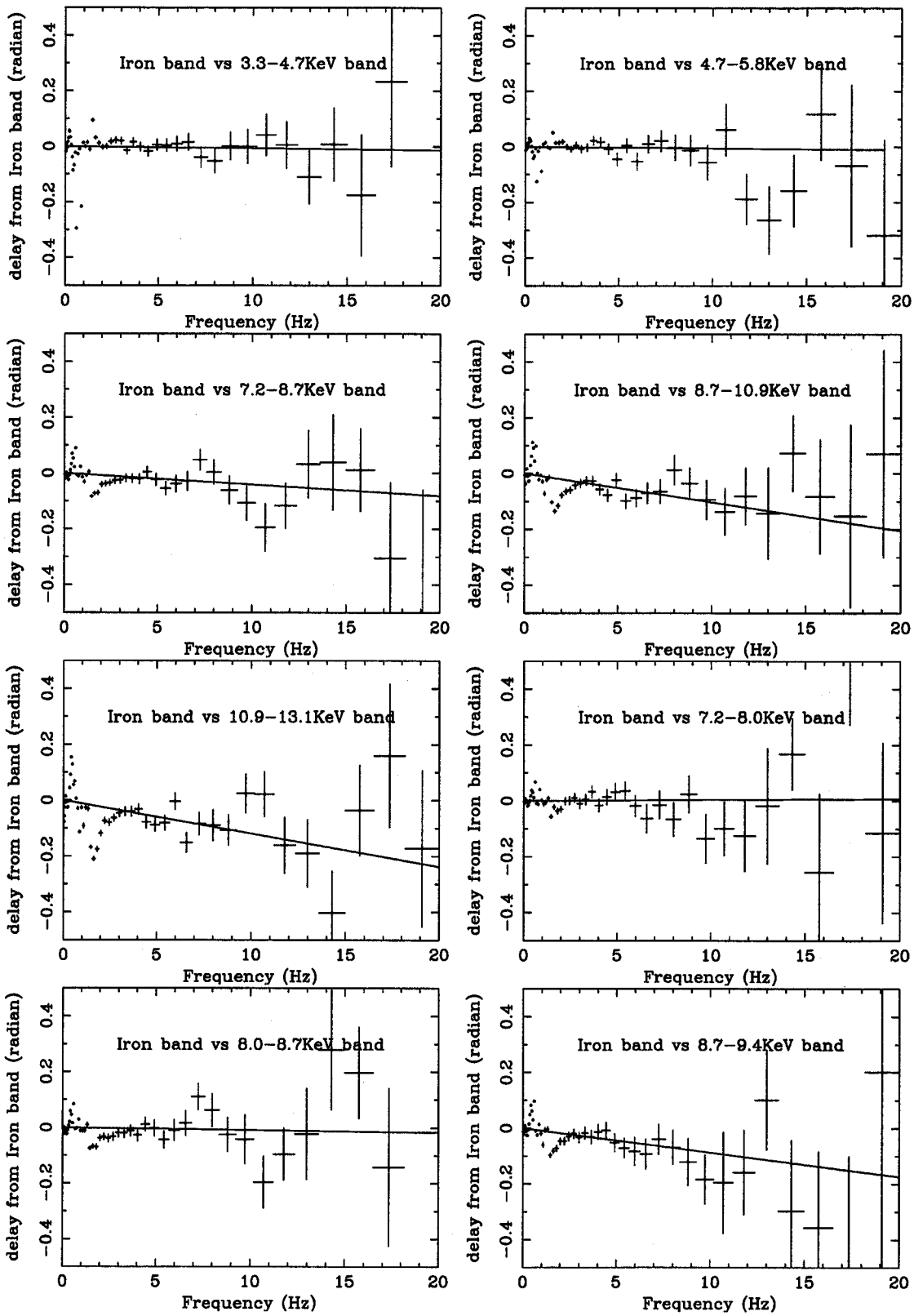

Figure 5.25: Phase lags calculated between the iron-band and the other X-ray bands in seg1 of P20104 are plotted as a function frequency. The best fit linear function with no offset is also plotted.

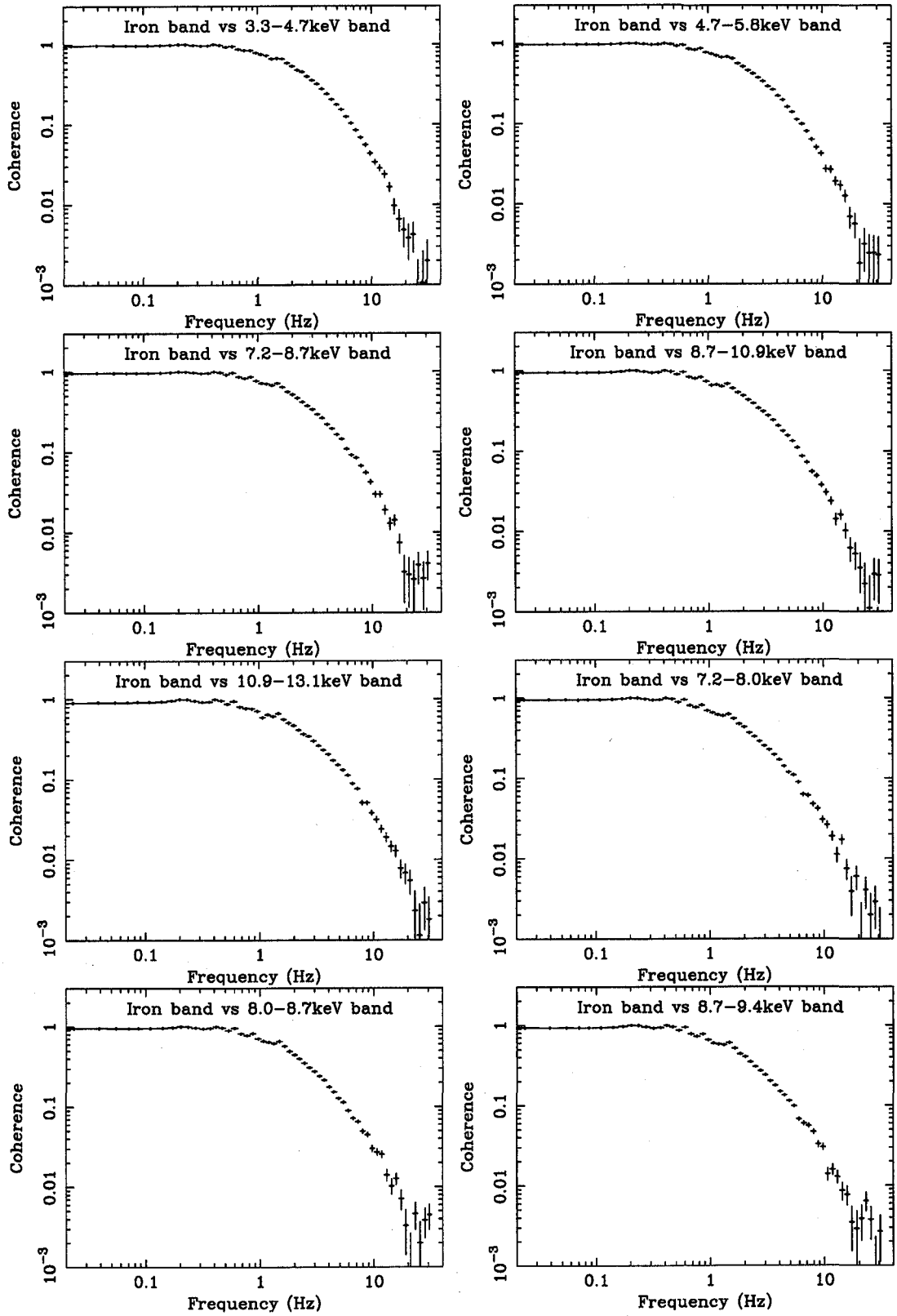

Figure 5.26: Coherences calculated between the iron-band and the other X-ray bands in seg1 of P20104 are plotted as a function frequency.

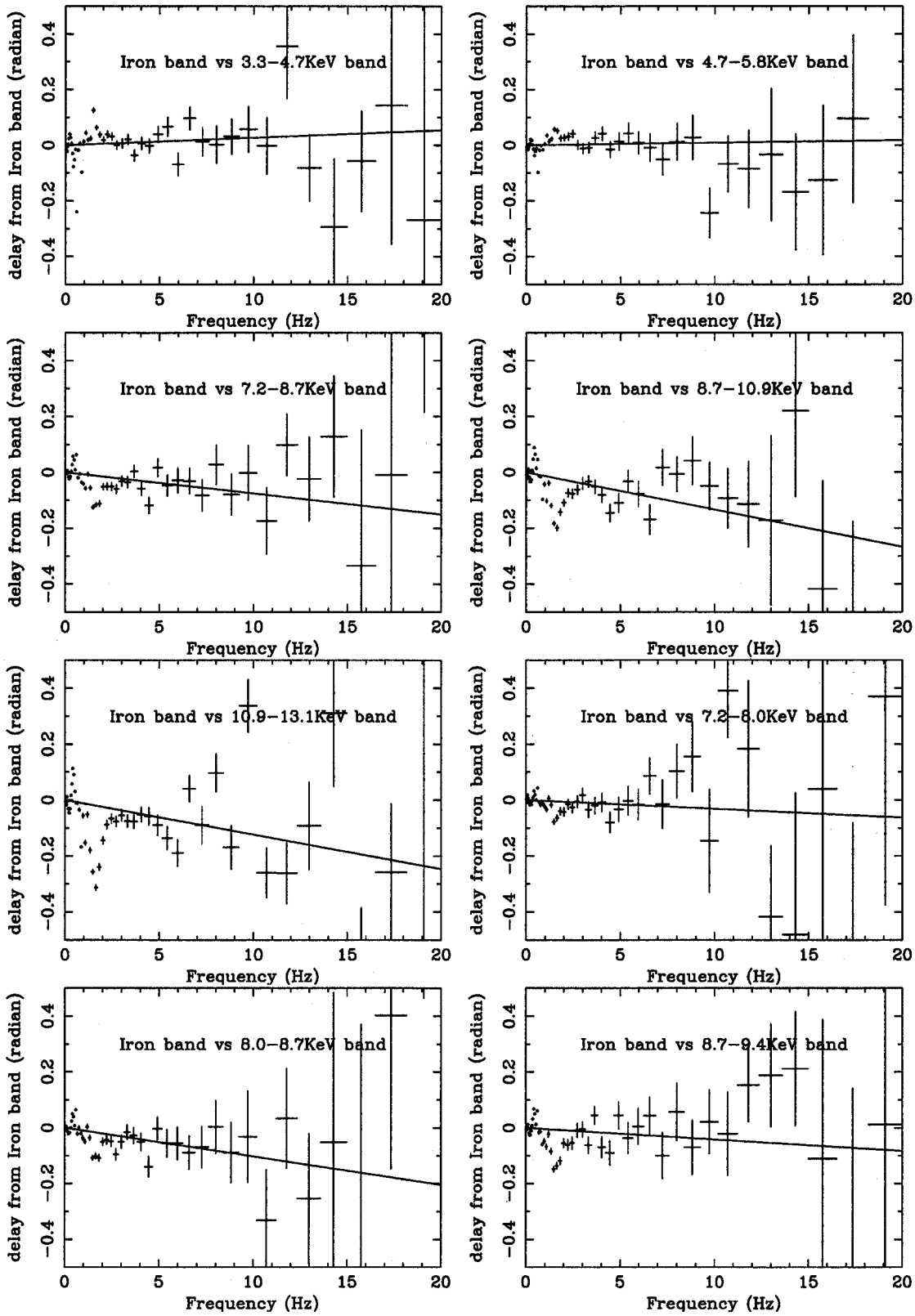

Figure 5.27: Phase lags calculated between the iron-band and the other X-ray bands in seg2 of P20104 are plotted as a function frequency. The best fit linear function with no offset is also plotted.

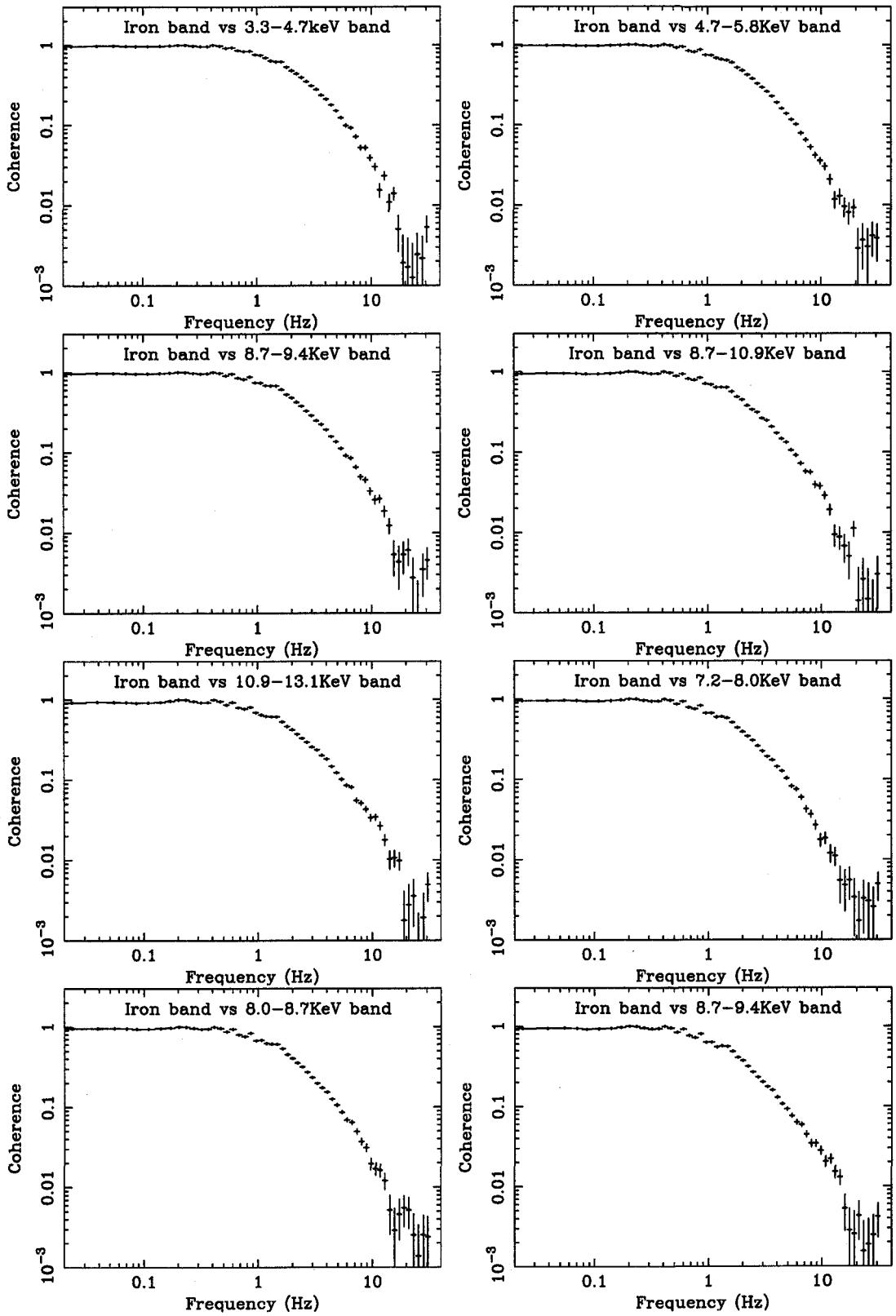

Figure 5.28: Coherences calculated between the iron-band and the other X-ray bands in seg2 of P20104 are plotted as a function frequency.

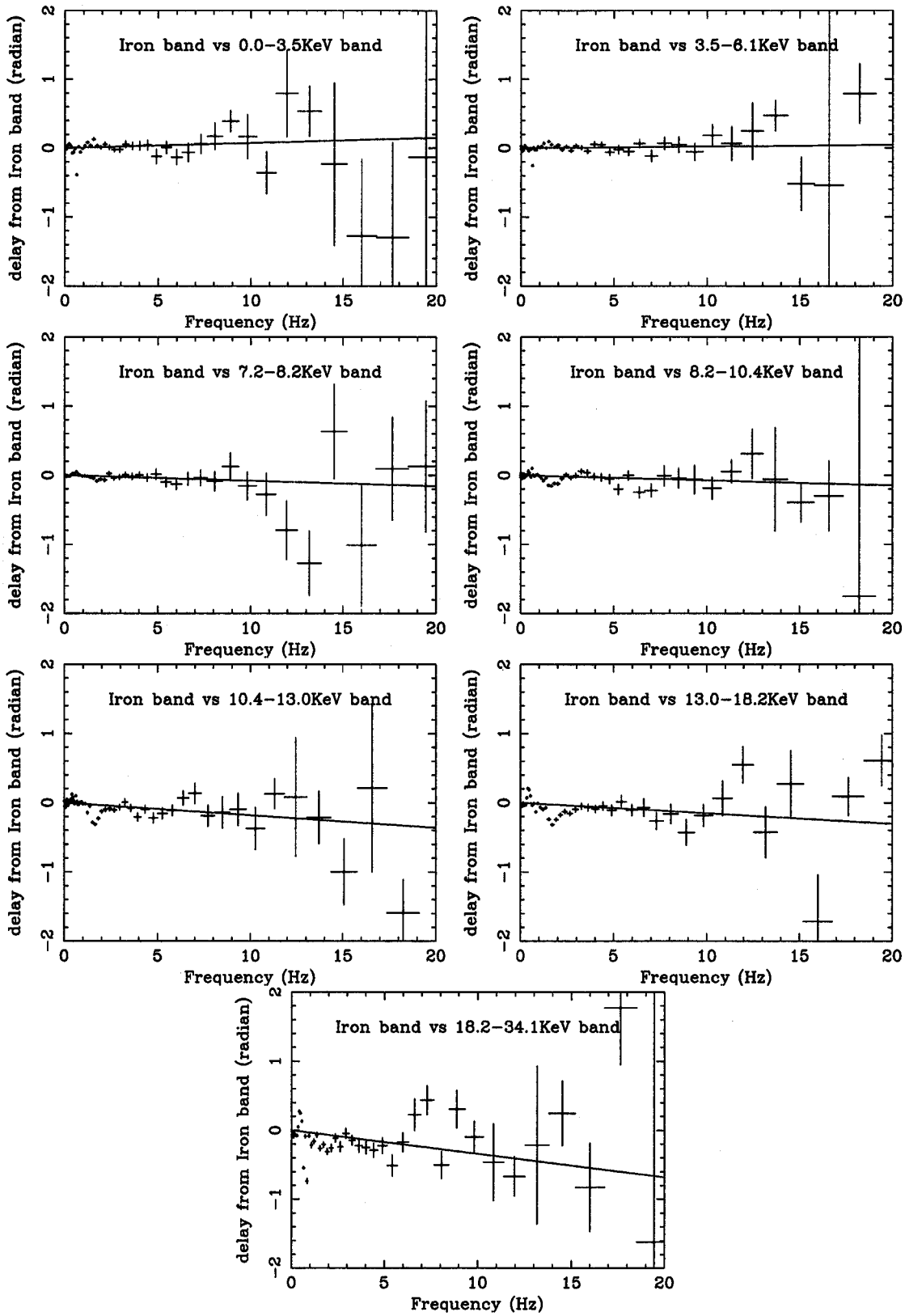

Figure 5.29: Phase lags calculated between the iron-band and the other X-ray bands obtained `B_4ms_16B_0_249_Q` mode in P30084 are plotted as a function frequency. The best fit linear function with no offset is also plotted.

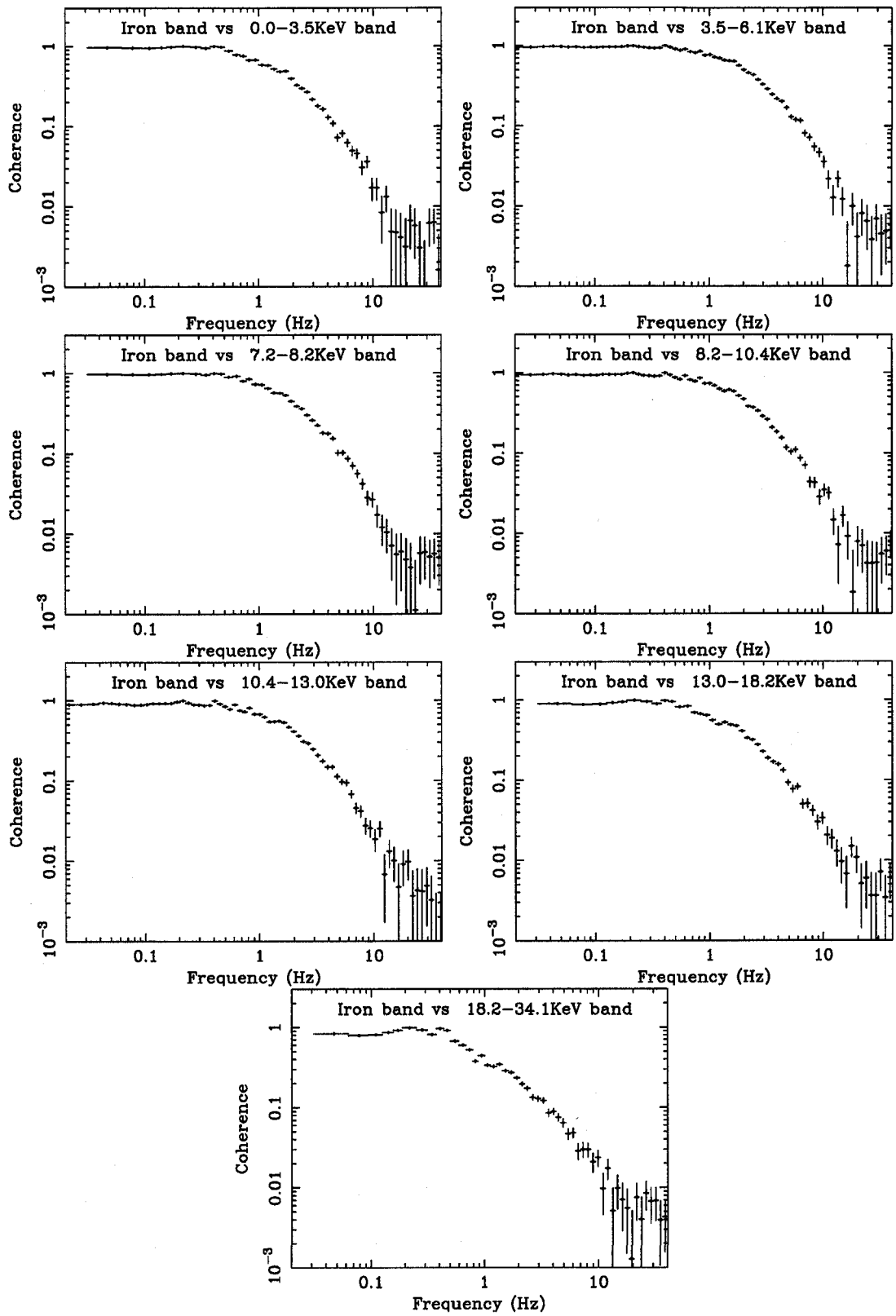

Figure 5.30: The coherence calculated between the iron-band and the other X-ray bands obtained `B_4ms_16B_0_249_Q` mode in P30084 are plotted as a function frequency.

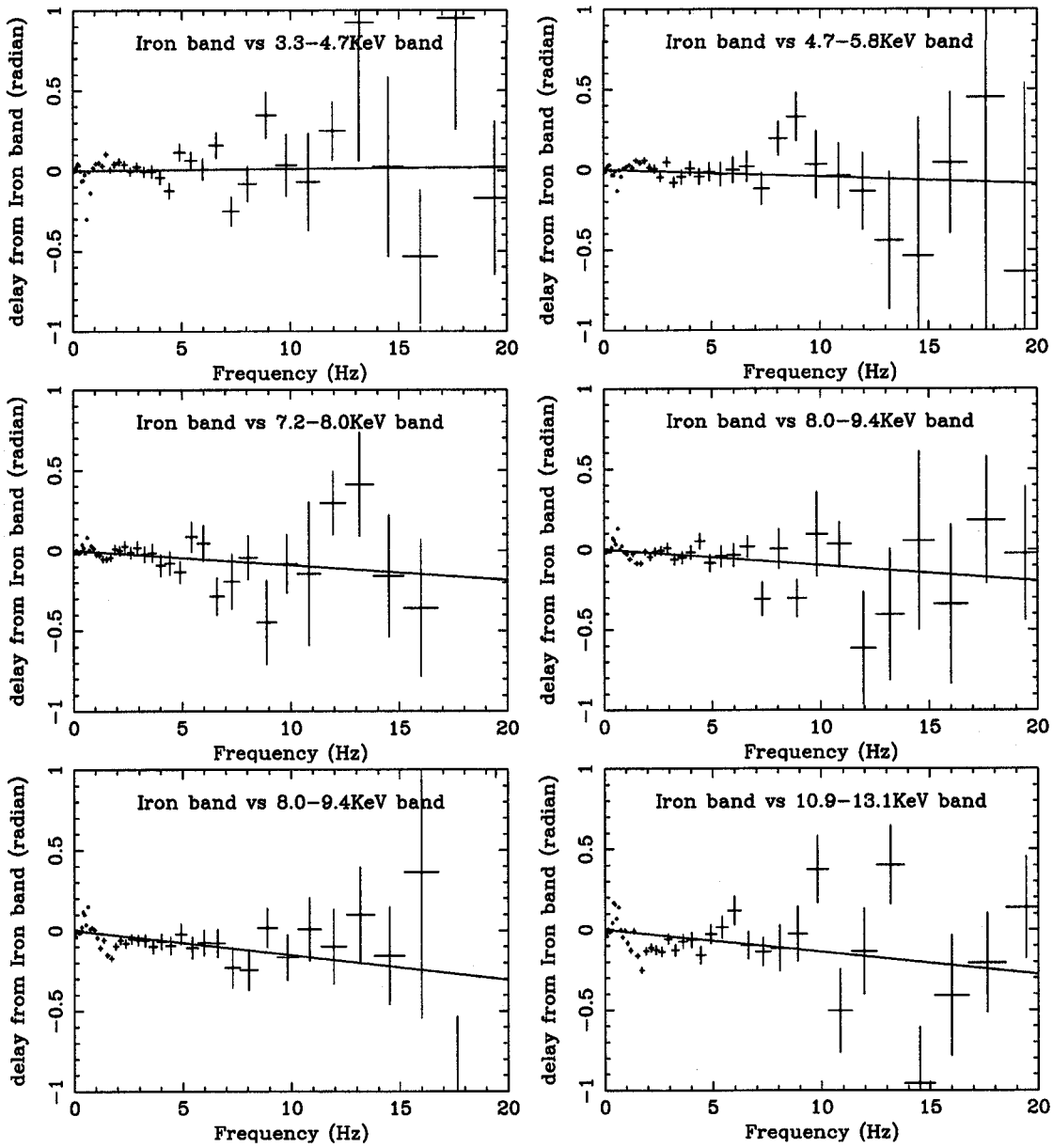

Figure 5.31: Phase lags calculated between the iron-band and the other X-ray bands obtained B_16ms_16A_0_35_H mode in P30084 are plotted as a function frequency. The best fit linear function with no offset is also plotted.

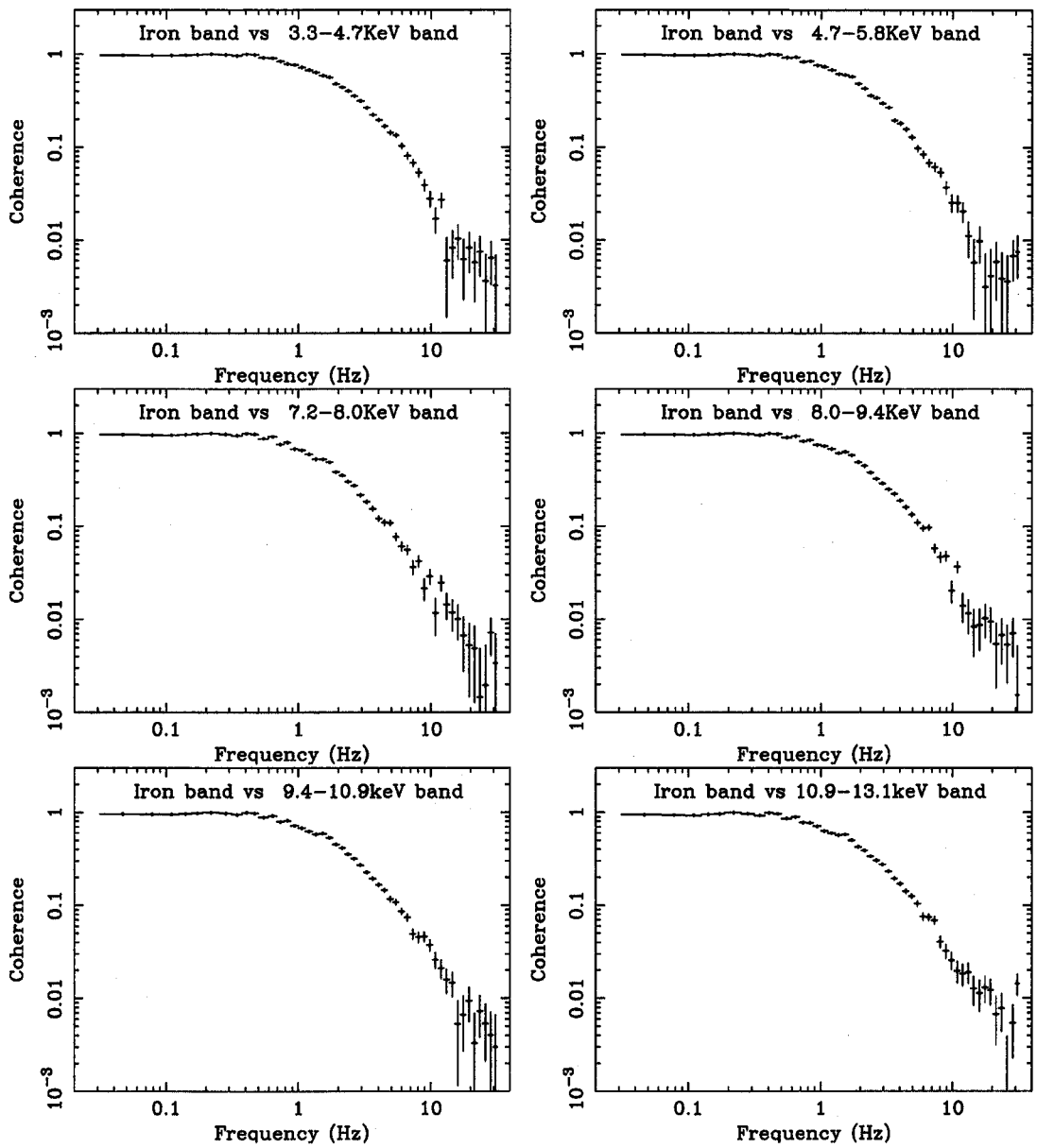

Figure 5.32: The coherence calculated between the iron-band and the other X-ray bands obtained `B_16ms_16A_0_35_H` mode in P30084 are plotted as a function frequency.

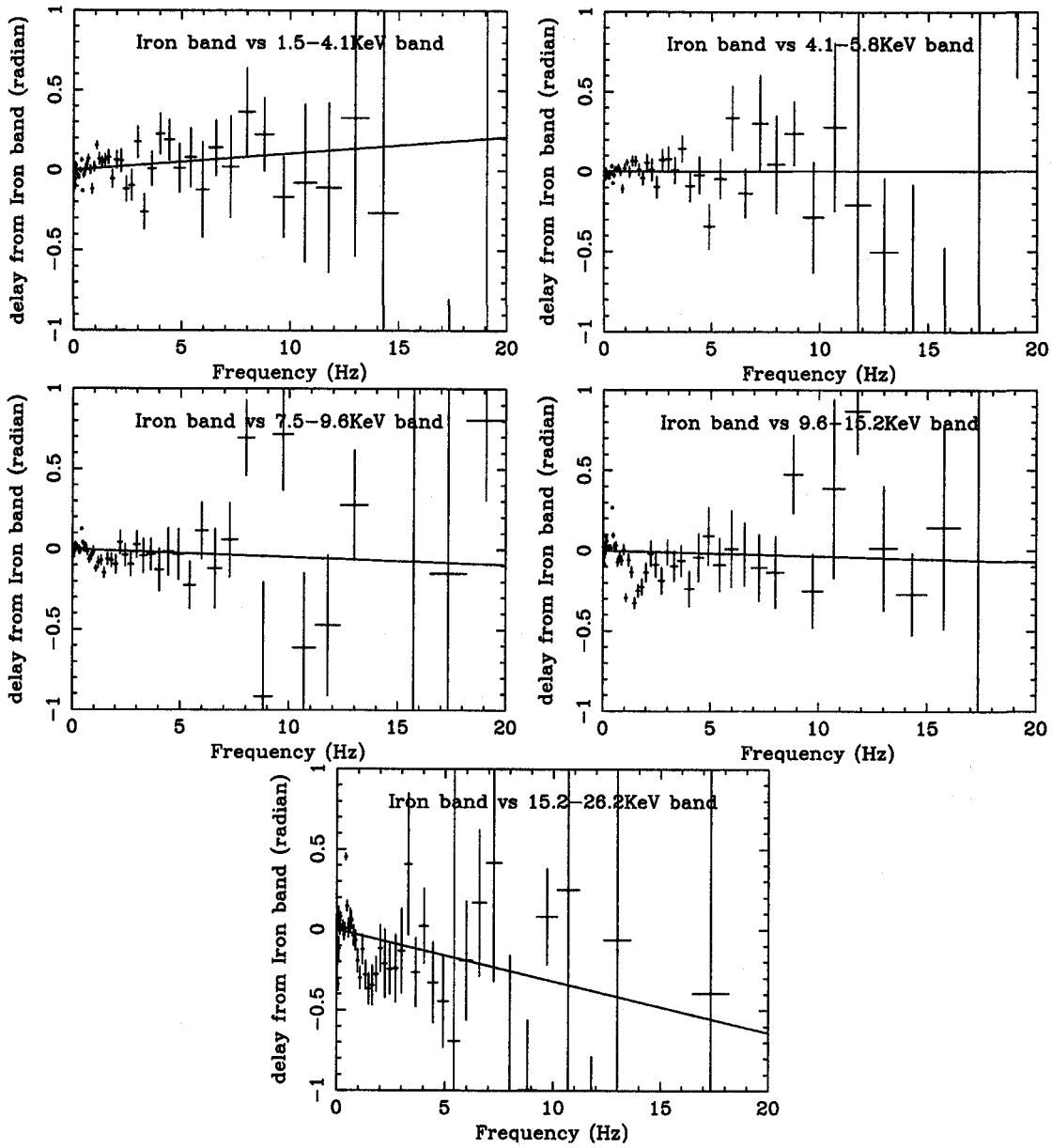

Figure 5.33: Phase lags calculated between the iron-band and the other X-ray bands in P40072 are plotted as a function frequency. The best fit linear function with no offset is also plotted.

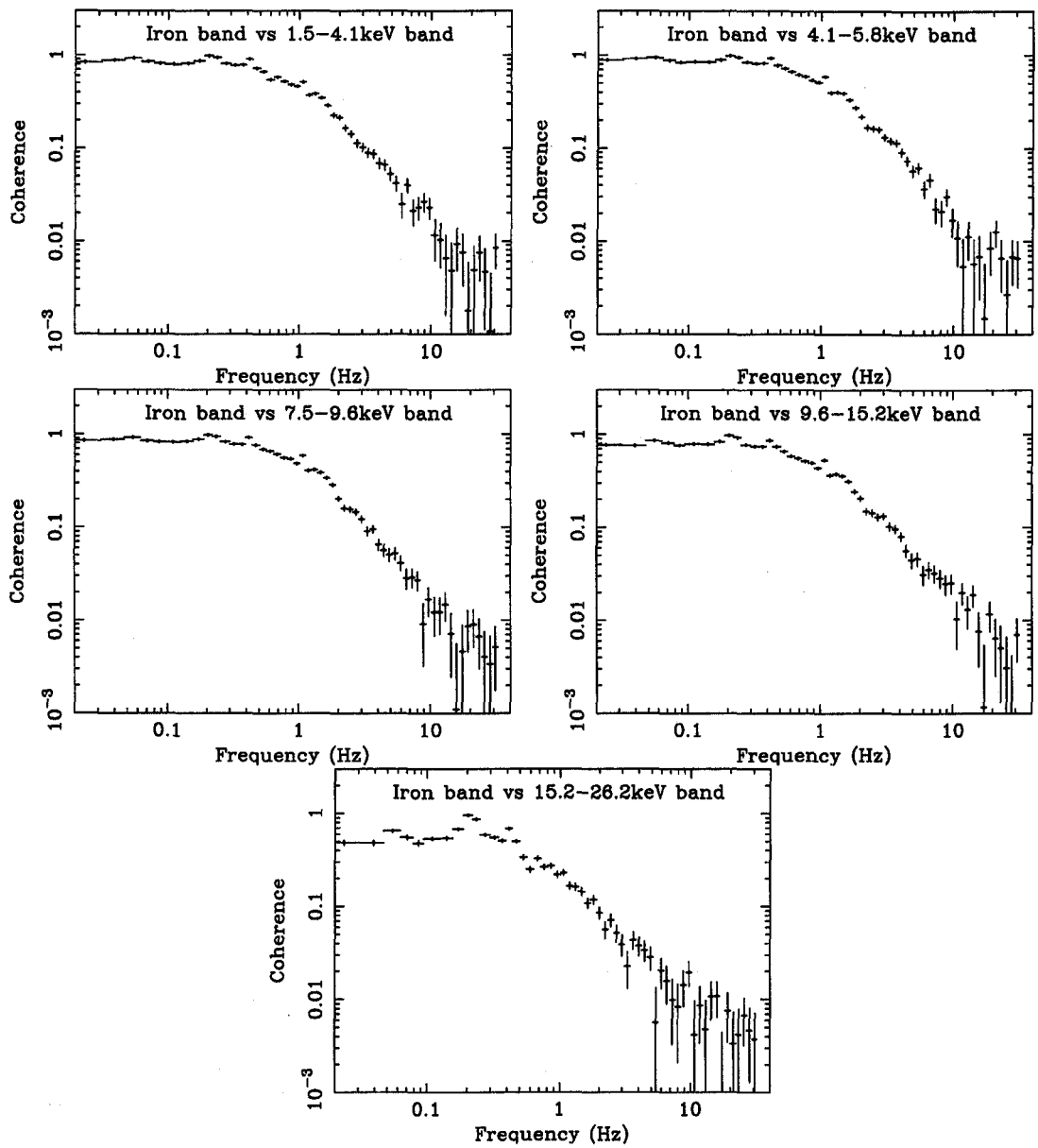

Figure 5.34: Coherences calculated between the iron-band and the other X-ray bands in P40072 are plotted as a function frequency.

5.6 Result of Cross Spectral Analysis

In the previous section, we have calculated the cross spectrum of Cen X-3 to investigate the delay time of the variavility of the iron-band with respect to the other continuum X-ray band. Here, we will summarize these results, focusing on the result of P20104.

5.6.1 P20104

If there is a constant time delay which is independent on frequency, the phase lag must be a linear function of the frequency with no offset. As shown in Figure 5.25, we first fitted the data of phase lag between 3 Hz and 15 Hz with linear function with no offset, where the coherence is high enough and the effect of the coherent pulse is small. Then, we found that the time variation in the higher energy band was advanced relative to that of the iron-band and the phase lag between the iron-band and the lower energy bands were relatively small. We plotted these results as a function of the energy in Figure 5.35.

We discovered, for the first time, that the higher energy band was advanced, with exception of the iron-band. We also derived the delays using more finely binned energy band data just above the iron-band (7.2–8.0, 8.0–8.7, and 8.7–9.4 keV). Derived delays are indicated by circles in Figure 5.35. The data in the energy range from 5.8 keV to 8.0 keV shows time delay from the general trend of the energy dependence. A linear function was fitted to the time delay data from the original six energy bands. The best fit linear function is

$$D(E) = -(2.6 \pm 0.4) \times 10^{-4} E(\mathrm{keV}) + (1.3 \pm 0.4) \times 10^{-3}(\mathrm{s}), \tag{5.5}$$

where $D(E)$ is the delay time as compared to the "iron band" as a function of energy, and E is the energy.

We discovered that the iron-band data at 6.5 keV was delayed from this best-fit model with (0.39±0.10) ms, where the error was the one sigma confidence level. In other words, we could detect the delayed iron line component at nearly the four sigma confidence level. The 7.2–8.0 keV band also shows the delay from the general trend at a two sigma confidence level. Because the energy resolution of the PCA is roughly 1.2 keV (FWHM) around this energy range, some photons of the iron Kα and iron Kβ lines may contaminate this energy band.

As described in the previous sections, we divided the data of P20104 into two segments, the seg1 and the seg2, and also calculated the cross spectrum of them (see also Figure 5.25 and Figure 5.27). We could obtain same results from both the seg1 and the seg2 that the higher energy was advanced to the lower energy (Figure 5.36).

The derived best fit linear functions of each the seg1 and the seg2 are

$$D(E) = -(2.2 \pm 0.5) \times 10^{-4} E(\mathrm{keV}) + (1.2 \pm 0.4) \times 10^{-3}(\mathrm{s}), \tag{5.6}$$

and

$$D(E) = -(3.2 \pm 0.6) \times 10^{-4} E(\mathrm{keV}) + (1.7 \pm 0.4) \times 10^{-3}(\mathrm{s}) \tag{5.7}$$

respectively. The derived delay time of the iron-band data at 6.5 keV are (0.27±0.13) ms and (0.42±0.16) ms respectively.

5.6.2 P10134, P30084, and P40072

Except for P40072, we applied the data of phase lag between 3 Hz to 15 Hz when we fitted the phase lag with a linear function with no offset in the same way of P20104 (see Figure 5.21 for P10134, and Figure 5.29, and 5.29 for P30084). As described in the chapter 4, two different observation mode of PCA, `B_4ms_16B_0_249_Q` and `B_16ms_16A_0_35_H`, were carried out for 30084 observation. Therefore, we calculated the cross spectrum separately for both of them based on the observation mode (Figure 5.29 and Figure 5.29).

For P40072, we only applied the data of phase lag between 3 Hz to 10 Hz because coherences of both the lower energy and higher energy band were significant only upto ~10 Hz as shown in Figure 5.33.

In the same way, these results of the above three observations are plotted as a function of the energy (see Figure 5.37 for P10134, both Figure 5.38 and Figure 5.39 for P30084, and Figure 5.40 for P40072).

P10134

Unlike results of the other observations, it was not clearly seen that the higher X-ray continuum was advanced as compared to that of the iron-band. But, to confirm whether the iron-band delayed from the other continuum band or not, we fitted the time delay data with a linear function, and the best fit linear function is

$$D(E) = -(1.0 \pm 1.0) \times 10^{-4} E(\mathrm{keV}) + (5.4 \pm 7.0) \times 10^{-3}(\mathrm{s}). \tag{5.8}$$

The derived delay time of the iron-band data at 6.5 keV from this data was (0.14±0.39) ms.

As a result, we could not obtain significant results that the iron-band delayed from the other continuum band using the data of this observation.

P30084

We also found the same trend as discovered in P20104 that the time variation in the higher energy band was advanced relative to the lower energy band.

To investigate that the iron-band was delayed from the continuum X-rays, we applied the linear function to the data in Figure 5.38 again. The best fit linear functions to the data of `B_4ms_16B_0_249_Q` and `B_16ms_16A_0_35_H` mode are

$$D(E) = -(2.9 \pm 0.5) \times 10^{-4} E(\mathrm{keV}) + (1.5 \pm 0.5) \times 10^{-3}(\mathrm{s}), \tag{5.9}$$

and

$$D(E) = -(3.7 \pm 0.8) \times 10^{-4} E(\mathrm{keV}) + (1.7 \pm 0.6) \times 10^{-3}(\mathrm{s}) \tag{5.10}$$

respectively.

The derived delay times of the iron-band data at 6.5 keV from each data are (0.32±0.30) ms and (0.66±0.26) ms, respectively, where the error is the one sigma confidence level. Therefore, we marginally detected the delayed iron line component at nearly the one sigma and two sigma confidence level, respectively.

Since both results are consistent with each other within the error, we added both result and fitted these data using the linear function and obtain the fitting result:

$$D(E) = -(3.0 \pm 0.5) \times 10^{-4} E(\mathrm{keV}) + (1.5 \pm 0.4) \times 10^{-3}(\mathrm{s}). \tag{5.11}$$

The derived delay time of the iron-band data at 6.5 keV is (0.52±0.20) ms.

P40072

From the result in Figure 5.40, it was also clear that the higher energy band is advanced. We fitted this data using the linear function. The derived best fit linear function is

$$D(E) = -(2.9 \pm 1.6) \times 10^{-4} E(\mathrm{keV}) + (2.3 \pm 1.3) \times 10^{-3}(\mathrm{s}). \tag{5.12}$$

The deviation of the iron-band data at 6.5 keV from this best-fit model is +(0.41±0.70) ms. Therefore, we could not obtain a significant delayed iron line component since the error was big. But this result is consistent with the other data within 1.1 σ.

5.7 Summary of the Cross Spectral Analysis

We discovered, for the first time, significant time delays of iron-band relative to the general trend of the other energy bands from P20104 and P30084 observations. Our derived delay time of them are (0.39±0.10) ms from P20104 observation, and (0.32±0.30) ms and (0.66±0.26) ms from `B_4ms_16B_0_249_Q` mode of P30084 and `B_4ms_16A_0_35_H` respectively. All are consistent with each other within an error.

But, we could not obtain significant time delay from P10134 and P40072. However, the delay time of P10134, (0.14±0.39) ms, is consistent to that of P20104 and P30084. As indicated in this section 1, the data of P10134 still may include the pre-eclipsing dips after subtracted the #2, #4, and #5.

The result of the time difference of iron-band of P40072 is +(0.41±0.70) ms. Since the observation time of 40072 is shorter than the others, the error of calculated delay time is large. The derived value is deviate by only 1.1 σ from the other observations.

We also discovered the advance of the time variation of the higher energy X-ray. As shown in Figure 5.35 – 5.40, all results show the similar trend as a function of the X-ray energy, and the slope of all data, $\frac{dt}{dE}$, is consistent to each other, where t is the derived delay time of each energy band and E is the X-ray energy. The mean value of $\frac{dt}{dE}$ is $-(2.7\pm0.3)$ msec/keV.

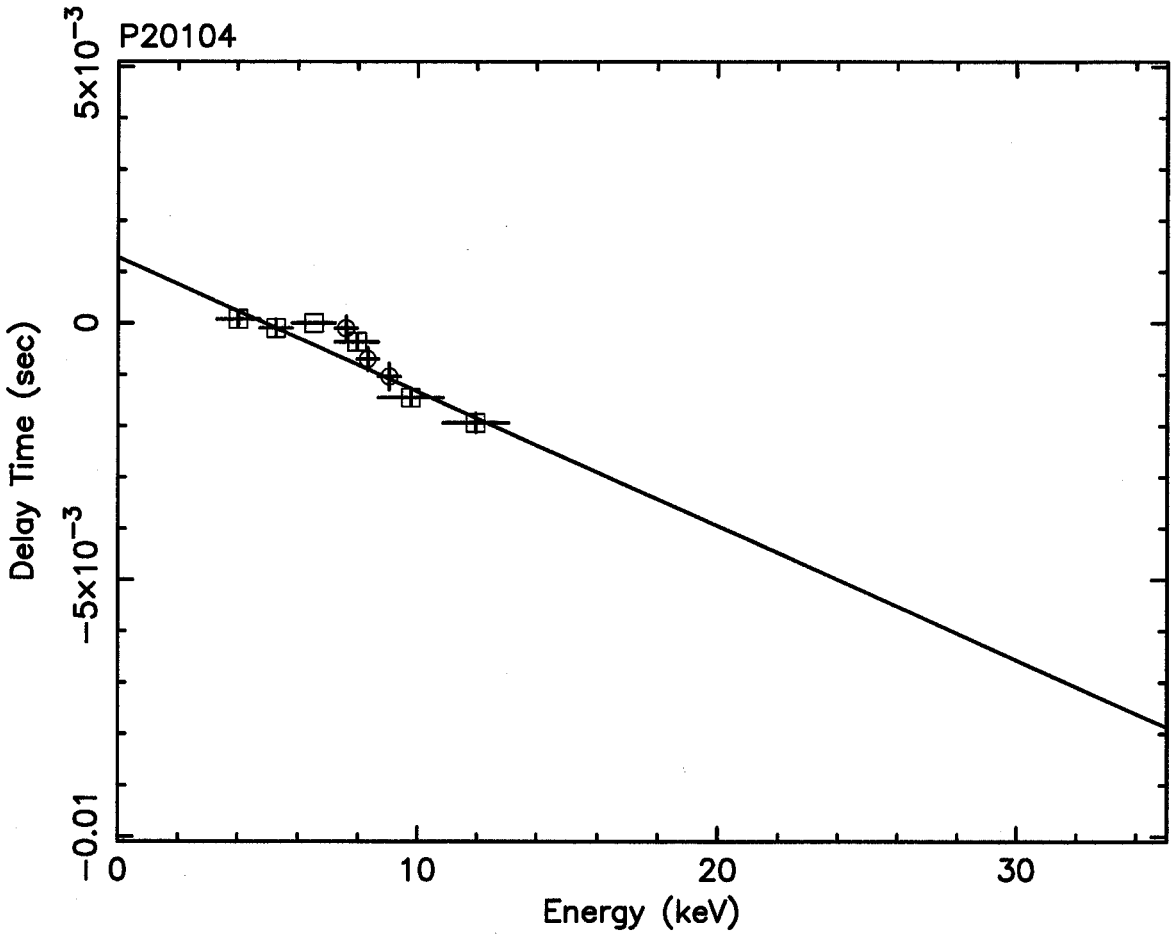

Figure 5.35: The time delay in the time variation from that of the iron-band as a function of the X-ray energy in P20104 data. The five squares are the data obtained from the original six energy channels, and the line around ~6.5 keV is marked for reference. The circles are the data derived by using more finely binned energy bands. Errors are one sigma confidence levels. The best-fit linear function is also plotted.

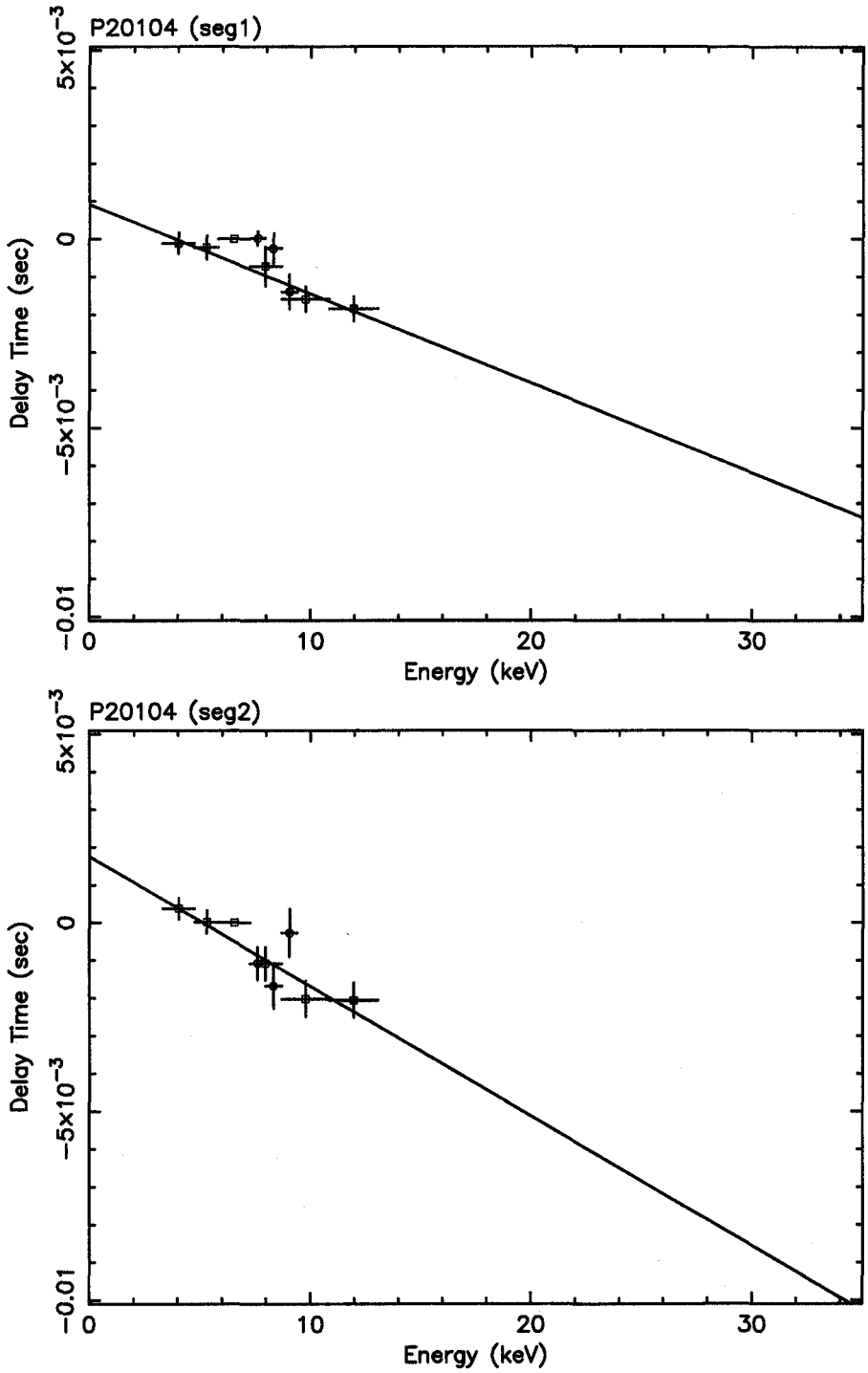

Figure 5.36: The time delay in the time variation from that of the iron-band as a function of the X-ray energy in both seg1 (upper panned) and seg2 (lower panned) of P20104 data. Errors are one sigma confidence levels. The best-fit linear function is also plotted.

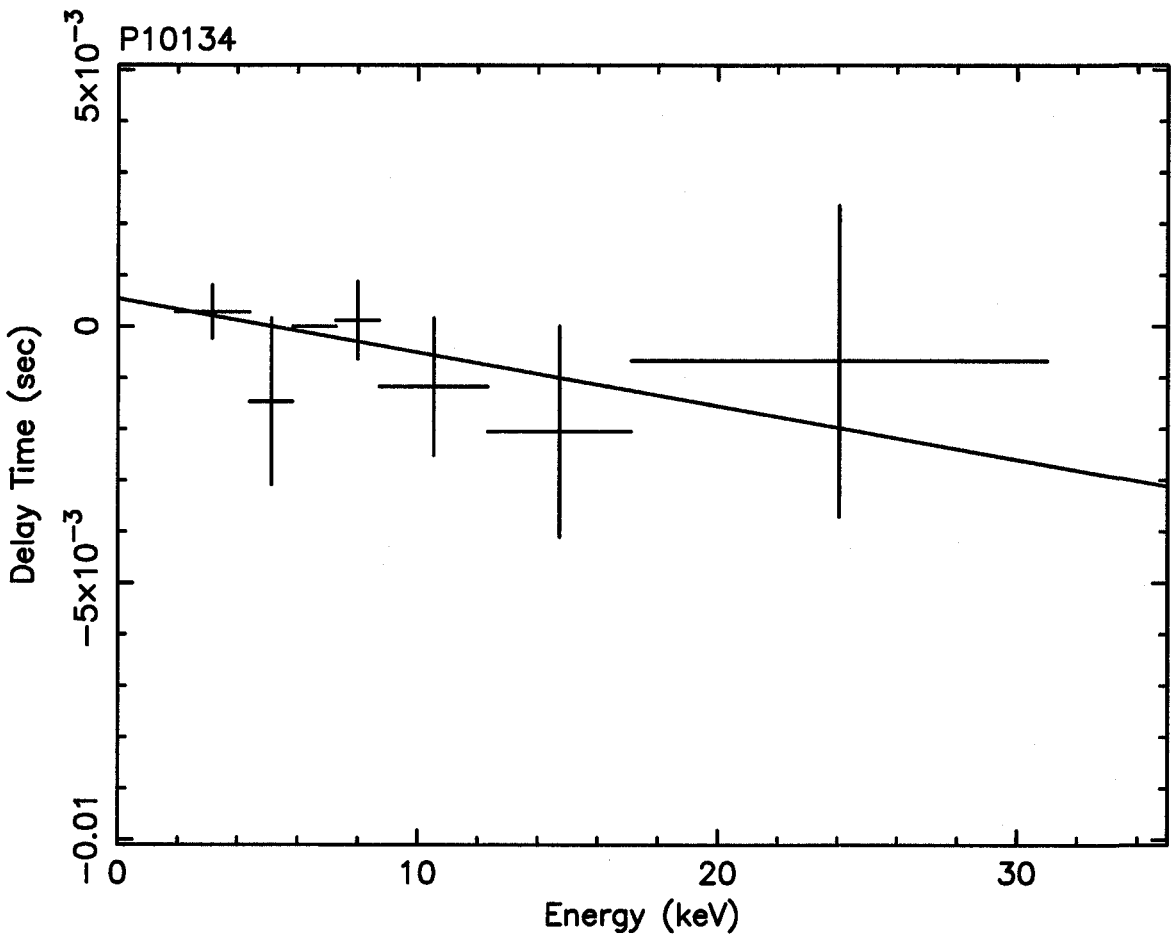

Figure 5.37: The time delay in the time variation from that of the iron-band as a function of the X-ray energy in P10134 data. Errors are one sigma confidence levels. The positive direction of the vertical axis represents the delay from the variation of the iron-band. The best-fit linear function is also plotted.

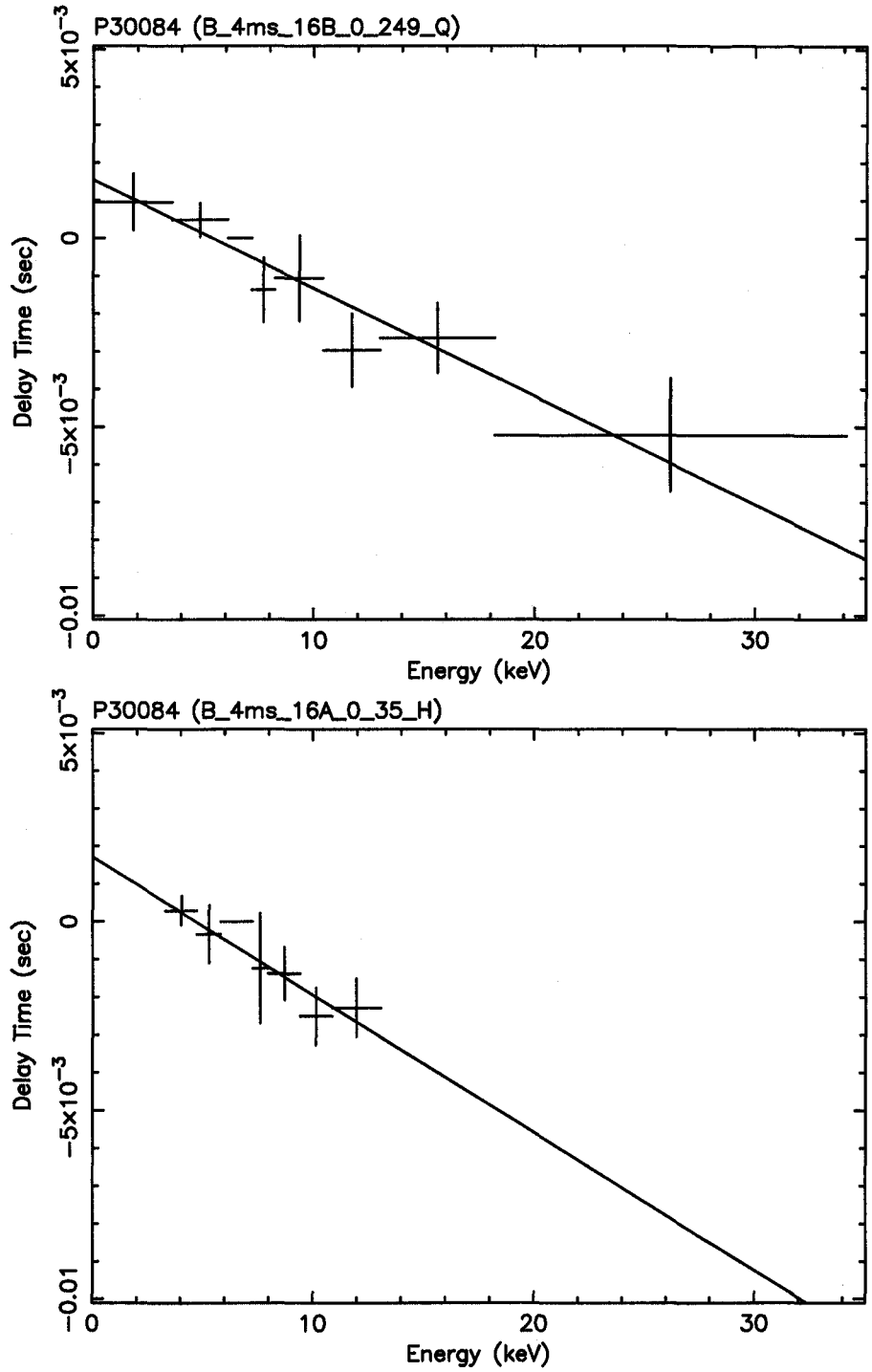

Figure 5.38: The time delay in the time variation from that of the iron-band as a function of the X-ray energy in both `B_4ms_16B_0_249_Q` (upper pannel) and `B_4ms_16A_0_35_H` (lower pannel) of P30084 data. Errors are one sigma confidence levels in each data. The best-fit linear function is also plotted.

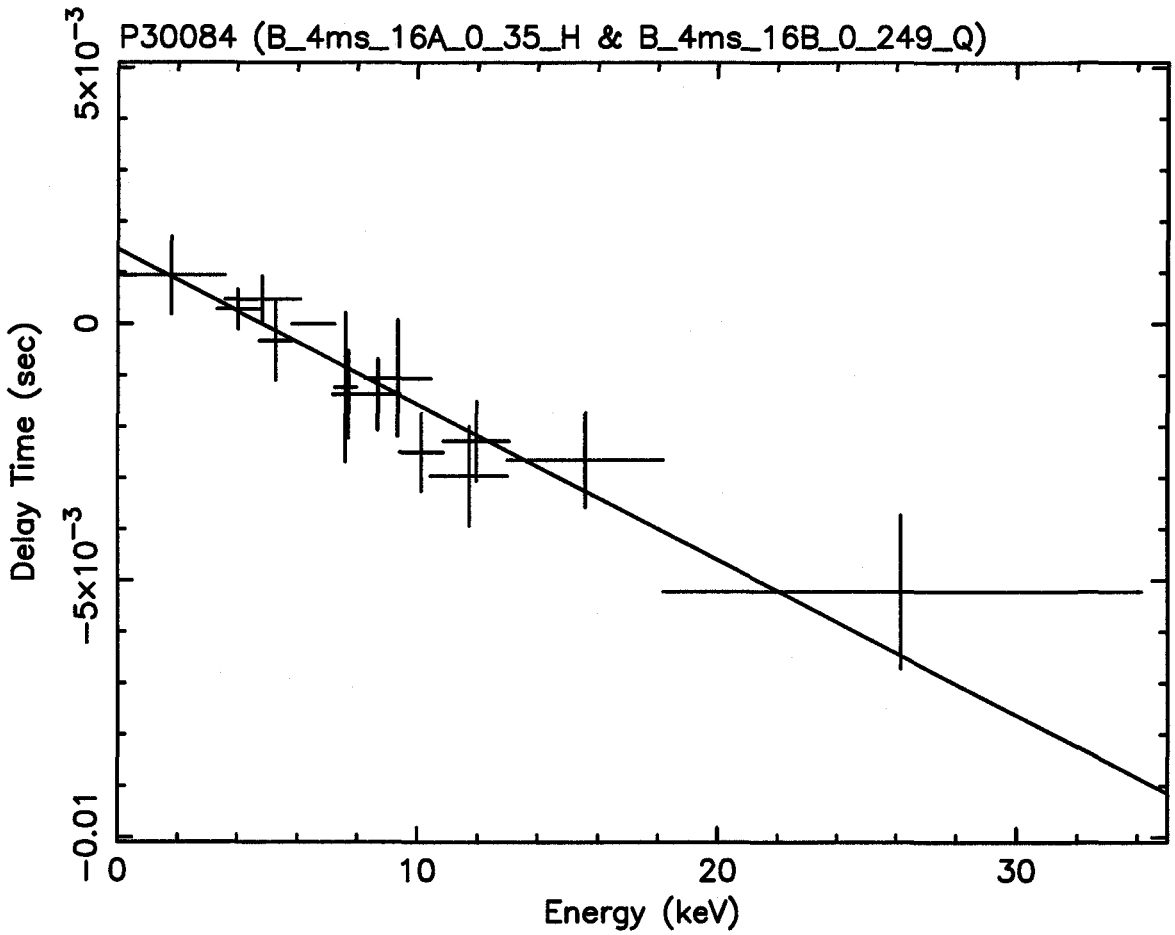

Figure 5.39: The time delay in the time variation from that of the iron-band as a function of the X-ray energy in P30084 data. Both `B_4ms_16B_0_249_Q` and `B_4ms_16A_0_35_H` are plotted in this Figure. Each data of `B_4ms_16B_0_249_Q` and `B_4ms_16A_0_35_H` is shown in the previous Figure. Errors are one sigma confidence levels. The best-fit linear function is also plotted.

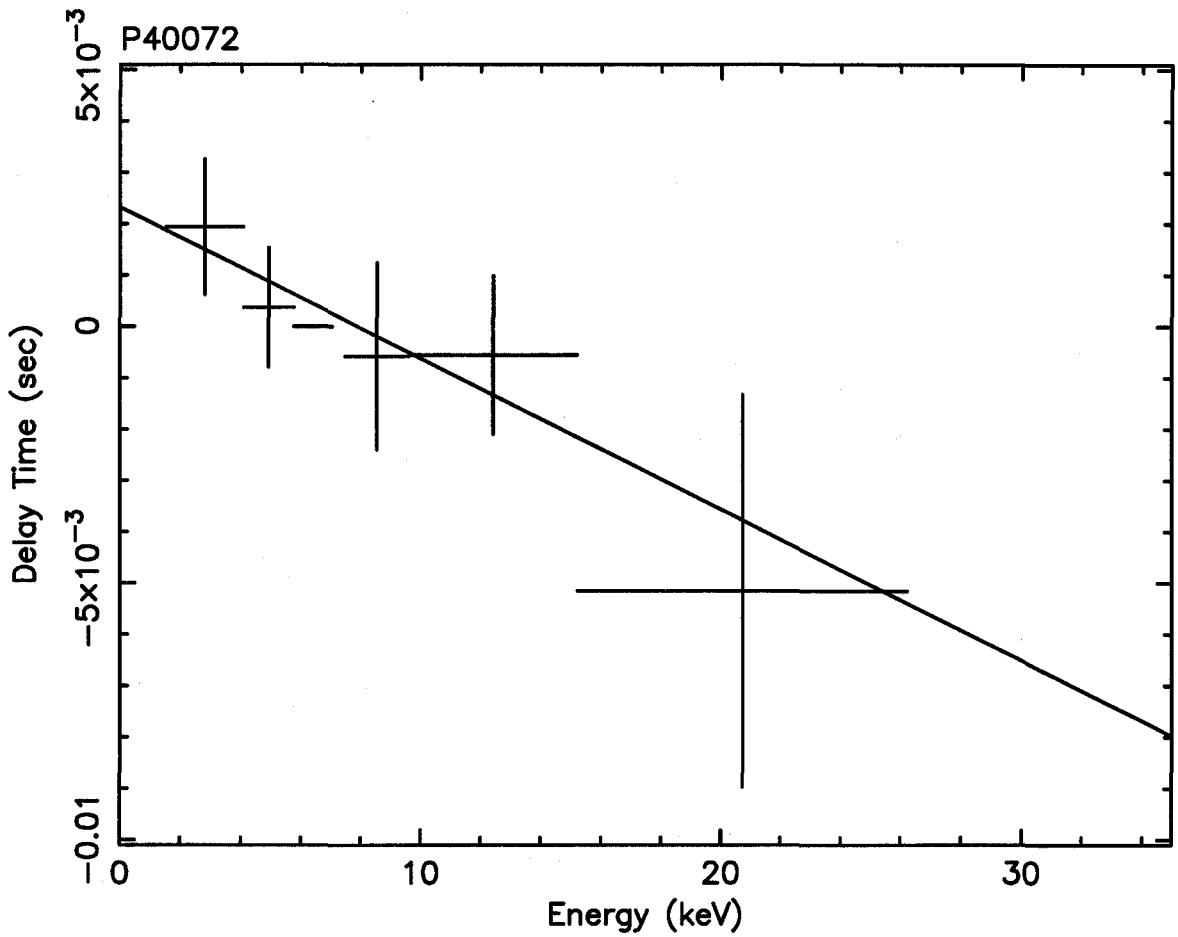

Figure 5.40: The time delay in the time variation from that of the iron-band as a function of the X-ray energy in P40072 data. Errors are one sigma confidence levels. The best-fit linear function is also plotted.

Chapter 6

Discussion

Using the cross spectrum, we discovered the variation of the iron-band was delayed as compared to that of the other continuum X-rays and also discovered the time difference showed a general trend such that the higher energy X-rays advanced in comparison with the lower energy X-rays with the exception of the iron-band. In this chapter, we will discuss that the interpretation of them.

6.1 Distance to the Reprocessor

We derived significant time delays of the iron-band relative to the general trend of the other energy bands from P20104 and P30084. These derived values are $-(0.39\pm0.10)$ ms from P20104, and $-(0.32\pm0.30)$ ms and $-(0.66\pm0.26)$ ms from `B_4ms_16B_0_249_Q` and `B_4ms_16A_0_35_H` mode of P30084 respectively. Since the results of the other observations, P10134 and P40072, did not show significant time delay of iron-band, but their results are consistent within the error.

Although, our derived delay times, the order of several hundreds μs, are much smaller value than our expected value from the size of Alfv́en shell, the order of ms, our derived values may not necessarily represent an actual delay of the reprocessed X-rays for the following two reasons.

1. The fraction of iron line photons in the iron-band of each observations is only $\sim$10%. We, therefore, need to estimate the actual delay of the line emission from general trend of the other energy bands.

2. Our derived delay time is a deviation of the iron-band from the general trend and may not be the delay from the original temporal variation.

For the reason 1 given above, we simulated the relation of the actual delay to the observed delay in our analysis as follows for each observations.

The effect of the mixture of the delayed and non delayed components in the iron-band must depend on the time variation itself. Therefore, we used the observed data of P20104, which was the longest observations, in the two energy bands, 3.3–4.7 keV and 4.7–5.8 keV. These two bands have no significant phase lags from each other, and the shape of the PSDs are almost similar (The shapes of the other energy bands, including iron-band, are also very similar). Then, we constructed an artificially delayed light curve using 3.3–4.7 keV band, where we assumed three fractions (5%, 10%, and 20%) of the delayed component and five lag times (0, 1, 2, 5, and 10 ms). We applied the cross spectrum to these data sets and derived the delay time of the artificially delayed light curves with regards to the 4.7–5.8 keV band. Although the light curves of the both energy bands had no significant delay time, the calculated delay time without an additional delay was a finite value with $\sim 2 \times 10^{-4}$ s. This value was not interested one for the estimation of the effect of the photon mixture. Thus, we subtracted this value from the calculated delay time. These results are shown in Figure 6.1.

The iron line fraction in the iron-band is estimated to be $\sim$10% of both P20104 and P30084 observations. Here, we have to note that, in the simulation, we assumed that the time variations (shape and fraction of the variation) of both the non-delayed photons and delayed photons were the same to each other. In other word, the fraction means the fraction of the variable component. However, the variation of the iron line may be different from the continuum component in the iron-band. Now, we are considering that the iron lines are reprocessed component of the photons above the iron K absorption edge. Thus, the variation of the iron line must be assumed as the variation of the continuum X-rays above the iron K absorption edge.

To compare the difference of the variation of iron line with that of the continuum X-ray component in the iron-band, we calculated the PSDs normalized by the square of the mean intensity (hereafter NPSD) , which was proportional to (rms. Amplitude)^2 / Intensity^2, of each energy bands and compared the integration of the NPSD for each of them.

- P20104

  We calculated the NPSD among six energy bands and integrated of calculated NPSDs between 3 Hz and 15 Hz of each energy bands. These results are summarized in Table 6.1.

  Then, we compared the integration of NPSD of iron-band with that of the 7.25–8.69 keV band, which was the main component of the original X-rays of iron lines.

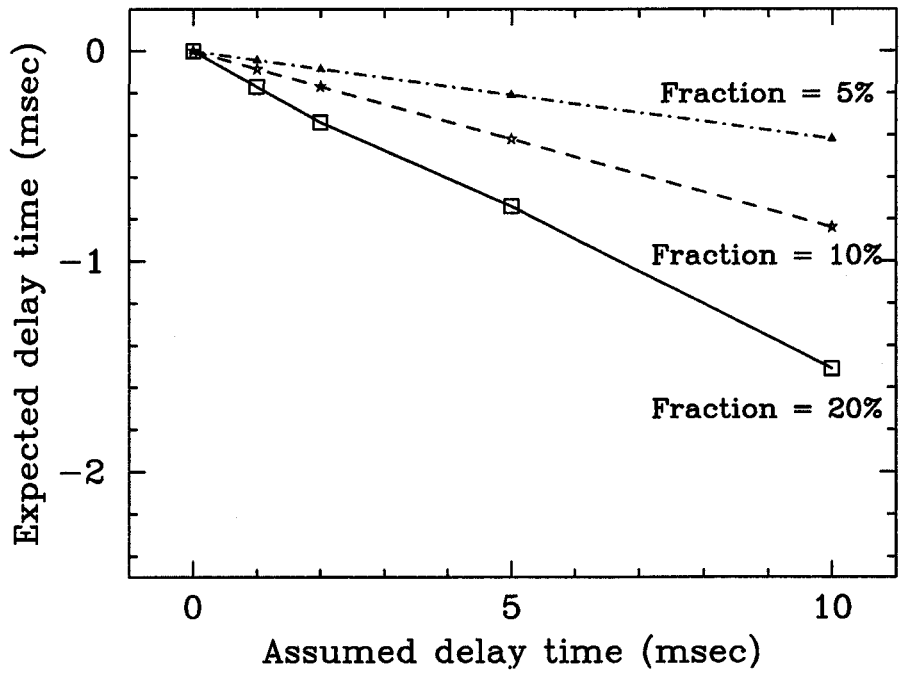

Figure 6.1: The relation between the expected time delay and the assumed time delay of P20104. Using the light curve in 3.3–4.7 keV band, We constructed an artificial light curve where certain fractions (5%, 10%, and 20%) of the X-rays are delayed by the assumed delay times. The same analysis was applied and the expected delay time between the artificially delayed light curve and the light curve in 4.7–5.8 keV band was calculated. Because even if the assumed delay was 0 s, a finite delay time was derived, all the data were shifted by this derived value.

Table 6.1: 3–15 Hz integrated normalized power spectral densities of P20104.

energy range (keV)	cts/s	Integrated (3-15 Hz) NPSD
3.31–4.73	581.2	1.31×10^{-4}
4.73–5.81	431.8	1.45×10^{-4}
5.81–7.25	609.2	1.43×10^{-4}
7.25–8.69	453.8	1.57×10^{-4}
8.69–10.87	543.4	1.55×10^{-4}
10.87–13.06	404.8	1.43×10^{-4}

The integration of the 7.25–8.69 keV band was 1.09 times larger than that of the iron-band. Thus, the rms amplitude of the original photons of the iron lines was 1.05 times larger than the continuum X-rays in the iron-band.

Consequently, we had to consider that the fraction of the variable component in the iron-band was 9.5%, and the calculated delay time of (0.39±0.10) ms was considered to be the actual delay of the iron line X-ray of (5.1±1.4) ms from the major component of the iron-band photons, i.e., the continuum X-rays in the iron-band.

- P30084

  Table 6.2 shows the integration of the NPSD of each energy bands of the two observation modes. The integration of the 7.17–8.26 keV band was 1.02 times larger than that of the iron-band (6.09–7.17 keV) in `B_4ms_16B_0_249_H` mode, and the integration of the NPSD of 7.25–8.69 keV band was the same value of the iron-band (5.81–7.25 keV) in `B_4ms_16A_0_35_H` mode.

  Consequently, we had to consider the difference of the variable component in the iron-band only for the data of `B_4ms_16B_0_249_H`. Then, we considered the fraction of the variable component in the iron-band was 10.7%, and the calculated delay time of (0.32±0.30) ms was considered to be the actual delay of the iron line X-ray of (2.9±2.7) ms from the major component of the continuum X-rays in the iron-band. For `B_4ms_16A_0_35_H`, fraction of the variable component in the iron-band was 8.6%, and the calculated delay time of (0.66±0.26) ms was considered to be the actual delay of the iron line X-ray of (8.8±3.5) ms from the major component of the continuum X-rays in the iron-band.

For the reason 2 given above, because we interpret that the iron lines to be fluorescent lines at a reprocessor, the original photons are though to be the photons above the iron K absorption edge. However, the derived delay time of (5.1±1.4) ms, (2.9±2.7) ms, and (8.8±3.5) ms were delay time from the continuum X-rays in the iron-band. Due to the energy dependence of the delay time, there is a farther delay time for the photons above the iron K absorption edge. We must calculate it by weighting the original photon number and the absorption cross section. Then, we assumed the best fit linear function of the general energy dependence, a power law spectral shape with a photon index, $P_{index} = -1.245$ (P20104), -1.14 (`B_4ms_16B_0_249_Q` mode of P30084), and -1.119 (`B_4ms_16A_0_35_H` mode of P30084), and the fraction of the photo-electric absorption above the edge of $(1.0 - \exp(-\tau(\frac{E}{E_{th}})^{-3.0}))$, where E was the original photon energy and the E_{th} was the K absorption threshold energy of the iron, and τ was the optical depth at the edge energy. We estimated

Table 6.2: Upper (Lower) Table shows 3–15 Hz integrated normalized power spectral densities of B_4ms_16B_0_249_H (B_4ms_16A_0_35_H) mode of P30084.

mode	energy range (keV)	cts/s	Integrated (3-15 Hz) NPSD
B_4ms_16B_0_249_H	0.00–3.57	380.6	4.97×10^{-4}
	3.57–6.09	1173.0	5.32×10^{-4}
	6.09–7.17	508.2	5.02×10^{-4}
	7.17–8.26	384.9	5.12×10^{-4}
	8.26–10.44	649.1	5.53×10^{-4}
	10.44–13.00	554.4	5.59×10^{-4}
	13.00–18.18	535.4	5.03×10^{-4}
	18.18–34.13	213.6	3.61×10^{-4}
B_4ms_16A_0_35_H	3.31–4.73	486.4	2.61×10^{-4}
	4.73–5.81	369.8	2.90×10^{-4}
	5.81–7.25	529.2	2.74×10^{-4}
	7.25–8.00	192.4	2.74×10^{-4}
	8.00–9.42	373.7	2.83×10^{-4}
	9.42–10.87	336.5	2.75×10^{-4}
	10.87–13.06	373.2	2.78×10^{-4}

the optical depth of the iron K absorption from the energy spectrum to be less than 0.1. Considering the equivalent width of the iron line, the optical depth was not much smaller than the 0.1. Ebisawa et al. (1996) reported that the optical depth was (0.52±0.10) from *ASCA* SIS data. Thus, we calculated the average delay time of the continuum X-ray in the iron-band from the original X-rays above iron K absorption edge as;

$$\frac{\int_{E_{th}}^{\infty}(A\times 10^{-4}(E-6.4\ keV))E^{P_{index}}(1.0-\exp(-\tau(\frac{E}{E_{th}})^{-3.0}))dE}{\int_{E_{th}}^{\infty}E^{P_{index}}(1.0-\exp(-\tau(\frac{E}{E_{th}})^{-3.0}))dE}. \tag{6.1}$$

where E_{th} was the cut off energy of 7.1 keV, A was the slope of the linear function of general energy dependence of each observations, P_{index} was the photon index of each observation, −1.245 (P20104), −1.14 (`B_4ms_16B_0_249_Q` mode of P30084), and −1.119 (`B_4ms_16A_0_35_H` mode of P30084). We applied the optical depth, τ, for the extreme cases of both 0.1 and 0.52. Using equation 6.1, we derived the delay time of P20104 between the continuum X-rays in the iron-band and the original photons above the iron K absorption edge was 0.89 ms and 0.94 ms for τ =0.1 and τ=0.52, respectively. The result of `B_4ms_16B_0_249_Q` (`B_4ms_16A_0_35_H`) of P30084 was 1.03 ms (1.32 ms) and 1.08 ms (1.38 ms) for τ =0.1 and τ=0.52, respectively.

Thus, the actual delay time of the iron lines from the original photons of each observation, P20104, `B_4ms_16B_0_249_Q` mode of P30084, and `B_4ms_16A_0_35_H` mode of P30084, must be considered to be (6.0±2.4) ms, (4.0±3.8) ms and (10.1±4.9) ms respectively.

These delay time must be interpreted as being due to the difference of the light path between the direct X-rays from a neutron star and the reprocessed X-rays because the life time of the iron ions in the excited state is order of 10^{-15} s, and it is much shorter than our derived delay time. Although we do not know the geometry of the reprocessor, it may cover more than half of the sphere (i.e., 2π steradian) as seen from the neutron star (Ebisawa et al. 1996), and our derived delay time is the averaged delay time during the observation. Thus, we assumed the spherical shell for the reprocessor and calculated the distance between the neutron star and the reprocessor by simply multiplying our derived delay time by light velocity. By this method, we determined the distance between the neutron star and the reprocessor based on each observations to be (1.8±0.7)× 10^8 cm, (1.2±1.1)× 10^8 cm, and (3.0±1.7)× 10^8 cm.

6.2 Accretion Flow and Beat Frequency Model

From previous discussion, we derived that the distance between the neutron star and the reprocessor was (1.7±0.5)×10^8 cm, (1.2±1.1)× 10^8 cm, and (3.0±1.7)× 10^8 cm from each observation. In addition, we found these distances were similar or even smaller than the expected size of the magnetosphere derived from the QPO model as shown in later. Because the equivalent width of the iron line is ∼128 eV, the reprocessor must cover more than half of the sphere (e.g., Ebisawa et al. 1996). On the other hand, the discovery of the pulsed iron line (Day et al. 1993b) indicates that the reprocessor does not cover the whole neutron star, if the reprocessor is optically thin. Here, using the result of P20104 observation as an example, we will evaluate our derived distance between the neutron star and the reprocessor as follows.

The energy of the iron K absorption edge determined by *ASCA* SIS (Ebisawa et al. 1996) indicates that the ionization state is at most Fe IX. This requires the ionization parameter $\xi = L/(nr^2)$ (Tarter, Tucker, & Salpeter 1969) must be 1–10^2 (Kallman & McCray 1982). Considering the observed luminosity (L ∼10^{38} ergs^{-1}) of Cen X-3 and the distance of r (1.7×10^8 cm), the density, n, can be calculated as 3.5×10^{19} cm^{-3} – 3.5×10^{21} cm^{-3}. The luminosity of 1×10^{38} erg s^{-1} corresponds to the accretion rate of 2.7×10^{-15} $\varepsilon_{0.1}^{-1}$ $M_\odot$ s^{-1}, or 3.2×10^{42} $\varepsilon_{0.1}^{-1}$ protons s^{-1}. These protons will fall along the magnetic field lines toward the magnetic polar caps, forming a part of a shell and finally forming accretion columns. Although the thickness of the shell, or the diameter of the accretion columns are not known, if the area of their cross sections across the flow is assumed to be ∼$4\pi r^2/1000$ and the velocity of the flow is free fall velocity, the expected number density is ∼10^{19} $(r/10^8\mathrm{cm})^{-1.5}\varepsilon_{0.1}^{-1}$ cm^{-3}. Thus the density derived by the ionization state is not unreasonable.

The radius of the magnetosphere and the magnetic dipole moment of the neutron star can be evaluated by assuming the BFM. In chapter 5, we detected the QPO frequency of (41±3) mHz. Using the BFM, the Keplerian frequency must be 0.249 Hz since the spin frequency is 0.208 Hz (see chapter 4). Consequently, we derived the Alfv́en radius, r_A, and the magnetic dipole momentum in unit of 10^{30} G cm^3, μ_{30} as

$$r_A = 3.8 \times 10^8 \left(\frac{M}{M_\odot}\right)^{1/3}\mathrm{cm}, \tag{6.2}$$

$$\mu_{30} = 4.5\, L_{38}^{1/2}\varepsilon_{0.1}^{-1/2}\left(\frac{M}{M_\odot}\right)^{5/6}\mathrm{Gcm}^3, \tag{6.3}$$

respectively. This radius of the magnetosphere is larger by a factor of ∼2 than our measurement based on the delay time. This discrepancy can be reconciled by considering that the

reprocessor is distributed from the neutron star to the magnetosphere along the magnetic field. Therefore, our derived distance, between the reprocessor and the neutron star, strongly supports the BFM.

In the same way, we derived the size of the magnetosphere from P30084 observation. In chapter 5, the QPO frequency derived from `B_4ms_16B_0_249_Q` and `B_4ms_16A_0_35_H` mode were (46±4) mHz and (39±1) mHz respectively. Then, the derived Keplerian frequency must be 0.254 Hz and 0.247 Hz using the spin period of 0.208 Hz derived in chapter 5. Thus, we derived the r_A and μ_{30} as,

- `B_4ms_16B_0_249_Q` mode

$$r_A = 3.7 \times 10^8 (\frac{M}{M_\odot})^{1/3} \mathrm{cm}, \tag{6.4}$$

$$\mu_{30} = 4.6\, L_{38}^{1/2} \varepsilon_{0.1}^{-1/2} (\frac{M}{M_\odot})^{5/6} \mathrm{Gcm}^3, \tag{6.5}$$

and

- `B_4ms_16A_0_35_H` mode

$$r_A = 3.8 \times 10^8 (\frac{M}{M_\odot})^{1/3} \mathrm{cm}, \tag{6.6}$$

$$\mu_{30} = 4.6\, L_{38}^{1/2} \varepsilon_{0.1}^{-1/2} (\frac{M}{M_\odot})^{5/6} \mathrm{Gcm}^3. \tag{6.7}$$

These derived radius of the magnetosphere of P30084 observation are also larger value than the radius derived from the delay time. Therefore, these discrepancy can be also reconciled by considering that the reprocessor is distributed from the neutron star to the magnetosphere along the magnetic field.

6.3 Where Dose the Cyclotron Resonance Scattering Occur?

Cyclotron features, observed in the high energy X-ray spectra of strongly magnetized neutron star, provide a powerful diagnostic tool for determining the magnetic field strength close to the neutron star surface. An X-ray emission of the accretion powered pulsar is due to funneling of ionized hot plasma onto the magnetic polar caps of the neutron star. Because the electron-photon interaction in the plasma is dominated by cyclotron resonance scattering in the strong magnetic field of order of $B{\sim}10^{12}$ G, one can determine the magnetic field strength

from the observed electron resonance energy in the energy spectrum which is related to the magnetic field strength by $E_{cyc} = 11.6 \times B_{12}$ keV (where B_{12} is the magnetic field strength in units of 10^{12} G). Then, we determined the transition energy of the Landau levels by the spectral analysis as descrived in chapter 5, and calculated the magnetic field strength at the X-ray emission region from our derived Landau transition energy. These results are summarized in Table 6.3.

We also determined the magnetic dipole moment, assuming a simple dipole magnetic field,

$$\mu_{30} = B_{12} (\frac{r_{cyc}}{10^6 \mathrm{cm}})^3 \ \mathrm{Gcm}^3, \tag{6.8}$$

where B_{12} was the magnetic field strength in units of 10^{12} G at the position where the cyclotron resonance scattering occurs, and r_{cyc}, was its radius from the center of the neutron star. On the other hand, the BFM predicts the strength of the magnetic dipole moment as shown in Table 6.3.

Table 6.3: Electron resonance energy, the magnetic field strength, and the magnetic dipole moment.

Obs ID	Cyclotron Resonance Energy (keV)	Magnetic Field Strength (G)†	Magnetic Dipole Moment ($\times L_{38}^{1/2} \varepsilon_{0.1}^{-1/2} (\frac{M}{M_\odot})^{5/6}$G cm^3) ‡
P20104	26.4	2.27	4.5
P30084 (#1–#5)	24.9	2.15	4.6
P30084 (#6–#10)	26.3	2.27	4.6

† in unit of 10^{12} G

‡ in unit of 10^{30} Gcm^3

Then, comparing equations (6.3), (6.5),and (6.7) with equation (6.8), we estimated the radius of region where the cyclotron resonance scattering occurs. These results are summarized in Table 6.4. Our derived radius of the X-ray emission region must be considered to be almost on the surface of the neutron star.

Table 6.4: The radius of the region where the cyclotron resonance scattering occurs.

Obs ID	Radius (r_{cyc}) ($\times L_{38}^{1/6} \varepsilon_{0.1}^{-1/6}$ $(M/M_\odot)^{5/18}$ cm) †
P20104	1.26
P30084 (#1–#5)	1.29
P30084 (#6–#10)	1.26

† in unit of $\times 10^6$ cm

6.4 Advance of Hard X-rays

We also discovered the time variation of the hard X-rays were advanced as compared with that for the soft X-rays. In other words, we discovered soft lag in the continuum X-ray. Our derived time lags were roughly expressed by a linear function with the X-ray energy up to ~30 keV. Two possibilities must be examined of these soft lags: either the lower energy bands as well as the iron-band include reprocessed X-rays (i.e. scattered X-rays and fluorescent X-rays) or the time variation represents an intrinsic variation in the original X-ray emission. Here, we will discuss the above two possibilities, using the result of P20104 as an example.

In the former case, the time difference must be a fraction of the reprocessed components; the scattered component and the fluorescent component. Since the energy shift by the scattering is small, the fraction of the scattered component to the direct component can be estimated by the cross section of the scattering. Since there is no evidence which indicates the large optical depth of the scattering for Cen X-3, the fraction of the scattered component is roughly proportional to the cross section. The difference of the scattering cross section between 3 keV and 13 keV is less than 4%. If we take account of the absorption by the scatterer, the amount of the scattered component in the low energy band becomes small and the difference of the fraction of the scattered component between 3 keV and 13 keV must be smaller than 4%. The observed time difference is roughly 1 ms between the iron-band and the highest energy band. If we assume that the scattered component delays by ~6 ms, the required difference of the fraction of the scattered component is more than 20% (see Figure 6.1). Thus the effect of the scattered component can not explain the observed general trend of the time difference. The fluorescent lines from Si, S, and Ar may be contained in the lower energy bands. Thus, a part of the reason for the low energy delay may be due to these fluorescent lines. However, in the energy range above 8 keV, we can not expect any fluorescent lines. Therefore, the general trend of the energy dependence can not be explained

by the contamination of the reprocessed X-rays.

In the latter case, we may consider a qualitative argument. As mentioned in chapter 2, the continuum X-ray emission mechanism has thought to be an up-Comptonization of the soft photons by the hot electrons in the atmosphere of the accretion column by some authors (e.g., Mészaros 1995). But, we will expect not the soft lag but the hard lag in the time variation of the continuum X-ray if we apply their idea. Therefore, we have to think the other continuum X-ray emission mechanism in the accretion column. Then, we assumed that our derived short term intensity variation could be interpreted as being due to the variation of the amount of material falling onto the polar cap of the neutron star. The intensity must become high when the large amount of matter falls on the polar cap. The kinetic energy of the falling matter is converted into thermal energy almost instantaneously, resulting to make an extremely high temperature plasma. This plasma must cool down via radiation and conduction, and consequently the hard X-ray advance is expected. Although the quantitative consideration is not discussed in this work, this discovery of the hard advance may be related to the interaction between the accretion matter and the neutron star.

Chapter 7

Conclusion

We have investigated the aperiodic time variation of X-ray binary pulsar, Cen X-3, observed with *RXTE* to determine where the emission region of the iron lines is. We have applied the cross spectral analysis to calculate the phase lags between the light curves of the iron-band and the other continuum X-ray bands. Our results are summarized as follows.

- We could derive significant delay time of temporal variation of the iron-band from two data, P20104 and P30084, as compared with that of the other energy X-rays. Our derived delay times are (6.0±2.4) ms from P20104, and (4.0±3.8) ms and (10.1±4.9) ms from P30084.

- We could not obtain the significant delay time from P10134 and P40072. However, the delay time of P10134, (0.14±0.39) ms, is consistent to that of P20104 and P30084. The result of P40072 is advance of (0.41±0.70) ms, and this result is also consistent with other results within the error.

- Assuming the spherical distribution of the reprocessor of iron lines around the neutron star, we calculated the distance between neutron star and the reprocessor by simply multiplying our derived delay time by light velocity. As results, we determined the distance between the neutron star and the reprocessor based on each observations to be (1.8±0.7)× 10^8 cm from P20104, and (1.2±1.1)× 10^8 cm and (3.0±1.7)× 10^8 cm from P30084.

- The advance of the hard X-ray variation was also discovered from all data of Cen X-3. We think this advanced trend of the continuum X-ray is related to the X-ray emission mechanism on the neutron star.

- Applying the BFM, our derived distances to the reprocessor were smaller than the size of the magnetosphere (i.e., Alfv́en radius, r_A). Finally, we concluded that the reprocessor of iron lines was distributed from the neutron star to the magnetosphere along the magnetic field.

Using the cyclotron resonance energies which we detected by the spectral analysis of Cen X-3, we derived the magnetic dipole moment $\sim 4.5 \times 10^{30}\, L_{38}^{1/2} \varepsilon_{0.1}^{-1/2} (\frac{M}{M_\odot})^{5/6}$ G cm^3. We also derived the magnetic dipole moment using the above described value of r_A. From these two results, we calculated the radius where the cyclotron scattering occurs to be $\sim 1.7 \times 10^6$ cm. Thus, we determined that the region where the cyclotron scattering occurs was estimated to be close to the surface of the neutron star.

We also determined the orbital parameters of Cen X-3 and confirmed the negative rate of orbital period change, $\dot{P}_{orb}/P_{orb}$, of $(1.77 \pm 0.04) \times 10^{-6}$ yr^{-1}. This value is consistent with Kelley et al. (1983) within one σ error, and more precise by a factor of two. In addition, the value derived by Nagase et al. (1992) is also consistent with our result within one σ error. We also determined the pulse period of 4.814249 ± 0.000009 s, and confirmed the source was still in a spin up state.

Finally, we will have to build a reasonable model for the X-ray emission mechanism to explain our discovered the soft lag of the continuum X-rays, and it will be a homework for the future!

Appendix A

Timing Analysis

In the current study, standard techniques, Power Spectral Densities(PSDs), epoch folding search (EFS) and cross spectral analysis are employed (e.g., Jenkins and Watt 1968; Leahy et al. 1983; van der Klis 1989; Vaughan et al. 1994). The details of the Fourier techniques used in X-ray astronomy field are described by van der Klis (1989). In this appendix, we will briefly review these techniques.

A.1 Power Spectrum Densities (PSDs)

Here, we treat time segment data with a total data length of T s, which is binned into $N = 2^m$ data bins with the bin width of t s. x'_k stands for the number of photons detected in bin k. The average of x'_k, $\bar{x}$, is expressed,

$$\bar{x} = \frac{1}{N}\sum_{k=1}^{N} x'_k \tag{A.1}$$

and, using above $\bar{x}$, the count data per bin is defined as $x_k = x'_k - \bar{x}$.

The Fourier transform, a_j ($j = -\frac{N}{2}, -\frac{N}{2}+1, \ldots, \frac{N}{2}-1$), is defined as follows:

$$a_j = \sum_{k=0}^{N-1} x_k e^{2\pi ijk/N} \quad j = -\frac{N}{2}, \ldots, \frac{N}{2} - 1. \tag{A.2}$$

$$x_k = \frac{1}{N}\sum_{j=-N/2}^{N/2-1} a_j e^{-2\pi ijk/N}, k = 0, \ldots, N-1. \tag{A.3}$$

Since x_k is a real number and the mean of x_k equals to zero, it is $a(-j) = a(j)*$ and a(0) = $\sum_{j=0}^{N-1} = 0$, where $*$ indicates the complex conjugate.

The Parseval's theorem states:

$$\sum_{k=0}^{N-1} |x_k|^2 = \frac{1}{N} \sum_{j=-N/2}^{N/2-1} |a_j|^2. \tag{A.4}$$

Calculating the total variance of the data series with above definitions, the result of variance is described as:

$$Var(x_k) \equiv \sum_k (x_k - \bar{x})^2 = \frac{1}{N}\sum_k |a_j|^2 - \frac{1}{N}a(0)^2 = \frac{1}{N} \sum_{j=-N/2}^{N/2-1} |a_j|^2, \quad \text{for } j \neq 0 \tag{A.5}$$

then, the power spectrum densities (PSDs) are defined as follows:

$$P_j = \frac{2}{N}|a_j|^2, \qquad j = 0, \ldots, \frac{N}{2} \tag{A.6}$$

Note that a_j is defined for $j = -N/2, \ldots, N/2 - 1$, but the PSDs, P_j, is defined for $j = 0, 1, \ldots, N/2$. The PSDs has half of the information of the original time series data. The lost information is the phase information for each number. The frequency $1/2T$, which corresponds to the maximum wave number $j(= N/2)$, is called as the Nyquist frequency.

In equation A.6, if the total number of photons in the transform, N_{ph}, are applied in spite of N, this is called Leahy Normalization (Leahy et al. 1983). In Leahy normalization, the distribution of powers for Poisson counting noise has a mean value of 2 and obeys the χ^2 distribution with 2 degree of freedom.

Fast Fourier Transform(FFT)

The data series of N, that we usually use, are quite huge number, and they take a long time to calculate the PSDs. Then, the computer algorithm, FFT (e.g., Jenkins & Watt. 1968; Leahy et al. 1983; Press et al. 1988; van der Klis 1989), has long been applied for astronomical data, since FFT is a procedure that involves only $N \log_2 N$ steps compared to N^2 steps for a straightforward method where N is the number of the series, it is much more efficient (faster) than the straight forward method. For $N = 2^{25}$, $N^2/(N \log_2 N) \sim 10^6$.

A.2 Epoch Folding Search

The technique of epoch folding data to search for periodic pulsations is particularly useful with X-ray astronomical observations for a variety of reasons. These include the higher sensitivity to nonsinusoidal pulse shapes which are characteristics of X-ray pulsars. Additionally,

epoch folding provides a straightforward approach to handling gaps which routinely appear in satellite data due to telemetry dropouts, passage through the South Atlantic Anomaly, Earth occupations, and so on. Thus, one keeps track, not only of the number of events placed in each data bin but also of the actual integration time per data bin.

Using same notations as for the PSDs, the basic approach to epoch folding considers a data set of total length, T sec, folded into N data bins at trial periods ranging from $P_{min} = 2\frac{T}{i_1}$ to $P_{max} = 2\frac{T}{i_2}$, with $i = i_2, i_2 + 1, \ldots, i_1$. Thus, the frequency spacing is $1/2T$, and the periods are searched in steps of the frequency resolution divided by two. The statistic S used to determine the presence of pulsations is calculated for each trial period from P_{min} to P_{max} and is

$$S = \sum_{j=1}^{N} \frac{(R_j - R)^2}{\sigma_j^2} \tag{A.7}$$

where R_j is the counting rate in the jth bin. Periodic pulsations are manifest by large values of S, and $R = N_{all}/T'$, $\sigma_j^2 = R/T_j$, and N_{all} is the total number of photons, T_j is the total integration time for the jth bin, and T' is the sum of the T_j.

A.3 Cross Correlation and Cross Spectrum

To investigate the time lag between two light curves of different X-ray energies, the cross-correlation function (CCF) have been applied. But, the CCF-based analysis did not permit explicit determination of the frequency of the intensity variations contributing to the observed time lag. Cross spectral technique, which allows the frequency dependence of the time lags to be measured, have been also applied (van der Klis et al. 1987).

In this section, first we will briefly review the CCF, and, second, We will review the cross spectrum (CS).

A.3.1 Cross Correlation Function (CCF)

The CCF between the two different energy bands, x_k and y_k, is defined as

$$CC(u) = \sum_{k=0}^{N-u} \frac{x_k y_{k+u}}{\sigma_{x_k} \sigma_{y_{k+u}}} \tag{A.8}$$

where σ_{x_k} and $\sigma_{y_{k+u}}$ are error in the k and $k+u$ bin.

A.3.2 Cross Spectrum (CS)

The Fourier transforms of time series above two energy bands can be used to produce a cross spectrum in addition to the two power density spectra. Using same notations as for PSDs, two Fourier transforms a_j and b_j are described as,

$$a_j = \sum_{k=0}^{N-1} x_k e^{2\pi ijk/N} \quad j = -\frac{N}{2}, \ldots, \frac{N}{2} - 1, \tag{A.9}$$

and

$$b_j = \sum_{k=0}^{N-1} y_k e^{2\pi ijk/N} \quad j = -\frac{N}{2}, \ldots, \frac{N}{2} - 1. \tag{A.10}$$

The cross spectrum is defined as the Fourier transform of the CCF (Jenkins and Watts 1968).

$$CS_j = a_j {}^* b_j \qquad j = 0, \ldots, \frac{N}{2} - 1. \tag{A.11}$$

Time Lags

The argument of the CS is the phase delay (in radians) between intensity fluctuations in the two energy bands:

$$\text{phase delay } \theta = arctan\frac{Im(CS_j)}{Re(CS_j)} = arctan\frac{Re(a)Im(b) - Im(a)Re(b)}{Re(b)Re(b) - Im(a)Im(b)} \tag{A.12}$$

This is easily converted to a time delay via $\delta t = \theta/2\pi\nu$. A negative value of δt indicates that intensity fluctuations in the first energy band lags those in the second. In our data, the first energy band is the "iron-band" and the second is the other continuum bands.

Coherence Function

The magnitude of the cross spectrum can be used to derive the coherence function between two energy bands. The coherence function is a measure of the degree of the linear correlation between the two time series at each Fourier frequency (Vaughan and Nowak 1997). For the noiseless signals, the coherence function is defined as

$$\text{Coherence } \gamma = \frac{|CS_j|}{\sqrt{|a_j * a_j||b_j * b_j|}} = \frac{|CS_j|}{P_1 * P_2} \tag{A.13}$$

where P_1 and P_2 are the PSDs derived from a_j and b_j respectively.

Acknowledgement

I am deeply grateful to Prof. S. Kitamoto for his continuous guidance and encouragement throughout my graduate course. After he moved to Rikkyo University, he has continued to guide me there, and he has been worried about my thesis and given me a lot of new idea. I learned a lot on the science as well as on the experiments. I am grateful to all the members of the X-ray astronomy group at Osaka University, especially, Prof. H. Tsunemi, Prof. K. Hayashida, and Dr. E. Miyata for their continuous guidance and valuable suggestions.

I am much indebted to Prof. N. Shibazaki for his valuable discussion, suggestions and supports on this work as a theorist. I would like to express my gratitude to Prof. F. Nagase, and Dr. T. Mihara for their discussions and helpful suggestions.

I thank Dr. Torii, for his guidance through my graduate course and encouragement. He taught me a lot on X-ray pulsars. I also thank Dr. Kinugasa for his valuable comment for the analysis of the X-ray pulsars. I would thank my colleagues, Ms. J. Hiraga and Mr. K. Mori for discussions and suggestions on my works in my last three years in my graduate school days, and I also thank to my colleagues, Mr. Y. Hashimoto and Mr. K. Katayama for discussions on my works in my first two years in my graduate school days at Osaka Univ. I also thank Mr. H. Katayama, Mr. K. Kamazuka, Mr. T. Okada, and Ms. T. Horikawa. They are my colleagues in Osaka Univ and spent a good time. I would like to Mr. C. Baluta for careful reading and suggestions to improve my first paper on Cen X-3.

I thank Prof. S. Yahikozawa, Prof. H. Yamamoto, Prof. M. Yoshimori, and Mr. Suga. They have always encouraged me at Rikkyo Univ. Prof. S. Yahikozawa takes me to eat our every lunch and dinner with Prof. N. Shibazaki, and talks a lot of interesting topics on science. I also would like to thank my colleague at Rikkyo Univ, Mr. M. Wada, Mr. H. Hirayama, Mr. H. Ogawa, and very special thanks go to Mr. K. Suzuki, Mr. E. Ozawa, and Mr. Y. Tachibana for proofreading and spell checking this draft. They have also encouraged me to write this thesis.

I would thank many people whom I met in symposia, especially participants of the *Chandra* workshop in Sep 2001 in Washington. D.C. and participants of the X-ray 2000 in

March 2001 in Yokohama.

I would thank all the members of the help desk of *RXTE* . I used the *RXTE* On-Line Service.

I express special thanks to Ms. N. Kubo. She has always encouraged me and spent a great time with me.

Finally, I thank my family, my father, mother, elder brother, and his wife for supporting my school life in Osaka Univ and Rikkyo Univ.

This research has made use of data obtained through the High Energy Astrophysics Science Archive Research Center Online Service, provided by the NASA Goddard Space Flight Center. I have been supported by JSPS Research Fellowships for Young Scientists.

Bibliography

[1] Abbott, D.C., Bieging, J.H., Churchwell, E., & Cassinelli, J.P. 1980, ApJ, 238, 196

[2] Alpar, M.A., & Shaham, J. 1985, Nature, 316, 239

[3] Alexander, S.G., & Mészaros, P. 1989, ApJ, 344, 1

[4] Araya, R.A., & Harding, A.K. 1999, ApJ, 517, 334

[5] Araya-Góchez, R.A., & Harding, A.K. 2000, ApJ, 544, 1067

[6] Arons, J., 1993, ApJ, 408, 160

[7] Audley, M.D., Kelley. R.L., & Boldt, E.A. 1996, ApJ, 457, 397

[8] Audley, M.D. 1998, PhD. Thesis, Univ. of Maryland

[9] Basko, M.M. & Sunyaev, R.A. 1975, A&A, 42, 311

[10] Basko, M.M. 1978, ApJ, 223, 268

[11] Basko, M.M. 1980, A&A, 87, 330

[12] Bendat, J.S., & Piersol, A.G. 1971, "Random Data: Analysis and Measurement Procedures", John Wiley & Sons, Inc. New York

[13] Bildsten, L., Chakrabarty, D., Chiu, J., Finger, M.H., Koh, D.T., Nelson, R.W., Prince, T.A., Rubin, B.C., Scott, D.M., Stollberg, M, Vaughan, B.A., Wilson, C.A.,& Wilson, R.B., 1997, ApJS, 113, 367

[14] Blondin, J,M., Stevens, I,R. & Kallman, T.R. 1991, ApJ, 371, 684

[15] Bondi, H. & Hoyle, F. 1944, MNRAS, 104, 273

[16] Bonnet-Bidaud, J.M., & van der Klis, M. 1979, A&A, 73, 90

[17] Bradt, H.V., Rothschild, R.E., & Swank, J., H. 1993, A&AS, 97, 355

[18] Bulik, T., Mészaros, P., Woo, J.W., Nagase, F., & Makishima, K., 1992, ApJ, 395, 564

[19] Bulik, T., Riffert, H., Mészaros, P., Makishima, K., Mihara, T., & Thomas, B. 1995, ApJ, 440, 405

[20] Burderi, L., Salvo, T. Di., Robba, N.R., Barbera, A. La., & Guainazzi,M. 2000, ApJ, 530, 429

[21] Burnard, D.J., Arons, J., & Klein, R. 1991, ApJ, 367, 575

[22] Burrows, A., Hayas, J., & Fryxell, B.A. 1995, ApJ, 450, 830

[23] Chevalier, R.A. 1975, ApJ, 199, 189

[24] Clark, G.W., Woo, J.W., Nagase, F., Maskishima, K., & Sakao, T., 1990, ApJ, 353, 274

[25] Cobrun, W. 2001, Ph.D. thesis, Univ. of California, Sandiego

[26] Chodil, G., Mark, H, Rodrigues, R., Seward, F.D. & Swift, C.D., 1967, ApJ, 150, 57

[27] Davidson, K.,& Ostriker, J.P. 1973, ApJ, 179, 585

[28] Day, C.S.R., & Tennant, A.F. 1991, MNRAS, 251, 76

[29] Day, C.S.R., & Stevens, I.R. 1993a, ApJ, 403, 322

[30] Day, C.S.R., Nagase, F., Asai, K., & Takeshima, T. 1993b, ApJ, 408, 656

[31] Ebisawa, K., Day, C.S.R., Kallman, T.R., Nagase, F., Kotani, T., Kawashima, K., & Kitamoto, S. 1996, PASJ, 48, 425

[32] Elsner, R.F., Shibazaki, N., & Weisskopf, M.C. 1987, ApJ, 320, 527

[33] Fabbiano, G., & Schreier, E.J. 1977, ApJ, 214, 235

[34] Garmany, C.D., Olson, G.L., Conti, P.S., & van Steenberg, M.E. 1981, ApJ, 250, 660

[35] Giacconi, R., Gursky, H., Kellogg, E., Schreier, E., & Tananbaum, H. 1971, ApJ, 167, L67

[36] Giles, A.B., Jahoda, K., Swank, J.H., & Zhang, W. 1995, PASA, 12, 219

[37] Ghosh, P., & Lamb, F.K. 1979a, ApJ, 232, 259

[38] Ghosh, P., & Lamb, F.K. 1979b, ApJ, 234, 296

[39] Ghosh, P., Angelini, L., & White, N.E. 1997, ApJ, 478, 713

[40] Harding, A.K., & Daugherty, J.K., 1991, ApJ, 374, 687

[41] Hatchett, S., & Weaver, R. 1977, ApJ, 215, 285

[42] Heindl, W.A., Coburn, W., Gruber, D.E., Rothschild, R.E., Kreykenbohm, I, Wilms, J., & Staubert, R. 2001, ApJL, 563, L35

[43] Howarth, I.D., & Prinja, R.K. 1989, ApJS, 69, 527

[44] Howe, S.K., Primini, F.A., Bautz, M.W., Lang, F.L., Levine, A.M., & Lewin, W.H.G. 1983, ApJ, 272, 678

[45] Holye, F., Narlikar, J.V., & Wheeler, J.A, 1964, Natuer, 203, 914

[46] Hutchings, J.B., Cowely, A.P., Crapton, D., van Paradijs, J., & White, N.E. 1979, ApJ, 229, 1079

[47] Illarionov, A.F., & Sunyaev, R.A., 1975, A&A, 39, 185

[48] Isenberg, M., Lamb, D.Q., & Wang, J.C.L. 1998a, ApJ, 493, 154

[49] Isenberg, M., Lamb, D.Q., & Wang, J.C.L. 1998b, ApJ, 505, 688

[50] Inoue, H. 1985, Space Sci. Rev., 40, 317

[51] Jackson, J.C. 1975, M.N.R.A.S., 172, 483

[52] Jahoda, K, R.I., Swank, J.H., Giles, A.B., Stark, M.J., Strohmayer, T., Zhang, W., & Morgan, E.H. 1996, SPIE, 2808, 59

[53] Janka, H.T. & Müller. 1995, ApJL, 448, L109

[54] Janka, H.T. & Müller. 1996, A&A, 306, 167

[55] Jenkins, G., & Watt, D., 1968, *Spectral Analysis and Its Applications*, (San Fransisco: Holden-Day).

[56] Jernigan, J.G., Klein, R.I., & Arons, J. 2000, ApJ, 530, 875

[57] Joss, P.C., & Rappaport, S.A. 1984, ARA&A, 22. 537

[58] Kallman, T.R., & McCray, R. 1982, ApJS, 50, 263

[59] Kelley, R.L., Rappaport, S., Clark, G.W, & Petro, L.D. 1983, ApJ, 268, 790

[60] Kii, T., Hayakawa, S., Nagase, F., Ikegami, T., & Kawai, N., 1986, ApJ, 38, 751

[61] Kitamoto, S., Tsunemi, H., Miyamoto, S., Yamashita, K., Mizobuchi, S., Nakagawa, M., Dotani, T., & Makino, F., 1989, Nature, 342, 518

[62] Klein, R.I., Arons, J., Jernigan, G., & Hsu, J. 1996, ApJ, 457, L85

[63] Kohmura, T., Kitamoto, S., & Torii, K. 2001, ApJ, inpress

[64] Krezminski, W. 1974, ApJ, 192, L135

[65] Lamers, H.J.G.L.M., van den Heuvel, E.P.J., & Petterson, J.A. 1976, A&A, 49, 327

[66] Lamers, H.J.G.L.M. 1981, ApJ, 245, 593

[67] Lamb, F.K., Pethick, C.J. & Pines, D. 1973, ApJ, 184, 271

[68] Lamb, F.K., Shibazaki, N., Alpar, M. A., & Shaham, J. 1985, Nature, 317, 681

[69] Latal, H.G., 1986, ApJ, 309. 372

[70] Leahy, D.A., Darbro, W., Elsner, R.F., Weisskopf, M.C., Kahn, S., Sutherland, P.G., & Grindlay, J.E. 1983, ApJ, 266, 160

[71] Leahy, D.A. 1987, A&A, 180, 275

[72] Liedahl, D.A., Sako, M., Wojdowski, P.S., Paerels, F., Kahn, S.M. 2000, RevMexAA, 9, 40

[73] Liu, Q.Z., van Paradijis, J., & van den Heuvel E.P.J., 2000, A&AS, 147, 25

[74] Liu, Q.Z., van Paradijis, J., & van den Heuvel E.P.J., 2001, A&A, 1021

[75] Levine, A.M., Bradt, H., Cui, W., Jernigan, J.G., Morgan, E.H., Remillard, R., Shirey, R.E., & Smith, D.A. 1996, ApJ, 469, L33

[76] Makishima, K. 1986, in The Physics of Accretion onto Compact Objects, et. K. O. Mason., M. G. Watson., & N.E. White. (Berlin: Springer), 249

[77] Makishima, K. Ohashi, T., Kawai, N., Matsuoka, M., Koyama, K., Kunieda, H, Tawara, Y, Ushimaru, N., Corbet, R.H.D., Inoue, H., Kii, T., Makino, F., Mitsuda, K., Murakami, T., Nagase, F., Ogawara, Y., Tanaka, Y., Kitamoto, S., Miyamoto, S., Tsunemi, H., Yamashita, K. 1990, PASJ, 42, 295

[78] Makishima, K. & Mihara, T. 1992. "in Frontiers of X-ray Astronomy". ed. Y. Tanaka & K. Koyama (Tokyo: Universal Academy), 23

[79] Makishima, K., Mihara, T., Nagase, F., & Tanaka, Y. 1999, ApJ, 525, 978

[80] Mereghetti, S., Stella, L., & Israel, G.L. 1997, The Active X-ray Sky: Results from Beppo SAX and Rossi XTE, Nuclear Physics B Proceedings Supplements, ed. L. Scarsi, H. Bradt, P. Giommi & F. Fiore, Elsevier Science B.V

[81] Mészaros, P. & Nagel, W. 1985a, ApJ, 298, 147

[82] Mészaros, P. & Nagel, W. 1985b, ApJ, 299, 138

[83] Mészaros, P. 1992, High Energy Radiation from Magnetized Neutron Stars (Chicago: Univ. of Chicago Press)

[84] Miller, M.C., Lamb, F.K., & Psaltis, D. 1996, astro-ph/9609157v1

[85] Miller, M.C., Lamb, F.K., & Psaltis, D. 1998, ApJ, 508, 791

[86] Mihara, T. 1990, Makishima, K., Ohashi, T., Sakao, T., & Tashiro, M., 1990, Nature, 346, 250

[87] Mihara, T. 1995, *Ph.D. thesis*, University of Tokyo

[88] Miyamoto, S., Kitamoto, S., Mitsuda, K., & Dotani, T. 1988, Nature, 336, 450

[89] Miyamoto, S., Kitamoto, S., Iga, S., Negoro, H., & Terada, K. 1992, ApJ, 391, L21

[90] Murakami, T., Inoue, H., Kawai, N., Koyama, K., Makishima, K., Matsuoka, M., Oda, M., Ogawara, Y., Ohashi, T., Shibazaki, N., Tanaka, Y., Hayakawa, S., Kunieda, H,, Makino, F., Masai, K., Nagase, F., Tawara, Y., Miyamoto, S., Tsunemi, H., Yamashida, K., & Kondo, I. 1983, ApJ, 264, 563

[91] Nagase, F., Hayakawa, S., Tsuneo, K. Sato, N. Ikegami, T. Kawai, N. Makishima, K., Matsuoka, M., Mitani, K., Murakami, T. Oda, M. Ohashi, T., & Tanaka, Y., 1984, PASJ, 36, 667

[92] Nagase, F. 1985, Adv. Space. Res., 5, 95

[93] Nagase, F. 1989, PASJ, 41, 1

[94] Nagase, F., Corbet, R.H.D., Day, C.S.R., Inoue, H., Takeshima, T., Yoshida, K., & Mihara, T. 1992, ApJ, 396, 147

[95] Nagel, W., 1980, ApJ, 236, 904

[96] Nagel, W., 1981, ApJ, 251, 278

[97] Ostriker, J.P. & Shu, F.H., 1995, ApJ, 447, 813

[98] Pacini, F. 1967, Nature, 216, 567

[99] Pounds, K.A., Cooke, B.A., Ricketts, M.J., Turner, M.J., & Elvis, M. 1975, M.N.R.A.S., 172, 473

[100] Press, W.H., Teukolsky, S.A., Vetterling, W.T., & Flannery, B.P . 1988, Numerical Recipes in C, Cambridge Univ. Press

[101] Pringle, J.E. 1972, & Rees, M.J. 1972, A&A, 21, 1

[102] Pravdo, S.H. 1979, in X-ray Astronomy, ed. Baity, W.A & Peterson, L.E (Oxford; Pergamon), 169

[103] Rappaport, S., & Joss, P.C. 1981, in *X-ray Astronomy with the Einstein Satellite*, ed. R. Giacconi, (Doredrecht: Reidel), p.123.

[104] Rappaport, S., & Joss, P.C. 1983, in Accretion-Driven Stellar X-Ray Sources, ed W.H.G. Lewin & E.P.J. van den Heuvel, Cambridge Univ. Press. p1

[105] Rots, A.H., Jahoda, K., Macomb, D.J., Kawai, N., Saito, Y. Kaspi, V.M., Lyne, A.G., Manchester, R.N., Backer, D.C., Somer, A.L. Marsden, D. & Rothschild, R.E., 1998, ApJ, 501, 749

[106] Rothschild, R.E., Blanco, P.R., Gruber, D.E., Heindl, W.A., MacDonald, D.R., Marsden, D.C., Pelling, M.R., Wayne, L.R., & Hink, P.L. 1998, ApJ, 496, 538.

[107] Santangelo, A., Sordo, S.D., Segreto, A., fiume, D.D., Orlandini, M., & Piraino, S. 1998, A&A, 340, L55

[108] Schreier, E., Levinson, R., Gursky, H., Kellogg, E., Tananbaum, H., & Giacconi, R. 1972, ApJ, 172, L79

[109] Schreier, E., Giacconi, R., Gursky, H., Kellogg, E., Levinson, R., & Tananbaum, H., 1973, IAU *Circ.*, No. 2524.

[110] Schreier, E., Swarts, K., Giacconi, R., Fabbiano, G., & Morin, J., 1976, ApJ, 204, 539

[111] Shakura, N.I., Sunyaev, R.A. 1973, A&A, 24, 337

[112] Shibazaki, N., & Lamb, F.K. 1987, ApJ, 318, 767

[113] Soong, Y. & Swank, J.H. 1989, in Proc. 23rd ESLAB Symp. on *Two Topics in X-ray Astronomy*, Bologna, Italy, 13-20, Sep, 1989 (ESA SP-296), p.617

[114] Sparks, W.M. 1975, ApJ, 199, 462

[115] Stella, L., White, N.E., & Rosner, R. 1986, ApJ, 308, 669

[116] Stella, L., & Vietri, M. 1998, ApJ, 492, L59

[117] Stella, L., & Vietri, M. 1999, Phys. Rev. Lett. 82, 17

[118] Strohmayer, T.E., Zhang, W., Swank, J.H., Smale, A., Titarchuk, L., & Day, C. 1996, ApJ, 469, L1

[119] Sunyaev, R.A., & Titarchuk, L.G. 1980, A&A, 86, 121

[120] Swank, J.H. 1997, Nucl. Phys. B. Proc. Suppl, 69, 12

[121] Takeshima, T., Dotani, T., Mitsuda, K., & Nagase, F. 1991, PASJ, 43, L43

[122] Takeshima, T. 1992, Ph D. Thesis in Univ. of Tokyo

[123] Tanaka., Y. 1986, in Radiation Hydrodynamics in Stars and Compact Object, ed. D. Mihalas & K.-H. Winkler (Berlin: Springer), 198

[124] Tananbaum, H., Gursky, H., Kellogg, E.M., Levinson, R., Schreier, E., & Giacconi, R. 1972, ApJ, 174, 143

[125] Tarter, C.B., Tucker, W., & Salpeter, E.E. 1969, ApJ, 156, 943.

[126] Tennant, A.F. 1988, a talk presented in The Fifth Los Alamos Space Physics/Astrophysics workshop, "Quasi-Periodic Oscillations in Luminous Galactic X-ray Sources," La Cienega, New Mexico, Octorber 1988.

[127] Thomas, H.-C. 1974, ApJ, 191, L25

[128] Thomas, H.-C. 1977, Ann. Rev. Astr. Ap., 15, 127

[129] Titarchuk, L.G., Lapidus, I., & Muslimov, A. 1998, ApJ, 499, 315

[130] Titarchuk, L.G., & Osherovich, V. 1999, ApJ, 518, L95

[131] Tjemkes, S.A., van Paradijs, J., & Zuiderwijk, E.J. 1986, A&A, 154, 77

[132] Trüemper, J., Pietsch, W., Reppin, C., Voges, W., Staubert, R., & Kendziorra, E. 1978, ApJ, 219, 105

[133] Tsunemi, H. 1989, PASJ, 42, 453

[134] Tsunemi, H., Kitamoto, S., & Tamura, K. 1996, ApJ, 456, 316

[135] Tuohy, I.R. 1976, MNRAS. 174, 45

[136] van den Heuvel, E.P., & de Loore, C., 1973, Naure, 245, 117

[137] van der Klis, M., Bonnet-Bidaud, J.M., & Robba, N.R. 1980, A&A, 88, 8

[138] van der Klis, M., Jansen, F. 1985a, Nature, 313, 768

[139] van der Klis, M., Jansen, F., van Paradijs, J. Lewin, W.H.G., Trumper, J. & Sztajno, M. 1985b, IAU *Circ.*, No. 4043

[140] van der Klis, M., Hasinger, G., Stella L., Langmeier, A., van Paradijs, J., & Lewin, W.H.G. 1987, ApJ, 319, L13

[141] van der Klis, M. 1989, Timing Neutron Stars, ed. H. Ögelman, & E.P.J. van den Heuvel, NATO ASI Series, p29-

[142] van der Klis, M. 1995, "X-ray Binaries", ed. W.H.H. Lewin., jan van Paradijs, & E.P.J. van den Heuvel, Cambridge Univ. Press. p. 293

[143] van der Klis, M., Swank, J.H., Zhang, W., Jahoda, K., Morgan E.H. 1996, ApJ, 469, L1

[144] van der Klis, M., "Astronomical Time Series", ed. D. Maoz, A. Sternberg, & E.M. Leibowitz, 1997 (Dordrecht: Kluwer), p. 121

[145] van der Klis, M. 1999, "Pulsar Timing, General Relativity and the Internal Structure of Neutron Stars", ed. Z. Arzoumanian, F. Van der Hooft, & E. P. J. van den Heuvel. (Amsterdam: Koninklijke Nederlandse Akademie van Wetenschappen,) ISBN 90-6984-247-5, 1999, p.259.

[146] van Paradijs, J., & McClintock, J.E. 1995, "in X-ray Binaries", eds. W.H.G. Lewin, J. van Paradijs, and E.P.J. van den Heuvel (Cambridge: Cambridge Univ. Press), p. 58

[147] van Paradijs, J., Taam, R.E., & van den Heuvel, E.P.J. 1995, A&A, 299, L41

[148] Vaughan, B.A., van der Klis, M., Wood, K.S., Norris, J.P., Hertz, P., Michelson, P.F., van Paradijs, J., Lewin W.H.G., et al. 1994, ApJ, 435, 362

[149] Vaughan, B.A., & Nowak, M.A., 1997, ApJ, 474, L43

[150] Ventura, J., 1979, Phys.Rev.D, 19, 1979

[151] Voges, W., Pietsch, W., Reppin, C., Truemper, J., Kendziorra, E. & Staubert, R. 1982, ApJ, 263, 803

[152] Wang, Y.-M., 1996, ApJ, 465, L111

[153] Wheeler, J.C., Mckee, C.F., & Lecar,M. 1974, ApJ, 192, L71

[154] White, N.E., Swank, J.H., & Holt, S.S. 1983, ApJ, 270, 711

[155] White, N.E., Angelini, L., Ebisawa, K., Tanaka, Y., & Ghosh, P. 1996, ApJ, 463, L83

[156] Woltjer, L. 1964, ApJ, 140, 1309

[157] Zahn, J,-P. 1975, A&A, 41, 329

[158] Zahn, J,-P. 1977, A&A, 57, 383